Rep. Prog. Phys. **63** (2000) 1317–1427. Printed in the UK PII: S0034-4885(00)07909-4

Detection of gravitational waves

L Ju, D G Blair and C Zhao
Department of Physics, The University of Western Australia, Nedlands, WA 6907, Australia

Received 4 January 2000

Abstract

Gravitational wave detectors have been under development since the pioneering work of Weber in the 1960s. The long and painstaking research effort has yielded enormous improvements in detector sensitivity. Astronomical observations of binary pulsar systems have confirmed the existence of gravitational radiation. Direct detection is inevitable once planned detectors reach sensitivity goals.

This review begins by introducing the concept of gravitational waves, and discusses their significance. Section 2 discusses sources of gravitational waves, giving estimates of signal characteristics and signal strengths. Section 3 presents an overview of gravitational wave detection and the critical issues of data processing.

In the fourth section the physics of resonant-mass gravitational wave detectors is discussed in some detail, covering all areas from antenna materials to transducers and the quantum limits to measurement. This section reviews the major operating antennas in the existing worldwide array but also discusses the prospects for achieving substantial increases in sensitivity in the future.

The fifth section presents the concepts and designs for laser interferometer gravitational wave detectors. Large-scale devices will be in operation in the first decade of the twenty-first century and should eventually be certain of detecting a known class of gravitational wave source. At their predicted sensitivity, space interferometers will be able to detect numerous known galactic sources of gravitational waves and also will be able to detect black hole mergers that are thought to have occurred as primordial galaxies merged and grew in the early universe.

(Some figures in this article are in colour only in the electronic version; see `www.iop.org`)

0034-4885/00/091317+111$90.00

Contents

1. Introduction to gravitational waves

1.1. Listening to the universe

Our sense of the universe is provided predominantly by electromagnetic waves. During the twentieth century the opening of the electromagnetic spectrum has successively brought dramatic revelations. For instance, optical astronomy gave us the Hubble law expansion of the universe. Radio astronomy gave us the cosmic background radiation, the giant radio jets emerging from black holes in galactic nuclei and neutron stars in the form of radio pulsars. X-ray astronomy gave us interacting neutron stars and black holes. Infrared astronomy gave us evidence for a massive black hole in the nucleus of our own Galaxy.

Gravitational waves offer us a new sense with which to understand our universe. If electromagnetic astronomy gives us eyes with which we can see the universe, then gravitational wave astronomy offers us ears with which to hear it. We are presently deaf to the myriad gravitational wave sounds of the universe. Imagine you are in a forest: you see a steep hillside, massive trees and small shrubs, bright flowers and colourful birds flitting between the trees. But there is much more to a forest: the sound of the wind in the treetops, the occasional crash of a falling branch, the thump thump of a fleeing kangaroo, the pulse of cicadas, the whistles of parrots and honking of bell frogs. The sense of hearing dramatically enriches our experience.

The gravitational wave universe is likely to be rich with 'sounds' across a frequency range from less than one cycle per month (below one microhertz) up to tens of kilohertz. Frequencies in the audio frequency band will be detectable using Earth-based detectors. But lower frequencies will require observatories in space. Gravitational waves are produced whenever there is non-spherical acceleration of mass–energy distributions. The lowest frequencies will consist of extremely red-shifted signals from the very early universe, as well as the slow interactions of very massive black holes, and a weak background from binary star systems. Signal frequencies often scale inversely as the mass of the relevant systems. Black holes below 100 solar masses, and neutron stars will produce gravitational waves in the audio frequency range: nearly monochromatic whistles from millisecond pulsars, short bursts from their formation, and chirrups from the coalescence of binary pairs.

During the twentieth century, at each opening of a new window in the electromagnetic spectrum, the universe surprised us with unexpected phenomena. Our imagination and ability to predict is limited. The sources we predict today are probably just a fraction of what we will hear when our detectors reach sufficient sensitivity.

Gravitational waves are waves of tidal force. They are vibrations of spacetime which propagate through space at the speed of light. They are registered as tiny vibrations of carefully isolated masses. Their detection is primarily an experimental science, consisting of the development of the necessary ultra-sensitive measurement techniques. While the gravitational waves can be considered as classical waves, the measurement systems must be treated quantum mechanically since the expected signals generally approach the limits set by the uncertainty principle.

The binary pulsar PSR 1913+16 has played a key role in the unfolding story of gravitational waves. This system has proved Einstein's theory of general relativity to high precision, including the quadrupole formula which states that the total emitted gravitational wave power from any system is proportional to the square of the third time derivative of the system's quadrupole moment. The pulsar loses energy exactly as predicted by this formula [1]. Hulse and Taylor, who discovered the system more than 20 years ago [2], were rewarded by a Nobel prize in 1993, by which time careful monitoring had shown gravitational wave energy loss from the system in agreement with theory to better than 1%.

1.2. Gravitational waves in stiff-elastic spacetime

In Newtonian physics spacetime is an infinitely rigid conceptual grid. Gravitational waves cannot exist in this theory. They would have infinite velocity and infinite energy density because in Newtonian gravitation the metrical stiffness of space is infinite. Conversely general relativity introduces a finite coupling coefficient between curvature of spacetime, described by the Einstein curvature tensor, and the stress energy tensor which describes the mass–energy which gives rise to the curvature. This coupling is expressed by the Einstein equation

$$\boldsymbol{T} = \frac{c^4}{8\pi G}\boldsymbol{G}. \tag{1.1}$$

Here $\boldsymbol{T}$ is the stress energy tensor and $\boldsymbol{G}$ is the Einstein curvature tensor, c is the speed of light and G is Newton's gravitational constant. The coupling coefficient $c^4/(8\pi G)$ is an enormous number, of order 10^{43}. This expresses the extremely high stiffness of space which is the reason that the Newtonian law of gravitation is an excellent approximation in normal circumstances, and why gravitational waves have a small amplitude, even when their energy density is very high.

The existence of gravitational waves is intuitively obvious as soon as one recognizes that spacetime is an elastic medium. The basic properties of gravity waves can be easily deduced from our knowledge of Newtonian gravity, combined with knowledge that spacetime curvature is a consequence of mass distributions.

First, consider how gravitational waves might be generated. Electromagnetic waves are generated when charges accelerate. Because a negative charge accelerating to the left is equivalent to a positive charge accelerating to the right, it is impossible to create a time-varying electric monopole. The process of varying the charge on one electrode always creates a time-varying dipole moment. Hence it follows that electromagnetic waves are generated by time-varying dipole moments. In contrast to electromagnetism, gravity has only one charge: there is no such thing as negative mass! Hence it is not possible to create an oscillating mass dipole. Action equals reaction. That is, momentum is conserved and the acceleration of one mass to the left creates an equal and opposite reaction to the right. For two equal masses, their spacing can change but the centre of mass is never altered. This means that there is a time-varying quadrupole moment, but there is no variation in monopole or dipole moment.

To be certain of the quadrupole nature of gravitational waves, think of a system which collapses under its own gravity. First think of a spherically symmetrical array of masses that collapse gravitationally towards a point. At a distance there is no difference between the gravitational field of a point mass and that of the same mass distributed in a uniform spherical distribution. (This is a consequence of the inverse square law, and is also true for electric fields.) Hence the process of gravitational collapse of a spherical distribution creates no variation in the external gravitational field, and hence no gravitational waves. Clearly gravitational waves must be created by non-spherical motions of masses. Consider a ring of eight test masses, such as the one illustrated in figure 1.

The simplest non-spherical motion is one in which the edge masses move inwards and the top and bottom masses move apart as shown in figure 1(*a*). Such a quadrupole motion does vary the external field and does create gravitational waves. For a small amount of vertical stretching, and an equal horizontal shrinking, it is obvious that the diagonally placed masses have no radial motion. There is clearly a second polarization rotated 45° from the first in which the diagonal masses move radially, and the top, bottom and edge masses have no radial motion. Unlike electromagnetic waves, gravitational wave polarizations are just 45° apart.

Gravitational wave detection can be easily understood from the symmetry between sources and detectors—time reversal invariance. A gravitational wave will distort a ring of test masses

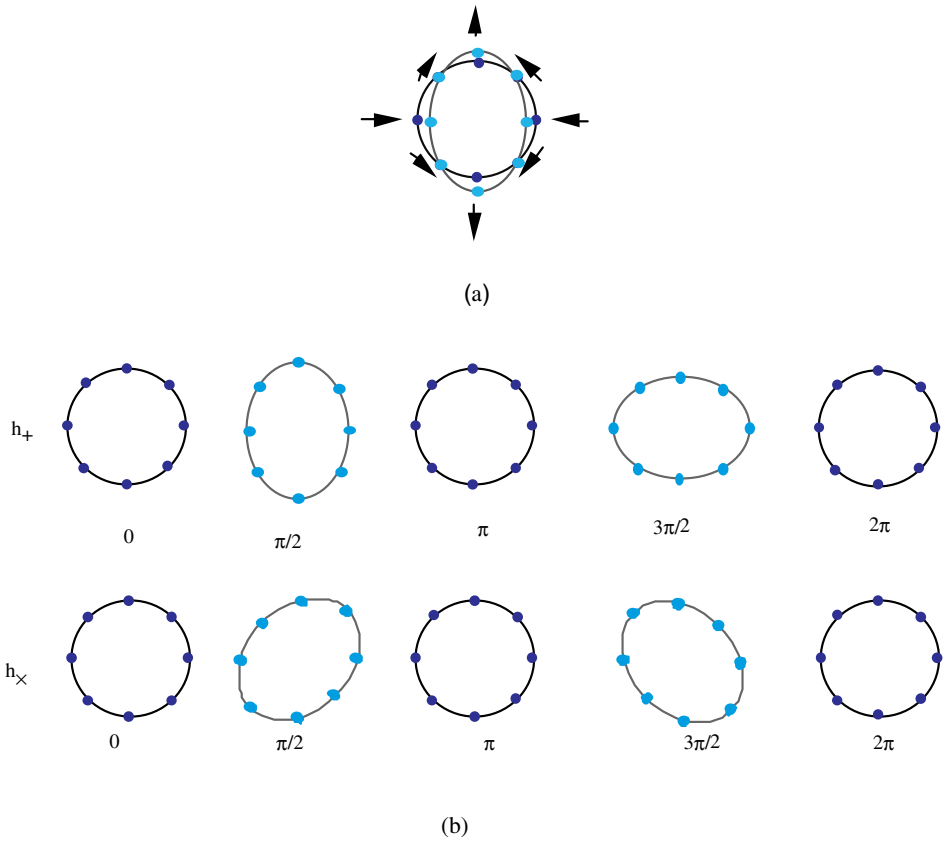

Figure 1. (*a*) The lowest order non-spherical deformation of a ring: the diagonal masses *are not moved*. (*b*) The deformation of a ring of test particles in one cycle of a gravitational wave field.

in exactly the same way that the distortion of a ring of test masses creates gravitational waves. The non-spherical deformation pattern we just observed is exactly like the tidal deformation of the Earth created by the gravity gradient due to the Moon. A gravitational wave is indeed a wave of time-varying gravity gradient. The amplitude of a gravitational wave is measured by the relative change in spacing between masses. That is, the wave amplitude, usually denoted h, is given by $\Delta L/L$, where L is the equilibrium spacing and ΔL is the change of spacing of two test masses. Whereas electromagnetic luminosity depends on the square of the second time derivative of the electric dipole moment, the gravitational wave luminosity is proportional to the square of the *third time* derivative of the mass quadrupole moment. The extra derivative arises because gravitational wave generation is associated with the differential acceleration of masses.

The above deformation patterns also apply to solid or fluid bodies. The rigidity of normal matter is so low compared with that of spacetime that the stiffness of the matter is utterly negligible. Considering the deformations of figure 1(*a*) applying to a solid sphere, such as the Earth, it also follows that the 45° points must involve circumferential motions since the deformation shown acts to transfer matter from the 'equator' to the poles in the same way that the lunar tides act on the Earth.

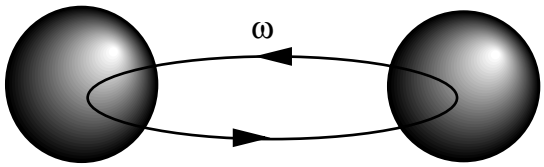

Figure 2. A rotating dumbbell or a binary star system, viewed edge-on, has a maximal variation of quadrupole moment.

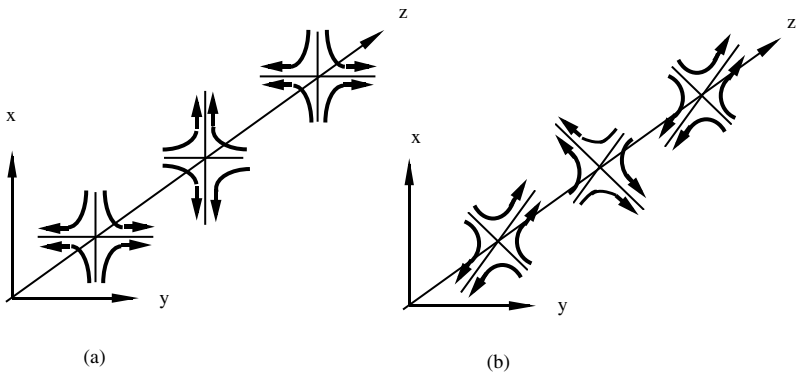

Figure 3. Gravitational wave field force lines. (*a*) '+' polarization; (*b*) '×' polarization.

The gravitational wave has an effective force field determined by the displacement vectors of the test masses. The force field is discussed further below, and is shown in figure 3. The force field indicates that detectors can be designed to couple to gravity waves in several different ways. They may detect straight linear strains, orthogonal strains, or circumferential strains.

The weak coupling of gravitational waves to matter is a consequence of the enormous elastic stiffness of spacetime. If the elastic stiffness of spacetime were infinite (Newtonian physics) the coupling would be zero. In general relativity the generation of gravitational waves is given quantitatively by combining the third time derivative of the quadrupole moment described above, with the appropriate coupling constant. The latter can only depend on the constants G and c (for classical waves) and by dimensional analysis this constant must have the form G/c^5. The luminosity of a source is given by

$$L_G \sim \frac{G}{c^5}\left(\frac{\mathrm{d}^3 D}{\mathrm{d}t^3}\right)^2. \tag{1.2}$$

Except for a numerical factor, this is the Einstein quadrupole formula [3]. There are two useful formulae one can derive from equation (1.2). The first is the formula for a hypothetical terrestrial source or binary star system. The second is for an interacting black hole system. The terrestrial source might be a pair of oscillating masses joined with a spring. Ideally, the spacing of the masses should change from zero to L. This is achieved in the edge on view of a rotating dumbbell or binary star system in a circular orbit as shown in figure 2. Viewed edge-on the masses appear to move in and out periodically twice per rotation cycle. The quadrupole moment for two masses distance x apart is Mx^2. If the motion is sinusoidal at an angular frequency of ω, the square of the third time derivative is $\sim M^2L^4\omega^6$. Thus the gravitational

wave luminosity of such a system is

$$L_c \sim \frac{G}{c^5} M^2 L^4 \omega^6. \tag{1.3}$$

This equation applied to any natural or artificial source in our solar system gives a depressingly small luminosity, due to the extraordinarily small value of G/c^5. However, the situation is different in an astrophysical context.

Suppose that the system is a similar binary system, except that it consists of a pair of gravitationally bound masses, of size such that their escape velocity approaches c and their radius is near to the Schwartzchild radius: that is, a pair of black holes. In this case we can express L in units of the Schwartzchild radius, using $r_s = 2GM/c^2$ and replace $L\omega$ with velocity expressed in light speed units. Then it follows immediately that

$$L_G \sim \frac{c^5}{G} \left(\frac{v}{c}\right)^6 \left(\frac{r_s}{r}\right)^2. \tag{1.4}$$

The remarkable difference between equation (1.3) and equation (1.4) expresses the difference between the physics of normal matter and black holes. Equation (1.3) is scaled by the tiny factor G/c^5, while equation (1.4) is scaled by its enormous reciprocal. Normal matter in our solar system creates negligible curvature of spacetime. A black hole creates an extreme distortion of spacetime. Hence normal matter sources are intrinsically extremely weak, while very large amplitude waves are created in events such as the coalescence of a pair of black holes (for which we would expect $v \sim c$ when $r_s \sim r$). The factor c^5/G is roughly the total electromagnetic luminosity of the universe. This is the upper limit to the gravitational wave luminosity of black hole systems. In reality, equation (1.4) does not take into account the gravitational redshift effects and other spacetime curvature effects which act to reduce the maximum luminosity. However, to order of magnitude, equation (1.4) indicates the extreme luminosity of gravitational waves that can be expected in short bursts when gravitationally collapsed systems with strong gravity, such as black holes (escape velocity $= c$) and neutron stars (escape velocity $\sim 0.1c$), are involved.

As we saw above, a gravitational wave is a wave of gravity gradient which causes relative displacements, or strains between test masses. The detection of gravitational waves requires the detection of small strain amplitudes. We should now consider the typical size of such strain amplitudes. One can very crudely estimate this by scaling the amplitude of the gravitational wave relative to the extreme amplitude at the point of coalescence of two masses to form a black hole. At the point of black hole formation spacetime curvature is very large. For example, the deflection of light for a light beam passing near to the event horizon can approach a complete orbit of a black hole. At the point of generation the dynamic curvature of space that will become the outgoing gravitational wave is unlikely to be able to exceed the static curvature represented by the maximal deflections of light past a black hole. The strain $\Delta L/L$ represented by such deflections can be estimated from the difference in light travel time for the deflected path around the black hole (say half an orbit) and the direct path between the same points in the absence of the black hole. For a half-orbit (in Euclidean geometry) the circular path is $\pi/2$ longer than the direct path, so roughly $\Delta L \sim L$, and the maximum possible strain amplitude is $\sim$unity. But by the inverse square law, the amplitude of the wave reduces as $1/r$. (The energy density which is proportional to the square of the amplitude reduces as $1/r^2$.) So for such a black hole source we can give the strain amplitude at distance r as simply $h \sim r_s/r$. For more realistic sources only a fraction of the total energy will participate in quadrupole motion. Thus it is more reasonable to include an efficiency factor ε which characterizes the fraction of the total system rest mass which can convert to gravitational waves. In this case we

can write

$$h \sim \varepsilon^{1/2} \frac{r_s}{r}. \tag{1.5}$$

Since the Schwartzchild radius of a solar mass is a few kilometres, the maximum strain amplitude that can be expected from any stellar source is numerically equal to the reciprocal of its distance in kilometres. Because r_s is linearly proportional to the mass, gravitational wave amplitudes from very high mass sources, such as colliding 10^9 solar mass black holes in galactic nuclei, will be of correspondingly larger amplitude. Putting in numbers, equation (1.5) gives $h \sim 10^{-16}$ for 10 solar masses and 100% efficiency at the galactic centre, and $h \sim 10^{-13}$ for 3 billion solar masses at 3 Gpc (towards the edge of the visible universe).

Clearly these maximal numbers are very small. It might seem that the supermassive black hole sources might be much more detectable than the stellar mass source. The strain amplitude in this case corresponds to the detection of a motion equal to the size of an atomic nucleus on a one-metre baseline, or one metre between here and Neptune. In fact the detection of such small strains on Earth is probably impossible, because the frequency of the waves from supermassive black hole sources must always be very low. The peak frequency, or its reciprocal, the burst duration, can be estimated from the time the binary black hole system takes to complete its final orbit before coalescence. Its value is about 10 kHz for one solar mass, reducing inversely as the mass. Thus, the peak frequency will be about 1 kHz for the above galactic centre source, and 3×10^{-6} Hz for the distant massive black holes. The latter frequency will be reduced towards 10^{-6} Hz by cosmological redshifts. At such low frequencies environmental effects, and particularly gravity gradients associated with tides and weather variations in the surrounding environment, create perturbations which greatly exceed the desired signal. The only known means around this obstacle is by using drag-free satellite technology to create very stable free-floating masses in space, and laser interferometry between them. In this case detection does look relatively straightforward, though expensive, since it requires several widely spaced spacecraft. For frequencies above 1 Hz, terrestrial detection appears to be possible, limited only by fundamental quantum measurement limits.

For even lower frequencies than 10^{-6} Hz it is possible that radio pulsars can replace man-made spacecraft in detection systems. The pulsar ideally provides a perfect monochromatic timing signal. The radio beams from the pulsar are traversed by incoming gravitational waves. If several pulsars are observed in the same part of the sky, gravitational wave signals would appear as correlated arrival time variations of pulses from pulsars in different directions. In this case it is more convenient to consider the gravitational wave acting not on the pulsar itself, but on spacetime geometry near to the Earth through which the pulsar signal propagates.

Today detectors are in long-term operation which exceed the 10^{-16} sensitivity indicated above by more than two orders of magnitude. Advanced detectors of two types are under development which should achieve another three orders of magnitude in amplitude sensitivity.

For 50 years after Einstein predicted gravitational waves [3] physicists considered them to be of academic interest only. It was not until after the pioneering work of Joseph Weber [4], and his reported discoveries [5, 6] that a growing number of physicists around the world started to develop different types of antennas to search for gravitational waves. Since Weber's first reports, which were never confirmed, the improvement in detectors has been quite remarkable. Relating them to optical telescopes, the improvement achieved so far is equivalent to the step from a 3 cm diameter optical telescope to a 3 m diameter instrument. In the next decade it is hoped that the improvement will be equivalent to a step up in size from 3 m to 3 km. At this sensitivity gravitational wave detection is practically certain, and the field of gravitational astronomy will be able to slowly map and explore the new spectrum, and the objects that it reveals.

In the following sections we will discuss gravitational wave sources in more detail before going on to discuss detectors, first in the form of a general overview, and then with specific emphasis on existing ground-based detectors and their future prospects.

1.3. Gravitational waves in general relativity

Here we give a brief summary of the mathematical basis for gravitational waves. For further details on the theory of gravitational waves, readers are referred to [7–12].

The geometry of spacetime can be expressed by the metric tensor $g_{\alpha\beta}$ which connects the spacetime coordinate $\mathrm{d}x^{\alpha}(\alpha, \beta = 1, 2, 3, 4)$ to the spacetime interval $\mathrm{d}s$ by way of the relation

$$\mathrm{d}s^2 = g_{\alpha\beta}\,\mathrm{d}x^{\alpha}\,\mathrm{d}x^{\beta}. \tag{1.6}$$

In reality, gravitational waves in the vicinity of the Earth will always be very weak. The background curvature can be ignored and the background metric can be approximated as that of the Minkowski flat metric η. An approximation of the gravitational wave field can then be expressed in the form [7]

$$g_{\alpha\beta} = \eta_{\alpha\beta} + h_{\alpha\beta}, \tag{1.7}$$

where $\eta_{\alpha\beta}$ is the metric of the flat background, and $|h_{\alpha\beta}| \ll 1$ is the perturbation on this background. If there is no stress-energy source term in Einstein's field equation, i.e. $T = 0$ in equation (1.1), we are left with the weak field vacuum approximation to the Einstein equations. To obtain an explicit statement of the metric perturbations h it is necessary to make a gauge choice. The most useful gauge is the transverse traceless gauge in which the coordinates are defined by the geodesics of freely falling test bodies. In this gauge, and in the weak field limit discussed above, the equations of general relativity become a system of linear equations, specifically a system of wave equations [7]

$$\left(\nabla^2 - \frac{1}{c^2}\frac{\partial^2}{\partial t^2}\right) h_{\alpha\beta} = 0. \tag{1.8}$$

Equation (1.8) is a three-dimensional wave equation, telling us that gravitational waves travel at the speed of light c. The gravitational wave curvature tensor $\boldsymbol{h}$ can be considered as the gravitational wave field. The wave field is transverse and traceless, and for waves travelling in the z-direction may be expressed as follows:

$$h_{\alpha\beta} = \begin{bmatrix} 0 & 0 & 0 & 0 \\ 0 & h_{xx} & h_{xy} & 0 \\ 0 & h_{yx} & h_{yy} & 0 \\ 0 & 0 & 0 & 0 \end{bmatrix}. \tag{1.9}$$

There is no z-component due to the transverse nature of the waves, and to be traceless h satisfies

$$h_{xx} = -h_{yy}. \tag{1.10}$$

Because the Riemann tensor is symmetric, h also satisfies

$$h_{xy} = h_{yx}. \tag{1.11}$$

The symmetry of h means that there are just two possible independent polarization states which are usually denoted h_{+} and $h_{\times}$. In the case of sinusoidal gravitational waves we can express these polarizations as

$$h_{+} = h_{xx} = \mathrm{Re}\,[A_{+}\mathrm{e}^{-\mathrm{i}\omega(t-z/c)}], \tag{1.12}$$

$$h_{\times} = h_{xy} = \mathrm{Re}\,[A_{\times}\mathrm{e}^{-\mathrm{i}\omega(t-z/c)}]. \tag{1.13}$$

Here A_{+} and $A_{\times}$ are the strain amplitudes of each polarization.

We have already seen that a gravitational wave field moves masses in the same way that an electromagnetic wave sets charged particles in motion. Each wave field exerts tidal forces on objects through which it passes. The corresponding lines of force have a quadrupole pattern as shown in figure 3. Figure 3(*a*) shows the force lines of the '+' polarization and (*b*) shows the '×' polarization which is rotated 45° with respect to the '+' state. These time-varying tidal forces can deform an elastic body or change the distance between mass points in free space. A ring of particles placed perpendicular to the wave propagation direction will be distorted as we already saw in figure 1.

Einstein's famous quadrupole formula describes the gravitational wave amplitude from a source. Einstein derived his formula in a slow-motion weak field approximation, but Thorne [8] emphasizes that the result is accurate as long as the reduced wavelength exceeds source size. This condition applies to all but the most compact sources such as forming or coalescing black holes. The latter are potentially the strongest and most detectable sources. It is unfortunate that these are just the ones where the nonlinearity of general relativity, and in particular the gravitational redshift of the outgoing gravitational waves due to the gravitational energy of the spacetime curvature itself, makes the gravitational radiation amplitude extremely difficult to estimate.

The quadrupole formula states that the gravitational wave amplitude h at a distance R from a source is proportional to the second time derivative of the transverse traceless projection of the quadrupole moment evaluated at the retarded time $t - r/c$. That is

$$h_{jk} = \frac{2}{r}\frac{G}{c^4}\frac{\partial^2}{\partial t^2}[D_{jk}(t - R/c)]^{TT}, \qquad (j, k = 1, 2, 3) \tag{1.14}$$

where $[D_{jk}(t - R/c)]^{TT}$ is the transverse traceless projection of the quadrupole moment evaluated at retarded time $(t - R/c)$. The transverse traceless requirement relates to the transverse nature of gravitational waves, and the lack of wave generation from spherically symmetrical motions. For weak fields, for which gravitational self-energy is small (see Damour [13]) $\boldsymbol{D}$ is given by the second moment of the source mass density ρ:

$$D_{jk} = \int \rho(t)[x^j x^k - \tfrac{1}{3}x^2\delta^{jk}]\,\mathrm{d}^3x. \tag{1.15}$$

In this equation the term with the Kronecker delta ensures that D is trace-free.

The total gravitational wave power is proportional to the square of the third time derivative of the mass quadrupole moment [14]. In general, the total energy radiation rate L_G is given by the sum of the squares of all the projections of the quadrupole moment

$$L_G = \frac{1}{5}\frac{G}{c^5}\sum_{jk}\left|\frac{\mathrm{d}^3 D_{jk}}{\mathrm{d}t^3}\right|^2. \tag{1.16}$$

The very small universal constant

$$\frac{G}{5c^5} = 5.49 \times 10^{-54}\ \mathrm{s\,J^{-1}} \tag{1.17}$$

sets the characteristic gravitational radiation power output.

The presence of the factor (G/c^5) in equation (1.16) indicates that unless the $\dddot{D}_{jk}$ involves energy of astronomical proportions, the gravitational wave power will be extremely small. It is easy to show that it is impossible to generate detectable gravitational waves on the laboratory scale, even at extreme limits of known technology. We can only hope to observe gravitational waves emitted by astrophysical sources.

It is useful, however, to consider a laboratory source simply as an application of equations (1.15) and (1.16). Suppose the source consists of a pair of masses distance L apart,

and joined by a spring to allow sinusoidal oscillation of their spacing at angular frequency ω. From equation (1.15), $D = ML^2$, and if $L = L_0 + a \sin \omega t$, it follows that

$$D = ML_0^2 + 2ML_0 a \sin \omega t + Ma^2 \sin^2 \omega t. \tag{1.18}$$

From equation (1.18), taking the third time derivative, it follows that this source will produce gravitational waves at the frequencies of ω and 2ω. If the amplitude a is small compared with L_0, the 2ω term is small and the gravitational wave luminosity is given by

$$L_G = \frac{G}{5c^5} 4M^2 L_0^2 a^2 \omega^6. \tag{1.19}$$

For any practical harmonic oscillator on Earth L_G is infinitesimal. However, such mass quadrupole oscillators have been created as sources of near-field dynamic gravity gradients (not waves) for the purpose of calibrating gravitational wave detectors. Such systems has been successfully used for low-frequency detectors tuned to the Crab pulsar [15] and also by the Rome group to calibrate their resonant-bar detector and measure the inverse square law of gravitation [16].

2. Sources of gravitational waves

2.1. Introduction

Astrophysics provides us with a variety of candidate systems which should be observable in the spectrum of gravitational waves. However, it is important to remember that our powers of prediction of new phenomena are poor, so any list of sources is almost certain to be incomplete.

Amongst stellar mass systems we expect detectable gravitational radiation from the formation of black holes and neutron stars, and the coalescence of binary neutron stars and final collapse of such binaries to form a black hole. We would expect not only discrete sources, but also continuous stochastic backgrounds created from large numbers of discrete sources. In our Galaxy the very large populations of binary stars create a stochastic background in the 10^{-2} to 10 Hz range. In the universe as a whole all of the above neutron star and black hole formation events are likely to merge to form a continuous background in the audio frequency part of the spectrum. This particular background provides an exciting opportunity to observe the earliest epochs of Galaxy formation, and the birth and growth of the supermassive black holes that appear to reside in the nuclei of many galaxies and quasars. We may also be able to observe gravitational waves from the big bang, amplified during the inflationary era, and possible signatures of cosmological phase transitions and topological defects such as cosmic strings. These very earliest sources in the universe would constitute a probe of physics at energy scales far beyond those accessible in particle accelerators and hence represent the best opportunity we have to obtain experimental data from the era of inflation.

Back in our own Galaxy we would also expect to find many quasi-monochromatic sources of gravitational waves such as individual binary star systems, including binary neutron stars as they evolve towards coalescence, and various rotating neutron star systems such as millisecond and x-ray pulsars.

Figure 16 shows the gravitational wave spectrum across nine decades. The spectrum conveniently divides into a terrestrial detection band, above 1 Hz (generally within the audio frequency band), mainly associated with stellar mass compact objects, and a space detection band, from 10^{-6} to 10^{-1} Hz, where sources include both binary star systems in our Galaxy, and cosmological sources associated with massive black hole interactions.

2.2. Classification of sources

All the above sources can be naturally divided into three distinct classes, according to the methods of data processing and signal extraction. The first class consists of catastrophic *burst sources* such as the final coalescence of compact binary star systems, or the formation of neutron stars and black holes in supernova events. The binary coalescence events can consist of binary neutron stars, binary black holes, or neutron-star–black-hole binaries. The burst signal consists of a very short single event, consisting of one or very few cycles, and hence is characterized by a broad bandwidth, roughly determined by the reciprocal of the event duration.

The second class consists of *narrow-band sources*. These include the rotation of single nonaxisymmetric stars, particularly pulsars and accreting neutron stars, as well as binary star systems far from coalescence. All such systems are quasi-periodic because gravitational wave energy loss must cause period evolution, and in general they are also periodically Doppler shifted by binary motion and Earth's orbital motion. Such sources are generally weaker than the burst sources, but in principle they are always amenable to long-term integration to extract signals from the noise. This requires accurate knowledge of the frequency modulations to maintain a coherent integration. Assuming a white noise background and perfect knowledge of the frequency evolution, the signal-to-noise ratio increases as $N^{1/2}$ where N is the number of cycles. For narrow-band sources it may be possible to integrate for 10^8 s, compared with less than 10 ms for a burst source. Thus, at 100 Hz, N can be 10^{10} allowing a 10^5-fold improvement in signal-to-noise ratio.

The third class of sources are the *stochastic backgrounds* produced from the integrated effects of many weak periodic sources in our Galaxy, or from a large population of burst sources at very large distances, as well as the above-mentioned cosmological processes in the early universe. Stochastic backgrounds are difficult to detect in a single detector because they are practically indistinguishable from instrument noise. If the source was not isotropically distributed (such as a population of binary stars towards the centre of our Galaxy), it might be detectable from the variation of observed instrument noise as the detector orientation varied on the rotating Earth. However, a much better way of detecting stochastic backgrounds is by cross-correlating two nearby detectors. In this case the correlated stochastic signal will integrate up in relation to the uncorrelated instrument noise (assuming both detectors to be truly independent). In this case the signal-to-noise ratio increases as $N^{1/4}$, where N is the effective number of cycles, determined by the observation frequency. This technique allows a 300-fold improvement in signal-to-noise ratio in 10^8 s of integration, (compared again with a 10 ms burst source).

Binary neutron star systems can produce gravitational waves in all the three classes. First, a large population of binary neutron stars in our Galaxy, with orbital periods in the range from days to minutes, can produce a stochastic background of individually unresolvable sources in our Galaxy in the frequency band $\sim 10^{-2}$–10^{-5} Hz. Nearby individual systems which are far from binary coalescence could produce detectable nearly monochromatic waves at any frequency up to 0.1 Hz. In addition to the binary orbit, the individual rotation of the stars themselves (if they are nonaxisymmetric), will also give rise to quasi-periodic gravitational waves. For example, the spin-down of a millisecond pulsar can be entirely due to gravitational wave emission if just $10^{-7} M_\odot$ is located in a nonaxisymmetric configuration on the star [17]. As the binary evolves and radiates away gravitational potential energy, it will gradually spiral inwards. As a result, the frequency of the gravitational wave signal will *increase* with time. At the same time, any periodic waves from the rotation of the individual stars will cause loss of rotational kinetic energy, so that this frequency will *decrease* with time. Eventually the stars will coalesce, resulting in a short intense burst of gravitational waves.

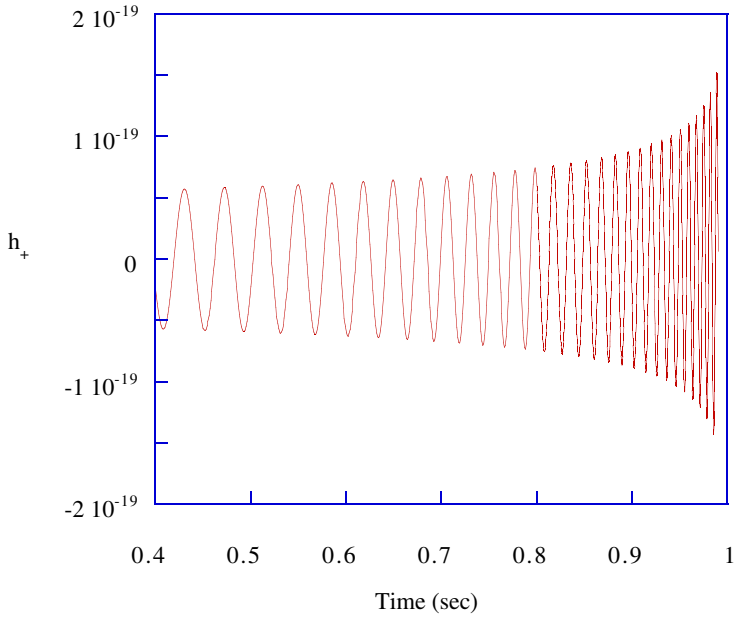

Figure 4. Predicted gravitational waveform from the inspiral of $10M_{\odot}$ black hole binaries [18]. To show the individual cycles near coalescence, the orbital frequency in this graph has been artificially reduced.

Figure 4 is a predicted gravitational waveform produced by the inspiral of a binary made of two black holes [18]. During the final minutes of a coalescing binary the waveform is highly distinctive.

The time evolution of the frequency of two $1.4M_{\odot}$ neutron stars in a binary system is shown in figure 5. Over a period of about 1000 s the frequency rises from about 10 Hz to 1 kHz as the neutron stars spiral together. This part of the merger begins when the stars are within about 1000 km of each other. The orbital velocity is $\sim 0.1c$. Signal detection can make use of exactly the same principles used to extract narrow-band signals due to the fact that the time evolution of the signal frequency and phase is predictable. Matched filtering, based on the existence of a family of accurately predictable waveforms, can allow integration over all of the observed signal cycles. A terrestrial detector may be able to observe more than 1000 gravitational wave cycles from a neutron star binary. The total number of cycles observable increases strongly as the lower cut of frequency is reduced. This provides a strong incentive for creating detectors at the lowest possible frequency. For 1000 observable cycles, the signal-to-noise ratio is improved by the square root of this number, or about 30.

Exactly the same concepts may be applied to supermassive black hole binaries. The signal frequency decreases inversely with the black hole mass. Thus a pair of 10^8 solar mass black holes would produce a chirp of gravitational waves rising from one cycle per year to a cycle per day over a period of 10^{11} s! This is much too long to observe the entire event, so in reality one could only expect to observe rather few cycles. However, since there appear to be a large population of quasars and galaxies containing massive black holes, as well as a large population of interacting galaxies, such events may not be uncommon, and may give rise to numerous strongly detectable sources at very low frequencies.

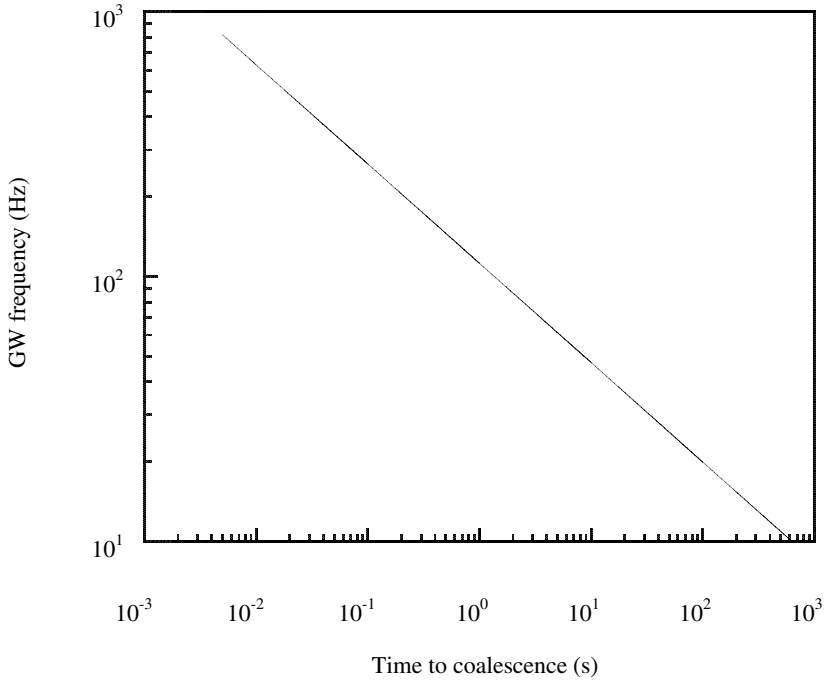

Figure 5. The frequency evolution for coalescence of a binary system consisting of a pair of $1.4M_\odot$ neutron stars.

2.3. Supernovae

Supernovae have long been considered a primary source of gravitational wave bursts. Unfortunately, astrophysics gives us few clues to their efficiency in producing gravitational waves during core collapse. Indeed, the true nature of the various supernova classes is still uncertain. In particular, it is uncertain whether a type I(a) supernova occurs through detonation or collapse in a solitary or binary white dwarf system. Some supernovae, such as the Crab supernova of the year 1054AD, do create neutron stars, but others such as supernova 1987A have failed to yield an identifiable neutron star. It is also unknown whether supernovae can directly create black holes.

The possibility of strong gravitational radiation emission only occurs if the event consists of gravitational collapse to a neutron star or black hole. Even in this case the efficiency of gravitational radiation emission is contentious. (The efficiency ε is defined as the fraction of the rest mass of the system concerned converted to gravitational waves.) Estimates of gravitational wave emission have been based on two quite independent approaches. The first follows the gravitational collapse of a system in two or three dimensions, considering as much of the physics as possible—magnetohydrodynamics, neutrino physics, and general relativity—in an attempt to deduce the time dependence of the quadrupole moment and hence the conversion efficiency to gravitational waves.

The second approach assumes that the collapse has occurred and follows the time evolution of a newly formed hot and rapidly rotating neutron star. Any phenomenon that creates non-axial symmetry will convert rotational kinetic energy into gravitational waves. In addition, convective motions, vibrational modes of oscillation of the star, and nonaxisymmetric emission of neutrinos can convert into gravitational wave emission. To date, many core collapse

calculations have predicted rather low efficiency—say 10^{-6} to 10^{-10} [19, 20], while the post-collapse evolution calculations have predicted far higher efficiencies, of order 10^{-3} to 10^{-4}. We will discuss some of these results below. However, it must be emphasized that all the models used so far are deficient due to uncertainty regarding the equation of state and the viscosity and the difficulty in constructing a full 3D numerical general relativistic hydrodynamical code which must also include magnetic and neutrino phenomena [21]. Due to the enormous difficulties involved it seems most unlikely that theory alone will be able to answer the primary observational questions on the efficiency and the waveforms generated in supernovae. However, almost all models show an unsurprising common feature: the efficiency of gravitational wave production depends on the angular momentum of the progenitor star.

Lai and Shapiro [22] have considered the time evolution of a new-born rapidly rotating neutron star. They have shown that the new-born star is driven by gravitational radiation into a non-asymmetric configuration due to a bar-mode instability. A unique gravitational wave signature ensues: the wave frequency sweeps rapidly downward from a few hundred hertz towards zero, while the wave amplitude increases rapidly from zero at the onset of the instability to a maximum at a few hundred hertz, and then reduces steadily as the frequency falls. Additional gravitational wave signals can also arise in rapidly rotating neutron stars. The rotating stars are modelled as nonaxisymmetric ellipsoids. A secularly unstable Maclaurin spheroid [23] will evolve away from the axisymmetric configuration due to gravitational radiation, and proceed ultimately toward a Dedekind ellipsoid [23].

According to Lai and Shapiro the characteristic amplitude of a gravitational wave during the evolution from a Maclaurin spheroid to a Dedekind ellipsoid is given (within 20% accuracy) by

$$h_c \sim 1.8 \times 10^{22} \left(\frac{10\ \mathrm{Mpc}}{R}\right) \left(\frac{M}{10M_\odot}\right)^{3/4} \left(\frac{r_0}{10\ \mathrm{km}}\right) f^{1/2} \tag{2.1}$$

where M and r_0 are the mass and radius of the star, respectively. Here h_c refers to the effective amplitude which takes into account the number of cycles that the signal is within the detector bandwidth (see below).

At high frequency, gravitational radiation can be expected from the evolution of a Jacobi-like ellipsoid [23] toward a Maclaurin spheroid. This Maclaurin spheroid can evolve further to a Dedekind ellipsoid. The characteristic amplitude during the Jacobi-like evolution can be fitted to the form

$$h \sim 2.7 \times 10^{-20} \left(\frac{10\ \mathrm{Mpc}}{R}\right) \left(\frac{M}{1.4M_\odot}\right)^{3/4} \left(\frac{r_0}{10\ \mathrm{km}}\right) f^{-1/5}. \tag{2.2}$$

Houser *et al* [24] have modelled the gravitational radiation from a bar-mode instability in rapidly rotating neutron stars. Their calculation using Newtonian gravity and without consideration of further collapse to a black hole, nor other hydrodynamic instabilities, gives a gravitational radiation conversion efficiency of $\varepsilon \sim 0.1\%$.

The above examples seem to indicate that supernovae which produce rapidly rotating neutron stars may be reasonably efficient sources of gravitational radiation. The nature of the production process is likely to be through shape instabilities such as those discussed, but it is unlikely that predictions of waveform are accurate. Large amounts of angular momentum may be radiated away in gravitational waves but if the duration and frequency evolution are unknown this presents an additional complication when it comes to trying to dig a signal out of the detector noise. The fraction of supernovae for which high gravitational wave emission occurs is unknown. In the following discussion where we need to use a numerical value, we shall adopt an efficiency of 0.1%. However, the uncertainty of this number must be recalled.

To start with, it is useful to note that a supernova of 0.1% efficiency produces a characteristic strain amplitude of $\sim 10^{-18}$ at 10 kpc (within our Galaxy), and 10^{-21} at 10 Mpc (halfway to the Virgo Cluster of galaxies). The chance of detecting gravitational wave bursts obviously depends strongly on the rate of the burst events. Due to the isolation of the Milky Way Galaxy, and to the large distances required to substantially increase the size of the target population, the amplitude distribution of bursts is extremely non-uniform. Strong events from our Galaxy are almost certainly rare, and to increase the event rate substantially one needs to be able to detect events in the Virgo Cluster. Thus, to have a chance of detecting several events per year, the sensitivity must be able to detect characteristic amplitudes of less than 10^{-21}.

2.4. Rough guide to signal amplitudes

It is useful to have some formulae with which to make rough estimates of signal amplitudes. For a continuous gravitational wave of frequency f_g, the strain amplitude h is related to the power density w through the relation [25, 26]

$$w \approx \frac{\pi c^3}{4G} f_g^2 \langle h^2 \rangle = 3.18 \times 10^{35} f_g^2 \langle h^2 \rangle \ \mathrm{Wm}^2. \tag{2.3}$$

where $h^2 = h_+^2 + h_\times^2$. Because of the large numerical constant in equation (2.3) the amplitude h is extremely small even for a fairly large power density. For a gravitational wave with strain amplitude of $h \sim 10^{-21}$ (typical of possible signals from the Virgo Cluster) at a frequency of 1 kHz, the flux would be 0.3 W m^{-2}, which is about 10^{20} times bigger than typical radio astrophysical energy fluxes. The strain amplitude can be written as

$$h = 4\pi R^2 w \sim \left(\frac{G}{\pi^2 c^3}\right)^{1/2} \frac{L^{1/2}}{f_g R} \sim 1.7 \times 10^{22} \left(\frac{1\ \mathrm{kHz}}{f_g}\right) \left(\frac{10\ \mathrm{Mpc}}{R}\right) \left(\frac{L}{10^{46}\ \mathrm{W}}\right)^{1/2}. \tag{2.4}$$

As we saw above, the modelling of gravitational wave forms in gravitational collapse is extremely uncertain. However, for a gravitational wave burst event, the characteristic time scale of the event τ_g, and the total gravitational energy released E_g, provide a reasonable basis for estimating source parameters. The energy radiation rate L is related to τ_g and E_g by

$$L \sim E_g/\tau_g. \tag{2.5}$$

Burst sources naturally have a broadband spectral distribution. The characteristic frequency of a burst of duration τ_g is roughly

$$f_g = \frac{1}{2\pi\tau_g}. \tag{2.6}$$

This frequency roughly defines the peak frequency in the spectrum. For a roughly Gaussian burst, the width of the spectrum Δf is of the same order of f_g. The strain amplitude can then be written as [8]

$$h \sim \left(\frac{G}{\pi^2 c^3}\right)^{1/2} \frac{(E_g/\tau_g)^{1/2}}{f_g R} \sim 5.8 \times 10^{-20} \left(\frac{E_g}{M_\odot c^2}\right)^{1/2} \left(\frac{1\ \mathrm{kHz}}{f_g}\right)^{1/2} \left(\frac{10\ \mathrm{Mpc}}{R}\right). \tag{2.7}$$

If a gravitational collapse forms a black hole, we can be more specific in estimating the event duration. Defining a characteristic time τ to be the time for the gravitational wave to travel across the region of strong gravitation d_s, which is assumed to be about twice the gravitational radius $2GM/c^2$, and assuming τ_g is approximately the same as the characteristic time τ, we have

$$\tau \sim \frac{1}{2\pi f_g} \sim \frac{d_s}{c} \sim \frac{4GM}{c^3}. \tag{2.8}$$

For a system of several solar masses, this corresponds to a frequency of a few kHz. Putting equation (2.8) into equation (2.7) and using $E_g = Mc^2$, the strain amplitude of a burst event then becomes [8]

$$h \sim \frac{1}{2\pi}\frac{c}{f_g R}\varepsilon^{1/2} \sim 5 \times 10^{-21}\left(\frac{1\ \text{kHz}}{f_g}\right)\left(\frac{10\ \text{Mpc}}{R}\right)\left(\frac{\varepsilon}{10^{-3}}\right)^{1/2}. \tag{2.9}$$

2.5. Neutron star coalescence sources

The modelling of gravitational wave emission from neutron star coalescence has been studied extensively. For most of their evolution, the neutron stars can be considered as point masses, and much of their evolution is well described by the quadrupole formula equations (1.15) and (1.16). The waveform as shown in figure 4 is quite distinctive and amenable to the method of matched filtering for signal detection. A numerical template is used, defined by the set of possible waveforms. When this is cross-correlated with the data and correctly matched in phase, it will produce a large positive correlation. The signal-to-noise ratio is substantially enhanced by this means. The apparent signal enhancement achievable is expressed in terms of the characteristic amplitude h_c. The characteristic amplitude represents the effective amplitude detected after optimal filtering of the waveform. Roughly, h_c includes an enhancement of the signal by the square root of the number of cycles within the spectral band of interest and is roughly a factor of 30 for a neutron star coalescence detected by a laser interferometer detector, although this increases strongly if the waveform is detectable at much lower frequencies where the frequency evolution is slow. For example, the number of observable cycles increases almost 50 times if the detector is able to observe down to 10 Hz instead of 100 Hz. This means that we can only roughly estimate the size of the detectable signal, as it depends on the detailed frequency response of the detector.

Thorne [18] gives the characteristic strain amplitude of the waves from inspiralling binaries as

$$h \sim 0.237\frac{\mu^{1/2}M^{1/3}}{r_0 f_c^{1/6}} = 4.1 \times 10^{-22}\left(\frac{\mu}{M_\odot}\right)^{1/2}\left(\frac{M}{M_\odot}\right)^{1/3}\left(\frac{100\ \text{Mpc}}{R}\right)\left(\frac{100\ \text{Hz}}{f_c}\right)^{1/6}. \tag{2.10}$$

Here M and μ are the total and reduced masses: $M = M_1 + M_2$, $\mu = M_1 M_2/M$, and f_c is roughly the frequency of maximum detector sensitivity.

Lai and Shapiro [22, 27] have modelled neutron star coalescence taking into account the dissipative hydrodynamics of the systems. They showed that a hydrodynamical instability arises through tidal interactions, which significantly accelerates the coalescence at small separations. This leads to a reduction in the coalescence time, and an increase in h compared with a non-viscous system, as shown in figure 6.

The rate of coalescence events is such that the chance of an event in our Galaxy is negligible. Based on the statistics of observed single and binary neutron star systems and on the supernovae rate in external galaxies [28, 29], it is estimated that the merger rate of binary neutron stars in our Galaxy is between 10^{-6} yr^{-1} and 10^{-4} yr^{-1}. For galaxies at $R \leqslant 200$ Mpc a lower limit of this rate is roughly 1–3 yr^{-1}. However, Tutukov *et al* [30] and Yamaoka *et al* [31] have shown that the above merger rate, calculated by means of statistics of observed binaries, is probably wrong because of the short lifetimes of most new-born neutron star binaries. From models based on stellar evolution, they estimate a neutron star binary merger rate up to 100 yr^{-1} in galaxies out to 200 Mpc (assuming a Hubble period of $T_{\text{Hubble}} = 1.5 \times 10^{10}$ yr, which corresponds to a Hubble constant of $H_0 \sim 66$ km s^{-1} Mpc^{-1}).

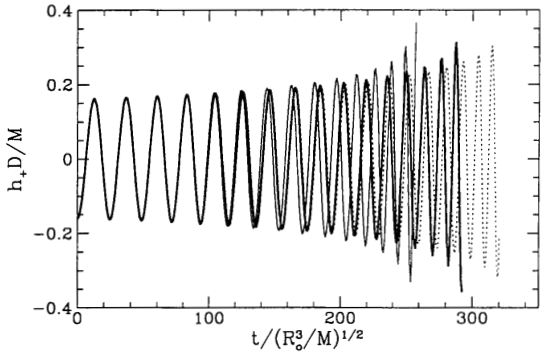

Figure 6. Waveform from neutron star binary coalescence [22]. The thick solid curve corresponds to zero viscosity. The thin solid curve assumes a mass-averaged shear kinetic viscosity $v = 0.5(M/r_0)^{1/2}$, where M and r_0 are the mass and the radius of the star respectively. The dotted curve is the case for two point masses (i.e. as figure 4).

The neutron star coalescence signals amplitude and waveform can be predicted with reasonable confidence, so that such sources are certain to be detected when sufficient sensitivity is achieved. The burst sources are also very promising for advanced gravitational wave detectors [32–34], but suffer from uncertainty in the value of ε. From equation (2.9), the gravitational wave strain amplitude for burst events at 200 Mpc is comparable to that from binary coalescence if $\varepsilon \sim 0.01$. In this case, the event rate will be much greater.

From the estimation of the stellar population with distance, the merger rate would be $\sim$0.1 yr^{-1} for a distance of $R \sim 20$ Mpc, the typical distance to the Virgo Cluster. The burst rate by contrast could be 30 yr^{-1} [35].

2.6. Low-frequency sources

As discussed above, very intense low-frequency gravitational wave sources can be expected from gravitational waves associated with the merger of massive black holes. Rees [36,37] has argued that massive black holes are inevitable in the cores of young galaxies. There is very strong evidence that such black holes exist in many objects, with masses ranging from 10^6 to 10^9 solar masses. Galactic mergers are likely to give rise to such black hole mergers so one estimate of the rate of powerful gravity wave events can be obtained by estimating the rate of galactic mergers. For large galaxies with central black holes, Haehnelt [38] has estimated this rate at about one per century. This does not include the far more frequent mergers of smaller galaxies for which central black holes have not been confirmed. Vecchio [39] has shown that for the black hole merger rate to reach one per year practically all galaxies out to $z = 1$ would have to contribute black holes to feed the merger process. The latter is not such a strong constraint, however, since the horizon for detecting black hole mergers could be far beyond $z = 1$. For example, if one considers mergers to $z = 3$, only a few per cent of galaxies are required to have a central black hole to achieve one event per year.

Potentially detectable low-frequency gravitational waves can also be created by low-mass objects orbiting massive black holes. The low-mass objects could be smaller black holes or neutron stars, white dwarfs or even main sequence stars. Such sources could exist in the nucleus of our own Galaxy, and could in principle be detectable well beyond the Virgo Cluster (which multiplies up the number of potential sources by several thousand).

The basic physics behind gravity wave emission from sources of this type relates to the question of whether the gravity gradient from the central black hole is sufficient to tidally disrupt the incoming object. Clearly, main sequence stars will be most easily disrupted. Only if the central black hole is capable of swallowing whole the incoming object, will the gravitational radiation be strong. Otherwise the tidally disrupted star will form an accretion disc and slowly

accrete the material with negligible gravitational wave emission. To avoid tidal disruption, the Schwartzchild radius of the black hole must be large compared with the radius of the infalling object. Roughly, the central black hole must be 10^7–10^8 solar masses for main sequence stars, 10^4 solar masses for white dwarfs, and 10 solar masses for neutron stars.

Sigurdsson [40] has estimated the rate of capture of stellar mass black holes by massive black holes in galactic nuclei. The gravitational potential of the central black hole creates a cusp-like stellar density profile. It is difficult to estimate the space density of objects in the central cusp. It depends on star formation in the central high-density region of galaxies. However, the population in the cusp will never achieve dynamic equilibrium because stars approaching too close to the central black hole will be lost into the hole. Sigurdsson estimates the rate of black hole capture by a central object as 10^{-8} per year, meaning that a realistic detectable rate (one per year) requires observations to a range of the order of 3 Gpc. If the high densities in galactic nuclei favour higher mass star formation the event rate could increase by an order of magnitude.

2.7. Gravitational waves from binary systems

Short-period binary systems can create interesting amplitudes of gravitational waves in the 10^{-1}–10^{-5} Hz range. Such binaries exist in several classes. One of the most definite classes consist of the W Ursa Majoris binaries (WUMas), which are contact binary stars, with orbital periods of hours. They are generally low-mass systems. About one star in 150 with mass $>0.6M_\odot$ is a contact binary [41]. Lower mass binaries are difficult to detect: there could be an equal population of such systems with even shorter orbital periods.

A second important class of short-period binary stars are the cataclysmic variables, consisting of an interacting main sequence and white dwarf binary. Cataclysmic variables have orbital periods in the range 1000 s to one day: the shortest-period systems are probably white-dwarf–white-dwarf systems.

Neutron star binaries occur in various forms, from the NS–NS binaries such as the Hulse–Taylor pulsar PSR 1913 + 16, to rather more common systems in which neutron stars have white dwarf or main sequence star companions. The latter often occur as interacting binaries—low-mass or high-mass x-ray binaries, in which x-ray emission occurs due to mass transfer on to the neutron star.

Verbunt [42] has summarized the density and strain amplitude expected from the short-period binary star systems. Table 1 below is based on his review. The table shows the rough number density and mass parameters, and the distances of typical sources. Most produce gravitational waves $\sim 10^{-3}$–10^{-4} Hz, at an amplitude $\sim 10^{-20}$–10^{-22}. There is clearly an abundance of sources in the categories of nearby sources ($<$100 pc), such that the total population creates a stochastic background of gravitational wave noise.

Several x-ray binary systems have been shown to contain neutron stars spinning in the range 250–350 Hz. It is suggested that their spin rate is determined by the balance between the mass accretion which provides a source of energy and angular momentum, and gravitational wave emission which is the dominant energy sink. Emission could occur by a variety of symmetry breaking instabilities. A specific suggestion is the so called r-mode instability, in which rotational fluid flow patterns are induced in the neutron star [43].

Stellar evolution studies suggest that globular clusters are a breeding ground for close-spaced binary black holes [44]. It has been recently suggested that these binaries get ejected from globular clusters by three-body interactions, creating a halo population of binaries which will coalesce in less than a Hubble time. Such binaries might coalesce without electromagnetic signature, and could have a sufficiently large population that they could be detected at a

Table 1. Binary sources of low frequency gravitational waves. The table shows the rough galactic density of each source, the distance within which sources are expected, the typical mass of each binary component, and the typical frequency and strain amplitude from the nearest sources.

Type	Density/number	d (pc)	$M/M_\odot$	$m/M_\odot$	$\log f$ (s^{-1})	$\log h$
WUMa (0.3–0.6$M_\odot$)	2×10^{-4} pc^{-3}	15	0.6	0.3	−4.0	−20.4
WUMa (0.1–0.3$M_\odot$)	2×10^{-4} pc^{-3}	15	0.3	0.1	−3.7	−20.7
Cataclysmic variables	10^{-5} pc^{-3}	45	0.3	0.6	−3.7	−20.7
Double degenerates (AM CVn)		100	0.04	0.6	−2.7	−21.2
Low-mass x-ray binaries ($P_b < 2 \times 10^{-4}$ s)	30	1 000	0.4	1.4	−3.8	−21.7
Low-mass binary pulsars (PSR 2051-08)		1 300	0.03	1.4	−3.8	−21.7
High-mass x-ray binaries (Cyg X-3)	1	10 000	4.0	1.4	−3.9	−21.9
NS–NS binary pulsars (1913 + 16)	$<10^{-5}$	500	1.4	1.4	−3.7	−20.8
Binaries in globular clusters (4U1820-30)		8 100	0.06	1.4	−2.5	−22.3

reasonable rate at $h \sim 10^{-21}$.

Gamma ray bursts which emit energy comparable to a solar mass at cosmological distances could be due to the formation of black holes, or to neutron star binary coalescence, or to the coalescence of neutron-star–black-hole binaries. Except in the case of spherically symmetrical black hole formation, these mechanisms should all include strong gravitational wave bursts. Searches have failed to find correlations between bursts and existing detectors, but this is not unexpected as sensitivity is still not high enough.

Neutron star black hole coalescences, whether or not they are associated with gamma bursts, can allow neutron star structure and microphysics to be probed because the break point in the coalescence waveform is set by the tidal disruption of the neutron star. This depends strongly on the neutron star radius and equation of state.

2.8. Stochastic background from the era of early star formation

We now consider the effects of supernovae and neutron star births at cosmological distances. In this case, we are extrapolating from a radius of 10 Mpc to a radius of several Gpc. For example, we consider supernovae from galaxies at redshift $z = 2$. Such galaxies are much older than massive stellar lifetimes, and the rate of supernovae in such systems is generally thought to be 10–100 times greater than supernovae in contemporary galaxies [45]. This is supported by observations by Cowie *et al* [46] which indicate a fourfold enhancement in faint blue galaxies at $z \geqslant 1$. At greater distances, millimetre wavelength studies of the Hubble deep field region show the presence very-high-luminosity objects consistent with dust-enshrouded galaxies at $z \sim 2$–4. Observations indicate that star formation is occurring at rates ∼50 times that in the present epoch [47]. The significance of these increased star formation rates, and hence increased supernova rates, is that it leads to the possibility that the gravitational waves from supernovae create a nearly continuous stochastic background.

First consider a simple case. Suppose that all supernovae have a gravitational wave burst duration τ, and a mean rate of occurrence within some horizon distance (say 3 Gpc), of R bursts per second. Then the mean duty cycle D of supernova bursts is given by $D = R\tau$. If $\tau \sim 10^{-3}$ s, then D reaches unity when R reaches 3×10^{10} y^{-1}, or 10^3 s^{-1}. When D reaches unity the supernova bursts create an effectively continuous stochastic background. To make an accurate determination of the supernova stochastic background, one needs to take into account both evolutionary effects and cosmological effects. If every population I (second-generation) star was the result of a single prior supernova, then there would need to have been $\sim 10^{21}$ supernovae to create the observed population of second-generation stars. This corresponds

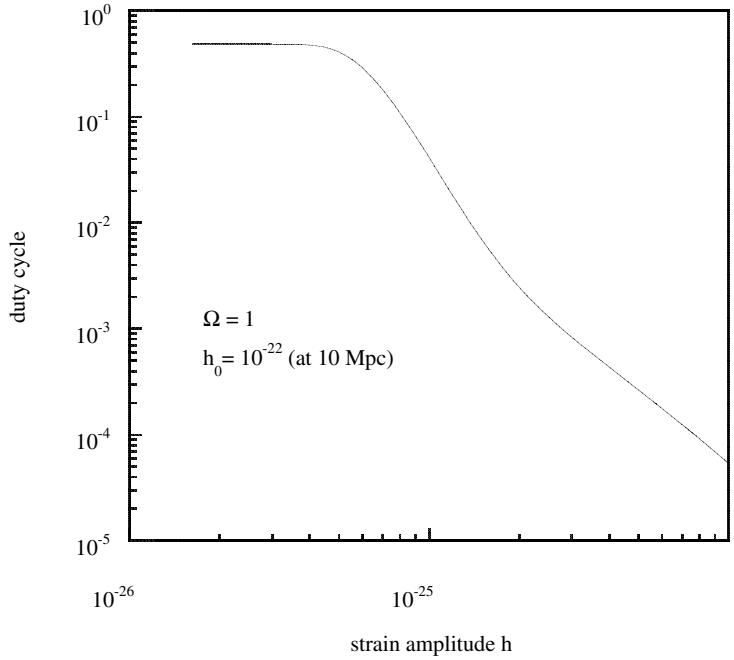

Figure 7. Duty cycle versus strain amplitude for supernova-generated gravitational radiation (with an initial Gaussian burst of star formation at $z = 2$) [49].

to an average rate Excedrin 1000 supernovae s^{-1}. Redshifts both stretch the pulses and the mean time between bursts. The luminosity distance in non-Euclidean geometry changes the observed amplitude of each burst.

A preliminary analysis in flat spacetime with assumed star formation rates showed that the event rate could be as high as 10^4 s^{-1} [48]. Burman *et al* [49] refined the predictions of [48] using various predictions for star formation rates to determine the duty cycle of short bursts of gravitational waves from supernovae within the observable universe for various cosmological models. Ferrari *et al* have separately considered supernovae [50] and gravitational waves from young neuron stars [51]. They obtained event rates $\sim$20 s^{-1}.

Figure 7 gives a typical result [49]. This result uses a Gaussian burst of star formation about $z = 2$. It shows the burst amplitude versus duty cycle for supernovae assumed to have an amplitude $h_0 = 10^{-22}$ at 10 Mpc. The background can only be considered a true stochastic background as D tends to unity: for this model this occurs at $h \sim 10^{-25}$. Most of this signal is due to events occurring during the initial burst of star formation. The amplitude of this stochastic background will be characteristic of the more distant sources at $z = 2$.

Like all stochastic backgrounds, the supernova background can in principle be detected by cross-correlation of signals between nearby detectors (less than half a wavelength separation: for $\tau \sim 10^{-3}$ s, they should be less than 100 km apart) [52]. As discussed above, the signal-to-noise ratio is increased as the $\frac{1}{4}$ power of the effective measurement time defined by the cross-correlation integration time. For 10^7 s, integration at 1 kHz, this represents a 300-fold improvement. Thus, the combined effects of all supernovae is to create a signal which can be detected at a signal-to-noise ratio comparable to that of an individual supernova at 20–30 Mpc. Thus, a detector capable of detection extragalactic supernovae can, with cross-correlation, detect a stochastic background produced at 30 times greater distance.

There are other aspects of the supernova stochastic background which are worth mentioning. Its spectrum represents the average spectrum over all supernovae, but it will be reddened according to the contribution of high-redshift supernovae. The duty cycle is clearly amplitude dependent. Nearer sources will create less-frequent, larger-amplitude bursts. At low duty cycle the background will be like popcorn noise, while for $D > 1$, it will approximate Gaussian noise. There is an important difference in this regard. The presence of a popcorn noise component [53] means that unlike true white noise, the individual short bursts create broadband intensity correlations which might allow more powerful digging into the noise. For example, the broadband correlations might allow the background to be detected as spectral intensity correlations within a single detector. This might be combined with cross-correlation between two detectors to dig still deeper into the noise. Further work in this area is badly needed.

The energy density of the supernovae background Ω_{SN}, expressed as a fraction of closure density, is given by

$$\Omega_{SN} = \Omega f_s f_{SN} \bar{\varepsilon} \tag{2.11}$$

where Ω is the usual fraction of closure density for the universe as a whole, f_S is the fraction of this matter which forms into stars in a Hubble time, f_{SN} is the mass fraction which takes part in supernova events in a Hubble time, and $\bar{\varepsilon}$ the mean gravity wave conversion efficiency for supernovae. It is possible that Ω_{SN} could be in the range 10^{-6}–10^{-8}. However, if $\bar{\varepsilon}$ is low and the duty cycle is low, Ω_{SN} could be $\ll 10^{-10}$.

If the majority of the gravitational waves are generated in relatively long duration spin-downs of neutron stars the spectrum will be dominated by a continuous stochastic component, but if it is emitted in short supernova bursts, the popcorn component will dominates. If the energy density of the early star formation stochastic background is $\sim 10^{-8}$, then it should be eventually detectable by pairs of advanced detectors [54].

To show the signals on the same scale, which relates to detectability, stochastic sources are assumed to have been integrated up for times $\sim 10^8$ s, binary coalescences have been integrated over the coalescence frequency range, while the burst sources signal strengths are the only ones representing the instantaneous signal amplitude.

Finally, to summarize our discussion of sources, we present a graph (figure 8) containing estimates of various events. The comparison is approximate, as it compares various sources detected by various techniques. Supernovae signals would appear as bursts requiring no special signal processing. However, estimates must allow for a wide range of efficiencies and source distances. Black hole formation is similarly uncertain.

2.9. Cosmological gravitational waves from the big bang

Various sources of gravitational waves from the early universe have been hypothesized. These may be thought of as the gravitational wave analogue of the microwave cosmic background radiation. The cosmic microwave background originated at the epoch of last scattering, at a redshift $z \sim 10^3$ when neutral gas first formed in the universe. Thus, the microwave background probes the universe when it was $\sim 10^5$ years old. A similar background of neutrinos should also exist, a relic from their epoch of last scattering, about 0.1 s after the big bang, at a redshift $z \sim 10^{10}$. Due to the weak coupling of gravitational waves with matter, their epoch of release would have been much earlier still, at around the Planck time $\sim 10^{-43}$ s, or $z \sim 10^{30}$.

Thus primordial gravitational waves offer the tantalizing possibility of probing the universe very near to the moment of creation. Unfortunately, we do not have accurate predictions about their amplitude. It has been suggested that the background could have been parametrically

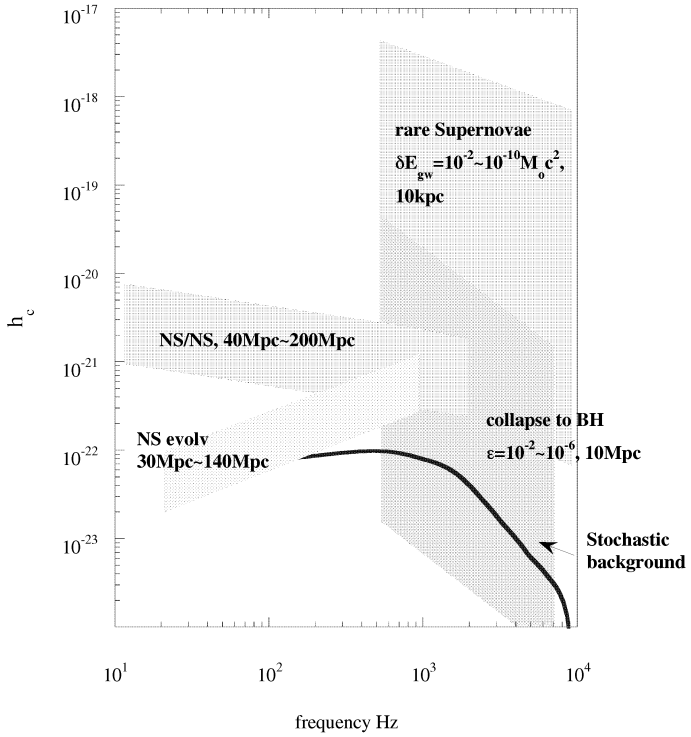

Figure 8. Spectrum of gravitational wave sources [18, 22]. In this figure, the abbreviations are: BH, collapse to black hole; NS/NS, neutron star coalescence; NS evol, secular evolution of a nonaxisymmetric neutron star.

amplified during a period of inflation, or that phase transitions in the early universe (for which there is no experimental evidence) could have created an enhanced background. If there was no process to enhance the background amplitude, then we need consider simply a thermal background that was in equilibrium at the extremely high energies of the Planck era. The background will then have been redshifted like any other radiation. Today this radiation would be in the microwave regime and have an amplitude $h \sim 10^{-35}$, which is beyond the possibility of detection.

If the universe contained an initial inhomogeneity of amplitude h_g [55], then today it would have an amplitude at frequency f given roughly by

$$h \sim 10^{-20} h_g / f. \tag{2.12}$$

We have little idea of the initial amplitude, except for limits set by the cosmic microwave background which implies that inhomogeneities traced by matter had an amplitude $\sim 10^{-5}$. This would imply that the cosmological background amplitude could be 10^{-28} at 1 kHz, (which is beyond terrestrial experiments) and 10^{-21} at 10^{-4} Hz, (which is experimentally accessible by space laser interferometers).

A constraint on the cosmological background is set by considering the energy density, and relating it to cosmological models. Thus cosmological backgrounds are often parametrized in terms of the closure density fraction Ω_g. If the spectrum contains equal energy in each decade, it has a slope of -1 on a $\log h$–$\log f$ plot. For example, for the universe to be closed by gravitational waves, $\Omega_g = 1$, the amplitude h_g would be 10^{-13} at 10^{-5} Hz, falling to 10^{-21} at 1 kHz. For $\Omega_g = 10^{-6}$, h_g falls by three orders of magnitude to 10^{-16} at 10^{-5} Hz and 10^{-24} at 1 kHz.

It would appear most unlikely that the universe be closed by gravitational waves, and it would be surprising if gravitational waves contributed significantly to the missing mass. The binary pulsar, in addition to confirming the emission of gravitational waves, also allows limits

to be set on the stochastic background of gravitational waves, and on the time variation of the gravitational constant. Taylor and co-workers [56] have used pulsar timing of the binary pulsar PSR 1913 + 16 to set limits on cosmological backgrounds. The method only works at very low frequencies where both pulsars and atomic frequency standards have sufficient frequency precision that measurement of the arrival time variations of pulsar signals gives useful sensitivity to gravitational waves. Taylor's timing measurements over several years set a limit to $\Omega_g \sim 4 \times 10^{-2}$ in the frequency range 10^{-9} to 10^{-12} Hz [56].

3. Detection of gravitational waves

3.1. An overview of detector technology

The development of gravitational wave detectors was pioneered by Joseph Weber in the early 1960s [4]. He used a massive aluminium bar as the antenna. Following his work, researchers all over the world have been working hard to build different types of gravitational wave detectors. The detection of gravitational waves is based on the following idea (as discussed in section 1.2). A gravitational wave can be considered as a time-dependent strain in space having two linear polarization states (h_+ and $h_\times$). When the wave passes test masses in space it will cause displacements of the test masses, as shown in figure 1. A measurement of the relative displacements of the test masses is a measure of the wave. The gravitational wave does work on electromagnetic field, such as a capacitance or a laser light field. Because the displacements are very small, the momentum of the gravitational wave is in general limited by the uncertainty principle. The *quantum limit* presents a significant but not insurmountable barrier for future detectors.

A gravitational wave detector can be constructed from a pair of masses which can move 'freely' with respect to each other. They can be suspended as pendulums, so that in the horizontal direction they can be treated as nearly free masses above the pendulum resonant frequency. A pair of masses connected by a spring (figure 9(*a*)) can also be used to form a *resonant* gravitational wave detector. Such a mechanical resonator will be driven by a gravitational wave as long as it has spectral components at the resonant frequency of the mass–spring system. If the detector is a high-Q resonator, it will continue to oscillate long after the gravitational wave has passed. That is, the resonator *remembers* the effect of the gravitational wave. A measure of the oscillation of the resonator will give information about the passing gravitational wave.

The resonator need not necessarily be two masses connected by a spring. A lump of metal such as a cylindrical bar is well suited to the purpose (figure 9(*b*)). The difference between the bar detector and two point masses with a spring in between is that the bar detector has a set of higher-order resonant modes. However, for the lowest resonant frequency, the bar can be modelled just like two masses connected by a spring, with an effective mass equal to half the mass of the idealized detector. A multi-spring mass resonator (figure 9(*c*)) can be constructed to detect not only the amplitude of the gravitational waves but also the direction of the waves. This leads to the idea of a spherical antenna [34, 57–59], as shown in figure 9(*d*).

All resonant-mass detectors use cryogenic techniques to reduce the thermal noise and to enable the use of high-sensitivity superconducting transducers. A high Q-factor ensures that the thermal noise (which even after locking has a very large amplitude compared with the signal) is manifested as a highly sinusoidal, and hence predictable, waveform. A gravitational wave induces a small change in the amplitude and phase of this waveform. Typically, the memory effect is used to resolve the signal component averaged over perhaps a few hundred cycles of the antenna. The time over which the signal can be resolved depends most strongly on

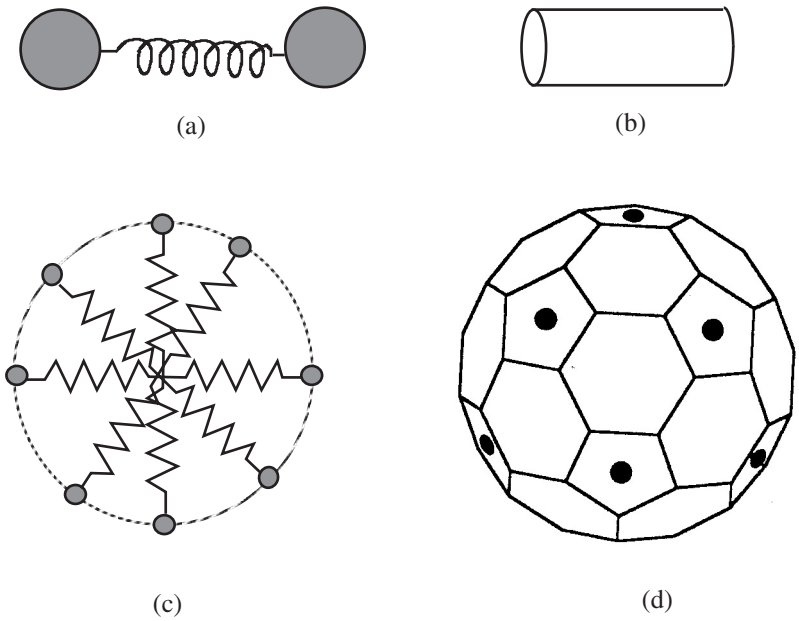

Figure 9. Model of resonant-mass gravitational wave detectors. (*a*) Two masses joined by a spring. (*b*) Bar detector. (*c*) Multi-spring mass detector. (*d*) Spherical detector, in this case formulated as a truncated icosahedron, with six transducers located as indicated.

the sensitivity and electromechanical coupling of the transducer which is used on the antenna. If the transducer is sufficiently strongly coupled, the signal could be resolved in perhaps a single cycle, and then the measured bandwidth would be comparable to the antenna frequency. Practical bar antennas to date have only demonstrated bandwidth of about 10 Hz. However, improved transducers should soon allow the bandwidth to reach $\sim$100 Hz and eventually near-quantum-limited sensitivity [60–63].

As indicated in figure 1, a passing gravitational wave will make a ring of particles stretch and shrink alternately in orthogonal directions. An interferometer configuration which can detect the relative position change between two orthogonal masses is a natural detector configuration [64–66], as shown in figure 10. When a gravitational wave passes, the lengths of the two arms of the interferometer change in antiphase. This results in a change in the interference intensity at the output. This change in light intensity is a measure of the gravitational wave. Since the test masses simply follow the passing wave pattern, these devices can be expected to accurately trace the waveform. The advantage of this type of system is the nonresonant feature and the fact that the scale of an instrument is set, not by the velocity of sound (which limits a resonant bar to a few metres in length if the detector is to detect radiation at $\sim$1 kHz), but by the velocity of light. Thus, a laser interferometer can detect gravitational waves over a wide band of frequencies and can in principle be scaled up to 150 km arm length, (for the same 1 kHz upper frequency) for which the absolute displacement $\Delta L = hL$ is much larger. Because 150 km arm length is impossible on the surface of the Earth (due to the curvature of the Earth), practical instruments must be scaled down to several kilometres.

In reality, the problem of noise always limits the bandwidth of laser interferometers. In their widest bandwidth configuration laser interferometers are limited by seismic and thermal noise at low frequency and photon shot noise at high frequency, as we discuss in detail in

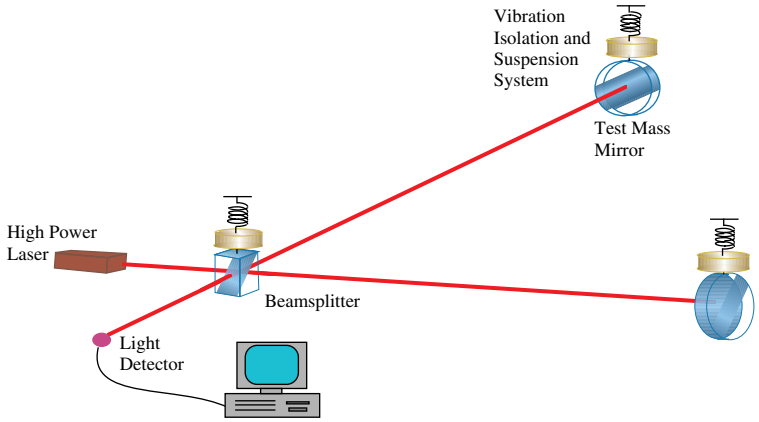

Figure 10. Schematic diagram of a Michelson interferometer for use as a gravitational wave detector.

section 5. This leaves a high-sensitivity bandwidth in the 100–500 Hz range. Optical tuning can in principle be used to restrict the bandwidth considerably, allowing optimum sensitivity to be achieved in narrower bands of several tens of Hz anywhere in the 10 Hz to several kHz range.

There is not a similar size constraint if a laser interferometer detector is placed in space. Laser interferometers can be conceived, of scale size millions of kilometres, in Earth or solar orbit. In this case practical considerations make such devices best suited to search for low-frequency sources in the range of 10^{-1} to 10^{-5} Hz. Free-floating spacecraft carrying test masses shielded from the solar wind, and low-power lasers should be able to achieve very high sensitivity, limited eventually by the confusion limit of gravitational wave 'noise' from the large number of binary star sources in the Galaxy (see section 3.2 for further discussion).

At even lower frequencies, signals from pulsars have been used as gravitational wave detectors. Pulsars, and especially millisecond pulsars, represent precise-frequency sources, close to the limit of the best man-made clocks. While we are accustomed to thinking of gravitational waves changing the relative spacing of test masses, this picture can be confusing when thinking of a pulsar as one of the test masses perhaps 1000 light years away. It is easier to consider the pulsar beam passing through the curved spacetime due to the passage of very-low-frequency gravitational waves in the vicinity of the Earth. (Both pictures are equivalent however.) The result is that the gravitational wave causes changes in the arrival time of the pulsar signal. Because the pulsar signal is weak, and because atomic clocks give best precision over long periods of time, the optimum precision of this method of detection occurs for frequencies $\sim 10^{-7}$ to 10^{-8} Hz [56].

Interferometric detection has the advantage that it gives intrinsic immunity to laser frequency noise. Indeed, a laser interferometer can in principle use white light. However, any single-beam detector is sensitive to frequency fluctuations in the source. The sensitivity limit is set directly by the frequency stability of the radiation source: $h \sim \Delta f/f$. Since frequencies can only be compared against a standard, the limit of a single-beam detector such as a pulsar signal is either the stability of the pulsar, or the stability of the frequency reference: today $\Delta f/f \sim 10^{-16}$.

The pulsar timing technique can to some extent avoid this single-beam clock stability problem by using several pulsars in different directions. A gravitational wave creates correlated fluctuations depending on the pulsar direction so that in principle it should be possible to dig at least an order of magnitude below the clock stability limit. Unfortunately, solar wind refractive

effects and interstellar scintillation are very strong in the MHz–GHz frequency range of strong pulsar signals. This provides an additional noise source that could mimic a gravitational wave.

There is no need in principle to rely on pulsars to provide the timing source for single or multibeam detection of gravitational waves. Interplanetary spacecraft generally transpond a ground-station-generated precision clock frequency back to the ground station. Comparison of the return signal frequency and the transmitted frequency predominantly records the spacecraft velocity, seen as a Doppler shift. Gravitational waves will appear as a perturbation in the Doppler tracking signal. Because the signal strength is stronger than for pulsars, and the path lengths are shorter, Doppler tracking is sensitive in the 10^{-4} to 10^{-5} Hz band. Solar wind refraction is again a very serious limit, but in this case it could be overcome if tracking took place at various frequencies, and if the frequencies used were increased into the millimetre wavelength range. Doppler tracking experiments [67, 68] have taken place successfully as low-cost add-ons to space missions, but the technique is unlikely to compete with space laser interferometers. Future interplanetary spacecraft equipped with nanosecond pulsed lasers avoid all local refractive errors from solar plasma, but solar wind buffeting causes additional noise which must be overcome by drag-free spacecraft technology.

3.2. Space laser interferometer gravitational wave detectors

A joint NASA–ESA space mission has been proposed, to place into solar orbit a set of three laser transponding spacecraft which would form a space laser interferometer for gravitational wave detection. The idea is to create a nested set of interferometers in a triangular configuration, and to use active transponding rather than passive interferometry as used in terrestrial detectors. The space environment allows the path length to be increased to 5 million kilometres. Consider first one vertex of the triangle. A pair of stabilized CW laser beams are transmitted through telescopes in 60° Y-shaped arms of the spacecraft, to two identical target spacecraft 5 million kilometres away. Each receives a very weak signal, but one sufficient to allow an on-board laser to be coherently phase locked to the incoming beam with a slight offset frequency. This laser is then directed back to the originating spacecraft. Thus the distant spacecraft acts like an active mirror, returning the incoming signal to its origin.

LISA (laser interferometer space antenna) as proposed uses three spacecraft in a special solar orbit. All six laser beams create three independent Michelson interferometers. The incoming beam at each arm has its phase compared (by beating) with some of the outgoing signal. That effectively measures the changes in the length of one arm. The same measurement is done in the second arm by the second laser beam. The phase differences are compared, to create a monitor of the arm length differences which could indicate the passage of a gravitational wave.

The above concept can give excellent sensitivity, as shown in the sensitivity curve for LISA in figure 11. This is only achieved if many noise sources are greatly reduced. The first is the buffeting by the solar wind. To overcome this noise the spacecraft are centred around a free-floating test mass, which is shielded from the wind. The spacecraft are controlled by miniature ion drives—field emission electric propulsion thrusters—to maintain the spacecraft location centred on the test mass. The forces required are $\sim 10^{-6}$ N.

A second potential source of noise is the gravity gradient due to the thermal expansion and contraction of the spacecraft structure. This can be overcome with careful design and thermal shielding.

To be able to use low-power thrusters the spacecraft must be placed in an orbit in which their relative positions have very high intrinsic stability. An orbit that achieves this requirement [69] is a heliocentric orbit of about 1 AU, 20° behind the Earth. The orbits of the spacecraft have a small eccentricity of $e = d/(D\sqrt{3})$, and a small inclination $i = d/D$, where d is the

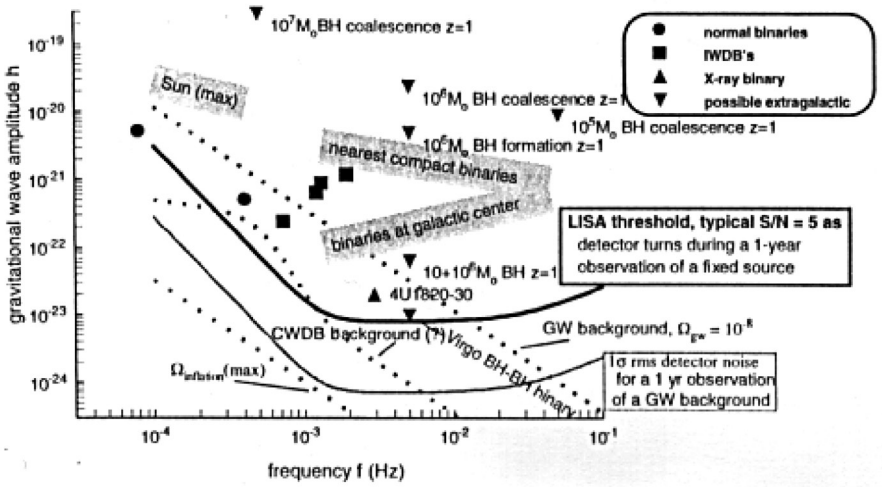

Figure 11. The sensitivity curve of LISA, along with its prime gravitational wave sources [322]. This is the sensitivity achieved after one year of integration.

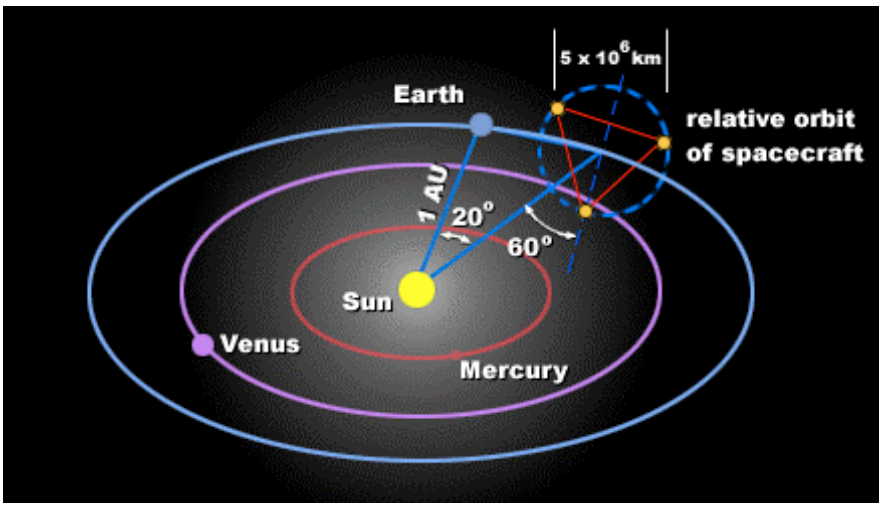

Figure 12. The positions of the proposed LISA spacecraft in heliocentric orbit [323].

triangle arm length and $D = 1$ AU is the semimajor axis of the orbit. Remarkably, three pairs of spacecraft in these orbits, with careful specification of their nodes, appears to maintain a nearly 'rigid' configuration which rotates slowly while maintaining the triangle in a plane which is inclined at 60° to the ecliptic. The positions of the spacecraft are shown in figure 12.

An important question is the orbital stability. If the relative spacing of the satellites changes too rapidly the fringe rate becomes high and the noise contribution from the local oscillator (which is used to apply frequency offsets and measures the fringe rate) becomes relatively larger. Thus it is essential that the fringe rate be low. Ideally the difference in arm length changes between two arms should be reduced to mm s^{-1}, less than the nominal metres per second arm length changes predicted for the proposed orbits. Stabilization schemes for the

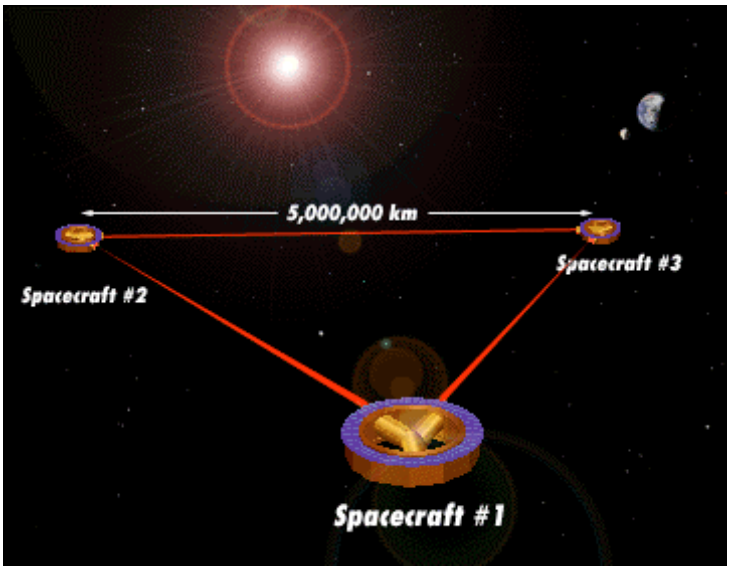

Figure 13. Artist's impression of space interferometer (LISA).

local oscillator through modulating the light in one arm or through the use of improved local oscillators should allow these problems to be overcome. Spacecraft manoeuvres are required occasionally to compensate for accumulated orbital drift.

Figure 13 shows an artist's impression of this remarkably ambitious conception. A large team of scientists is pursuing this project, which should fly in the second decade of the twenty-first century. More details are available from the LISA web page (http://lisa.ipl.nasa.gov/).

3.3. The world array of resonant-mass detectors

The improvement of resonant-bar detectors since they were first reported by Weber has been enormous. Their amplitude sensitivity has been increased several hundred times, corresponding to an improvement in flux sensitivity of about five orders of magnitude. Current detectors are sensitive to narrow frequency bands near 700 Hz and 900 Hz, but improvements will increase the bandwidth of each to >50 Hz. Figure 14 shows one of the present resonant-bar detectors.

An array of five resonant-mass gravitational wave detectors, coordinated under the International Gravitational Events Collaboration is in operation [70, 71, 110, 114, 156]. The detectors are located at Baton Rouge (Louisiana), CERN (Geneva), Legnaro (near Padova), Frascati (near Rome) and Perth (Australia). The data are available at a web address (http://axln01.lnl.infn.it/igec/). Since 1993 between two and four antennas have been in coincident operation searching for bursts at a strain sensitivity better than 10^{-18} (see figure 16). This is sufficient to detect strong galactic gravitational wave bursts, but insufficient for detection beyond our Galaxy. Over the past two decades the limits to the strength and rate of gravitational wave burst events impinging on the Earth has been reduced substantially, but these limits are still below astrophysical predictions. Thus, so far, it can be stated that the rate of gravitational wave bursts is not two orders of magnitude greater than expected from conservative astrophysical predictions, or else that their strength is not at the high end of predicted signal strengths ($\varepsilon > 10^{-2}$, see figure 29 for quantitative results).

Figure 14. Photograph of the antenna NAUTILUS at Frascati, showing the bar and its cryogenic shields.

The resonant bars have been used for rather deep pulsar searches in certain directions ($h \sim 10^{-23}$) [71] (see figure 30) and, by using cross-correlation, have been used to set impressive limits on the stochastic background of gravitational waves ($h \sim 10^{-22}$) [84].

Some of the resonant-bar detectors are being improved with better transducers and amplifiers, allowing their bandwidth to be increased towards 100 Hz. This improves the burst sensitivity and time resolution which in the immediate future should allow an order-of-magnitude improvement in burst sensitivity. Efforts are underway to create quantum-limited transducer systems (e.g. [72]) which should eventually allow a further order-of-magnitude improvement in amplitude sensitivity.

To match the ultimate sensitivity of long-baseline laser interferometer detectors (see below), it is necessary to increase detector mass from a few tonnes to a few hundred tonnes. Such massive spherical detectors have been proposed and development work is underway on small prototypes in Frascati, Leiden, and Sao Paulo [73–75]. As already noted they have the advantage of omnidirectional sensitivity. They use the proven cryogenic techniques of the existing resonant-mass detectors, but to scale up to hundred tonnes represents an exciting major engineering challenge (see section 4.10 for more details).

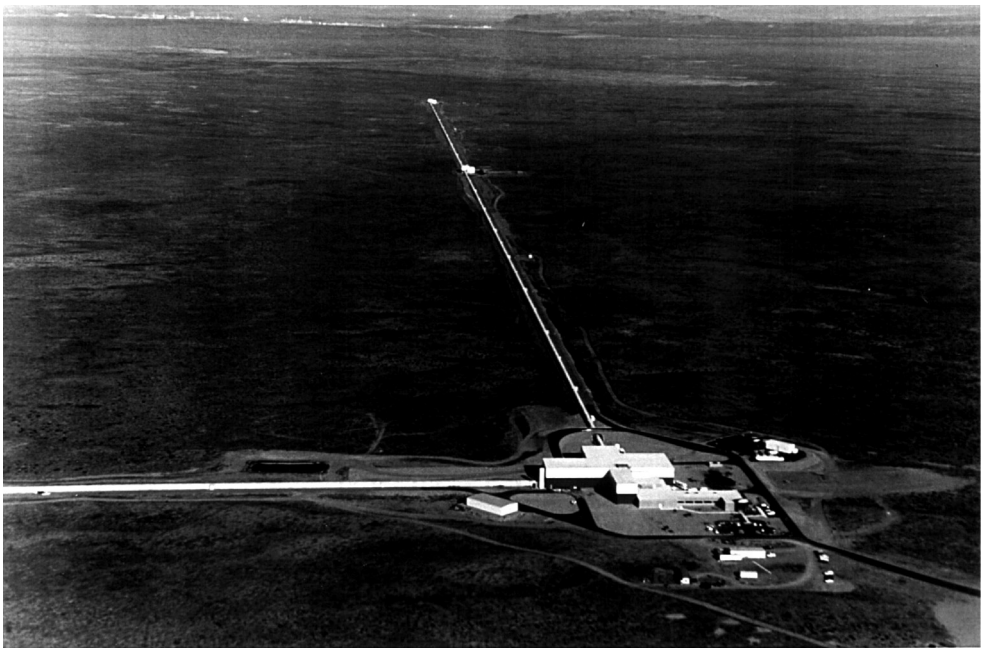

(*a*)

(*b*)

Figure 15. The LIGO detector at Hanford. (*a*) An aerial view, (*b*) the vacuum pipe tunnel and (*c*) the main cornerstation.

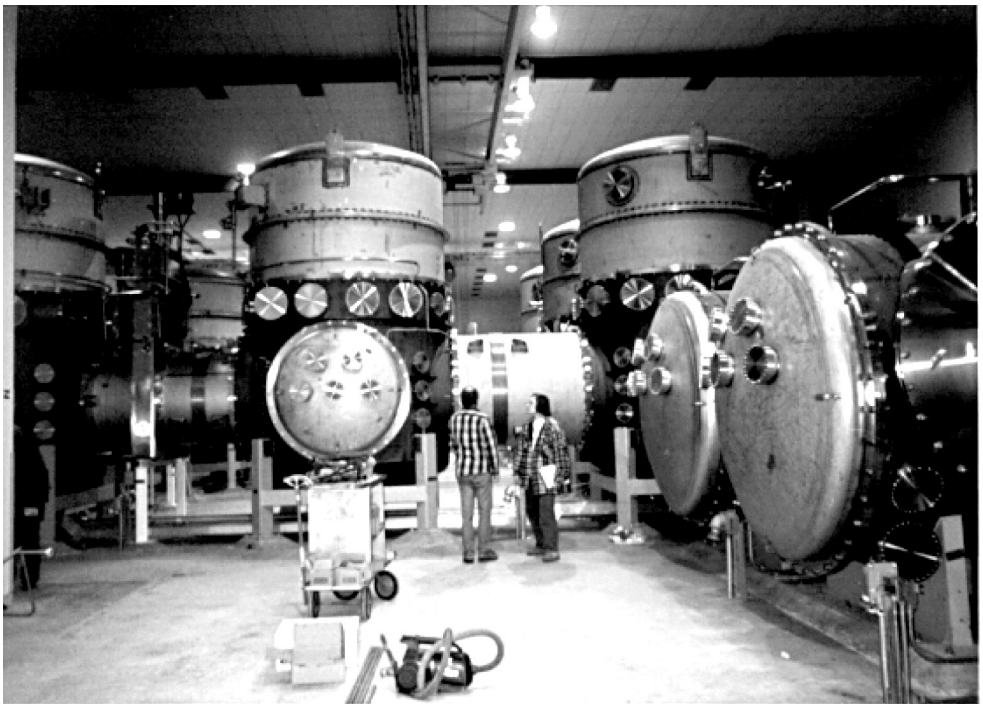

(*c*)

Figure 15. (Continued)

3.4. Laser interferometer detectors

Three long-baseline laser interferometer gravitational wave detectors have been or are being constructed. The US LIGO Laboratory consists of two 4 km arm length detectors, at Hanford, Washington State, and Livingstone, Louisiana (http://www.ligo.caltech.edu). The Italian/French VIRGO project is completing a 3 km arm length instrument at Casina, near Pisa (http://www.virgo.infn.it). Smaller detectors are under construction at Hannover (the German/British GEO project, 600 m arm length, http://www.geo600.uni-hannover.de), Tokyo (TAMA 300 m arm length, http://tamago.mtk.ano.ac.jp) and Perth (80 m arm length, http://www.gravity.pd.uwa.edu.au). Figure 15 shows some photographs of the LIGO detector in Hanford: (*a*) an aerial view, (*b*) the vacuum pipe tunnel and (*c*) the main cornerstation. The long-baseline laser interferometer detectors are initially expected to achieve sensitivity as shown in figure 16.

Laser interferometers are complex instruments limited by a range of noise sources: internal thermal noise in the mirror test masses, seismic noise, radiation pressure noise, laser frequency noise, control system noise, residual gas refraction noise etc. All noise sources must be reduced as far as possible to allow the detectors to achieve high sensitivity. The first decade of the twenty-first century will see steady improvement of the detectors. Late in that decade it is likely that major improvements to the detectors will be possible using improved lasers, improved test masses and improved vibration isolation. Figure 16 shows the expected improvements.

Ultimately, both laser interferometers and resonant masses can be improved by using various quantum measurement techniques. Laser interferometers can in principle also be improved by use of cryogenic methods, and by increasing their arm length.

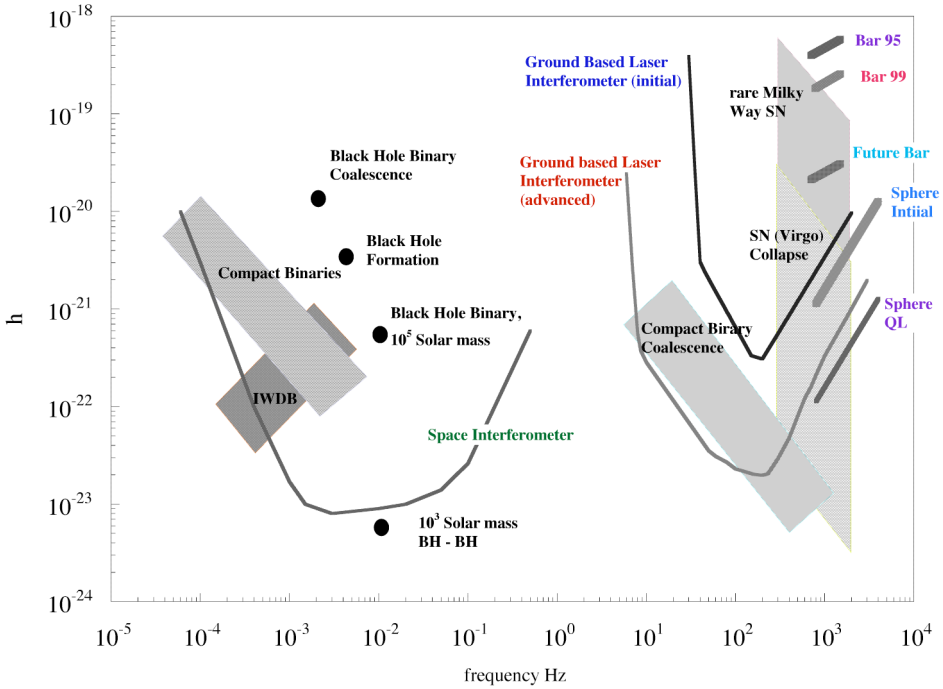

Figure 16. Rough comparison of various detector technologies and some sources. Note that the sensitivity depends on the type of signal searched for: the resonant-mass sensitivities quoted refer to burst sources (e.g. the narrow-band sensitivity of bars has already been demonstrated at 10^{-23}). At low frequencies interacting white dwarf binaries (IWDB) and neutron star binaries are known sources. At high frequency the only known source is neutron star binary coalescence: all the others have unknown signal strength.

All gravitational wave detectors provide data dominated by noise. All face difficult data processing challenges. In the following we shall briefly review some of the main issues in the context of the various classes of gravitational wave sources, before going on to examine resonant-mass and laser interferometer detectors in more detail.

3.5. Issues of data processing and signal detection

There are many important and still unresolved issues of data processing which it is necessary to solve to enable detection of signals to the levels anticipated from a simple analysis. These issues affect burst detection, stochastic background detection and narrow-band detection. Since the general analysis principles are independent of the type of detector used, we will discuss some of them in generality.

The raw data from a detector must first be filtered. In section 2.2 we discussed the use of *matched* filters or optimal filters to extract particular signals. An *optimal filter* is one which maximizes the signal-to-noise power ratio for a particular signal waveform. The term matched filter arose because in the special case where the noise is white, the optimal filter is one with an impulse response which *matches* the shape of the input signal. In these ideal circumstances the matched filter is simply a template of the waveform one desires to detect.

Think of the data from a detector over a particular period of time, due to some input signal. In a perfect noise-free detector it would create an output signal $s(t)$ which is uniquely

determined by incoming signal and the detector impulse response. After sampling, a real detector output consists of a two-dimensional array of output values o_i and time values t_i: $\{o_i, t_i\}$. But $o_i = s_i + n_i$ is a sum of the input signal s_i and the noise n_i. The template is a noise-free array representing $s(t)$, but it has an arbitrary phase, so can be represented $\{s_j, t_j\}$ where the difference between i and j represents a time difference. When the template is aligned with the signal $i = j$ and the sum of the products $o_i s_i (= s_i^2 + s_i n_i)$ over all values of i will be maximal. At times when s_i is zero there is no noise contribution. The template which accurately matches the ideal signal response of the detector is therefore the optimal filter function.

In practice one could apply a large calibration signal and measure the output signal to create such an optimal template.

Often it is more convenient to consider the problem in frequency space. In frequency space the phases of the noise frequency components are random and uncorrelated. If you multiply the Fourier transform of the output data $O(f)$ with the complex conjugate of the Fourier transform of the signal waveform $s^*(f)$, the signal component will be positive definite while the noise phases remain random. Summing over frequency space, the signal will add up but the noise frequency components will tend to cancel. Thus, in frequency space the matched filter transfer function is simply the complex conjugate of the Fourier transform of the input signal $s^*(f)$.

In almost all real situations the noise is not white. However, coloured noise can be whitened by passing it through a filter with a transfer function equal to $S_n^{-1/2}$ where S_n is the noise power spectral density of the noise. Thus, the optimal filter transfer function is simply $s^*(f)/S_n^{1/2}$. In the time domain the same correction for coloured noise is made using the noise autocorrelation function whose Fourier transform is S_n.

All optimal filters require a sum over frequency or time. If the signal is transient, then the sum will be zero after the signal has passed and the detector has stopped responding. For a resonant bar this will be several ring-down times of the bar (after which all memory of the signal is lost). In the same time *before* the signal arrives the bar loses memory of its instantaneous mechanical state. Thus it is only necessary to integrate over a modest time interval before and after the signal arrives. The Louisiana State University (LSU) group have implemented a time domain optimal filter by applying a large 'signal' pulse using a calibrator, and measuring the detector response, as well as the detector noise in the absence of a signal. Other bar groups have used frequency domain filters and obtained similar results [76].

There are many ways to implement optimal filters and the best choice often involves minimization of computation requirements for the particular search. For some systems optimal filters can be implemented in quasi-real time whereas for others the need for prior data requires the search to be conducted off-line.

A particular issue is that of noise stationarity. In practice, stationarity of the noise is not a good approximation. This means that the noise spectrum at the output varies with time, due, for example, to environmental effects such as variable microseismic noise from changes in the ocean wave conditions [77]. To overcome slow changes in the detector noise distribution it is possible to always use recent noise data for the creation of the optimum filter. Several groups use noise from the previous few hours to continually adapt the filter [78].

Another problem relates to the fact that in gravitational wave detectors it is impossible to turn off the signal, and possible signal-like noise events (such as cosmic ray events). Thus, in principle it is impossible to measure the noise spectrum in the absence of signal. In practice today this is not a critical issue (signals are rare and very small), but for future detectors it may be important to ensure that the filter does not suppress signal by confusing it with noise. Heng has shown [79] that periodic transient bursts are indeed suppressed by an optimum filter if the

bursts are present during the measurement of the noise distribution.

For CW signals, a Fourier transform of the entire data set represents an optimal filter. By this method the signal appears as a narrow spectral line. If the Earth's orbital and rotational Doppler corrections are included this method can be used to search for unknown CW signals (such as those due to isolated spinning neutron stars) in a particular direction (because the Doppler correction is direction dependent, see figure 30).

Traditionally the lock-in amplifier or phase-sensitive detector (PSD) has been used to create a matched filter operating in the time domain for CW or near-CW signals. For modern systems this type of filter can be implemented by software (hence not in real time) which allows it to be used for multiple searches through the same piece of data. It also allows CW searches with arbitrarily long integration times. (The traditional analogue lock-in amplifier is limited by the charge storage time of a capacitor.)

The lock-in amplifier form of the matched filter multiplies the data by +1 during the positive going signal cycle, and -1 during negative parts of the cycle. All results are summed. The sum represents the phase coherent integral of the absolute value of the signal over the observation time: hence the alternative name for this method: coherent integration. The noise components average towards zero, and a small signal component previously buried in the noise will emerge.

Assuming that the phase of the incoming signal is unknown, it is necessary to repeat the matched filter at 90° phase shift to determine the magnitude of the orthogonal components of the signal. (For example, if the signal was a pure sine function, the matched filter would give a zero output if the +1 and -1 multipliers were defined by a cosine function.) Clearly, if there were slowly varying phase errors due to errors in the timing of data acquisition, errors in direction for Doppler corrections, or errors in the prediction of the waveform, the accumulated result from a matched filter could average to zero.

For a CW source of fixed but unknown frequency it is usually simpler to replace matched filtering with the fast Fourier transform. However, if the frequency is modulated in a known pattern (such as occurs when you search for a signal from a known binary pulsar) [80] the coherent integration is computationally simpler.

Attempts at gravitational wave burst detection have normally followed techniques first introduced by Weber. By this method the data is first filtered, as discussed above, and then thresholded to obtain a list of candidate events. Some events will be due to spurious effects (see below). These can be vetoed if the appropriate monitor channels are used. Then the event lists for widely spaced pairs of detectors are correlated to search for coincidences. If the time axes for the event lists are randomly displaced one expects all correlation due to possible gravitational wave bursts to be absent. Thus it is possible to compare true-time coincidences with time-shifted coincidences to determine whether there is an excess of 'zero time delay coincidences'. This method is powerful since it allows the probability of accidental coincidence to be experimentally determined by simply running the random time shift analysis a sufficient number of times to obtain an accurate estimation of the probability of the observed peak. However, it is only relevant when the number of accidental coincidences is large.

Consider, for example, a six-month coincidence run which might yield 5000 'candidate events' in each detector, most of which are assumed to be noise or interference. The coincidence analysis might yield 30 true-time coincidences. For such analysis with existing resonant bars the coincidence window is usually more than 0.1 s, so that propagation delays across the Earth ($\sim$40 ms) can be neglected. Then 1000 random time delays are applied to the data of one detector and of these 10 might show 30 or more coincidences. If this was the case, then the zero time delay peak would have a probability that it was accidental of 10/1000 or 1%. This probability could be resolved with more accuracy if more random time delays were used. In

this type of experiment the time delays which are chosen must either be small compared with total duration of the experiment, or they should be modulo the experiment duration so that coincidences are not lost at the ends of the record.

A serious pitfall can occur in this type of analysis if the threshold for candidate event selection, or any other vetoing scheme, is variable during the coincidence experiment. To have such a variable accessible to the persons analysing the data can allow conscious or unconscious selection which can completely invalidate the statistical significance analysis. It can be very difficult to estimate the true significance after such selection has taken place. Since the days of Weber, researchers have been in general very careful to pre-set all thresholds to try to avoid such pitfalls.

For the existing array of five resonant-mass detectors it has been suggested that the entire body of data from all detectors should be used rather than candidate events. As discussed in the next section, the accidental coincidence rate is extremely low for five detectors. The thresholding method means that all phase information is lost. However, it need not be lost if the data from separate detectors are recombined along the lines used by VLBI radioastronomy. If this was done the detectors could represent a single telescope with angular resolution for incoming bursts set by the ratio of the time resolution (in principle $\sim$100 μs) and the near-Earth-diameter baseline (40 ms). However, the noise increases exponentially as one digs to lower and lower energy so the overall amplitude sensitivity of the array would be limited to $\sim$3 times.

Most data from terrestrial gravitational wave detectors can be idealized as the sum of a pair of thermal distributions. The first is the intrinsic Boltzmann distribution of the detector noise that one would measure using a spectrum analyser. This is usually due to some well understood noise sources such as thermal noise, electronics noise or shot noise. The second distribution is described as excess noise. Excess noise arises from rare and poorly understood sources. In the detector NIOBE at the University of Western Australia (UWA) some of the excess noise was correlated with electromagnetic pulses and seismic noise [81]. However, the majority was not identified, but might be due to strain relief events. Surprisingly, the excess noise distribution is rather similar for widely differing types of resonant-mass gravity wave detector. Figure 17 shows the idealized form of these distributions. Both may be expressed as

$$N = N_0 \mathrm{e}^{-E_e/kT}. \tag{3.1}$$

For a typical resonant-bar detector the intrinsic distribution parameters would be: $N_0 \sim 10^5$ per day, and $E_e \sim$ few millikelvin (Kelvin is simply a convenient energy scale). The excess distribution typically would have $N_0 \sim 10$ per day, and $E_e \sim$ few 100 mK: that is, the excess noise distribution has an event rate 10^4 times lower than the thermal distribution, and an effective energy 100 times larger. The presence of these two distributions allow improved data analysis, as discussed in section 4.8.

Periodic signals can be detected by coherent integration or Fourier transform methods. Because, as always, signals are near to the limit of detection sensitivity, long integration is needed. However, in long integrations signals will be smeared out by the Earth Doppler motion unless the source direction is known. Equally, if the source is a member of a binary system such as a binary millisecond pulsar it is necessary to know the ephemeris of the system itself as well as the precise source direction to prevent Doppler smearing of the signal. If coherent integration can be achieved, then the signal-to-noise ratio improves as $\tau^{1/2}$, which can allow very deep searches over a 1–3 year period.

The nearest millisecond pulsar PSR 0437-4715 is a typical such potential source. In this case the pulsar source is a binary system, which is extremely well defined by pulsar timing [82]. The observed radio pulse timing gives very accurate information which can be used to gate the

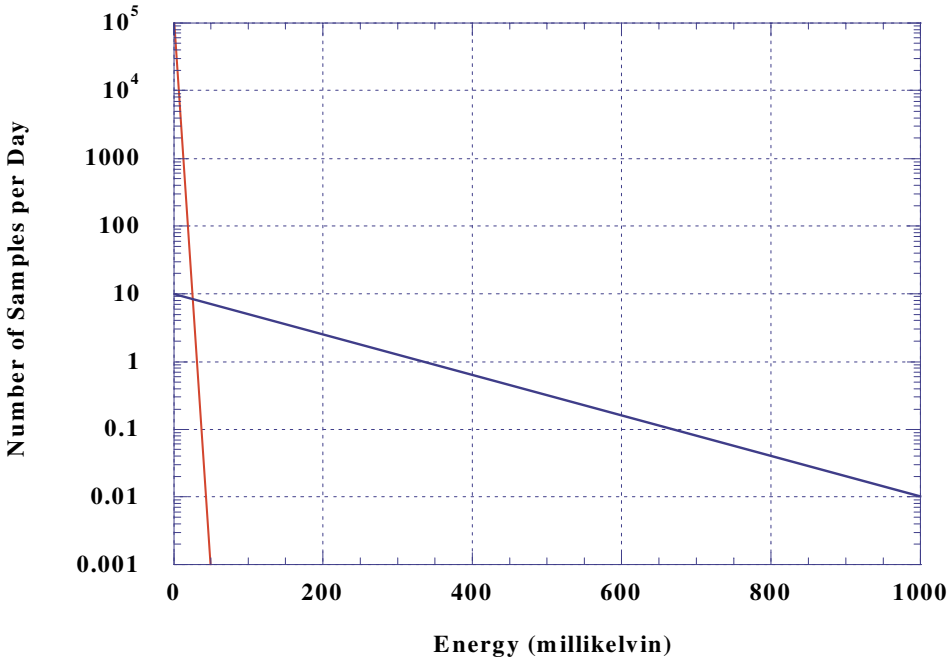

Figure 17. Detector noise is often characterized by a pair of Boltzmann distributions. The steep curve is the typical antenna thermal noise distribution for burst detection in a resonant bar. The flatter curve is the excess noise distribution due to rare disturbances.

phase-coherent integration of the detector output [80]. Such methods were pioneered by the Tokyo group [83] led by Hirakawa searching for gravitational radiation from the Crab pulsar.

It is likely that many such narrow-band sources will not be detected in advance by radio astronomy. Pulsar beaming ensures that the majority of pulsars are not visible in radio, and normal pulsars older than 10^8 years appear to cease to emit radio beams. There could easily be 1000 rotating neutron stars within the range of the nearest observed pulsars ($\sim$100 pc) meaning that a few old neutron stars could exist within 10 pc of the solar system.

Unfortunately, our ability to search for such sources is very poor because of the difficulty of searching all directions in the sky. The most obvious search strategy involves applying a separate ephemeris correction for each of typically 10^{10} source directions, and re-integrating the data 10^{10} times. This already is a daunting computational exercise, but it becomes 10^{10} times harder if the search space has to involve all possible binary orbits of the pulsar. Many investigators are searching for efficient algorithms to solve this problem, based on alternative filtering techniques or hierarchical searches [84].

As discuss in sections 2.2 and 2.8, stochastic signals can be detected by cross-correlation of nearby gravitational wave detectors. For optimum sensitivity the detectors must be located within about one reduced wavelength ($\lambda/2$) of each other. If the spacing requirement is satisfied, the signal-to-noise ratio increases as the $\frac{1}{4}$-power of the number of cycles observed [85]:

$$\frac{S}{N} = \left(\frac{S_{gw}^2}{S_1 S_2} B\tau\right)^{1/4}. \tag{3.2}$$

Here S_{gw} is the gravitational wave background power spectral density, S_1 and S_2 are the spectral

noise density of two detectors, B and τ are the bandwidth and duration of the observation respectively. Thus, a stochastic signal of characteristic frequency $\sim$100 Hz can be cross-correlated to gain a factor of $10^{2.5}$ in signal-to-noise ratio (compared with the observation of a single cycle) after 10^8 s integration. Schutz [85] has shown that this method can be particularly effectively applied to signals in detectors of quite different types: specifically resonant-mass detectors and laser interferometers, which conveniently are planned to be located in sufficiently close proximity to each other to satisfy the above spacing requirement.

The simplest cross-correlation experiment merely gives an output consisting of a single number (and a measure of its statistical significance). This can be quite misleading since there are many ways that cross-correlation can give a false positive result. The major difficulty in cross-correlation signal processing is to ensure that no correlated technical noise components exist in the signals. Remembering that the signal detected is generally going to be at least 100 times lower than the spectral noise floor accessible using normal fast Fourier transform diagnostic instrumentation, correlated features can exist which could never be detected in short-term monitoring. The correlated features could be weak spectral lines such as those created by electrical power harmonics, (which are phase coherent over the electrical grid) or occasional transients such as those due to lightning flashes. To prove that a positive cross-correlation signal was associated with gravitational waves it would be necessary to show that the correlation was preserved across the accessible frequency band, and that it was not due to intermittent transients due to electrical interference. The individual output spectra of the detectors would need to be resolved for weak spectral features to the same depth as the correlation detection threshold. Much effort at developing algorithms and solving some of these practical problems is underway [53, 86].

Giazotto [87] has shown that the stochastic background signal from the combined old radio pulsars in our Galaxy should be detectable in a single detector, due to the fact that they are non-isotropically distributed relative to the solar system. The central concentration of pulsars means that there should be a strong sideband modulation of the stochastic background intensity as the detector sweeps the sky during Earth rotation. This signal should appear in the technically very demanding 1–10 Hz frequency band.

The next two sections present resonant-mass detectors (section 4), and then laser interferometer detectors (section 5), with emphasis on techniques and the solution to various technological challenges.

4. Resonant-mass detectors

4.1. Introduction

Resonant-mass detectors are designed to measure acoustic signals induced in a large mass due to its coupling to a gravitational wave. Resonant detectors were first developed by Weber during the 1960s [4]. They consisted of large vibration-isolated aluminium cylinders instrumented with piezoelectric crystals glued on the surface near to the centre. A low-noise amplifier and lock-in amplifier allowed detection of the energy of the fundamental longitudinal resonance of the bar. A gravitational wave applies a time-varying quadrupole deformation and does mechanical work on the bar. The absorption cross section of the bar to gravitational waves depends on its mass and sound velocity. The cross section is highest at the fundamental resonant frequency. The latter is linked to its length and sound velocity, since its length must be half an acoustic wavelength at the fundamental longitudinal resonance. Weber chose aluminium because of its high sound velocity and availability in large pieces, and because it has quite low acoustic losses. Following Weber, many new resonant-mass detectors using similar techniques, but with

variations and improvements, were developed in the early 1970s. Following null results these were abandoned, but advanced resonant-mass detectors using cryogenics and superconductivity continued to be developed. Fairbank *et al* [88] and Hamilton *et al* [89] first proposed such cryogenic detectors, and proposed cooling to millikelvin temperatures to minimize thermal noise. Today two detectors in Italy are in operation at temperatures below 100 mK.

In all resonant-mass detectors the large amplitude of thermal vibration considerably exceeds the gravitational wave amplitude expected from astrophysical sources. Without methods to suppress this noise the principle of detection by resonant masses would be impossible. Weber's key contribution was the realization that in a high-Q antenna—one with a low acoustic loss—the effective noise energy is reduced by a factor $\sim\tau_i/\tau_a$, where τ_i is the effective measurement integration time, and τ_a is the antenna ring-down time. The advantage of using a low acoustic loss antenna follows directly from the fluctuation–dissipation theorem [90]: the greater the dissipation the greater the fluctuations or noise level imposed by the thermal reservoir. A high-Q antenna approaches an ideal harmonic oscillator, whose motion is exactly predictable at a time in the future from the observed amplitude, frequency and phase at an earlier time. High levels of predictability means that very small deviations from sinusoidal behaviour can be resolved given a sufficiently sensitive transducer for monitoring its motion.

4.2. Intrinsic noise in resonant-mass antennas

To understand the operation of a resonant-mass gravitational wave detector it is convenient to start with an old-fashioned approach first introduced by Gibbons and Hawking [91]. This approach is intuitively obvious but is not consistent with the optimal filter theory discussed in section 3. The instantaneous state of the antenna can be described by the pair of symmetrical harmonic oscillator coordinates X_1 and X_2 given by

$$\begin{aligned} X_1 &= A\cos\phi \\ X_2 &= A\sin\phi, \end{aligned} \tag{4.1}$$

where A is the antenna amplitude and ϕ is the phase. Experimentally, X_1 and X_2 can be easily measured using two lock-in amplifiers or PSDs in a configuration shown schematically in figure 18. They may be analogue or digital or software devices. The state of the antenna can be represented by a point P_1 in the (X_1, X_2) plane. The amplitude $A = |P| = (X_1^2 + X_2^2)^{1/2}$ and phase $\phi = \tan^{-1} X_2/X_1$. This is illustrated in figure 19. A gravitational wave causes the antenna to move from P_1 to P_2. The direction of this motion depends on the relative phase of the gravitational wave and the resonant mass. To extract a signal the measuring system should monitor $\Delta|P_1 - P_2| = (\Delta X_1^2 - \Delta X_2^2)^{1/2}$. The quantity Δ^2 is described as the energy innovation and its magnitude, properly calibrated and expressed in the units of Kelvin (1.38×10^{-23} J) describes the effective temperature of the antenna.

In a noiseless antenna the motions of the vector P would only be due to gravitational waves, but in practice P is driven by thermal fluctuations in the bar. Thermal fluctuations cause the state vector P to execute a random walk in the X_1X_2 plane. A high-Q mode is weakly coupled to the thermal reservoir which is made up of all the higher modes of the system. The antenna loses energy slowly into the reservoir, and equally it is only weakly excited by the reservoir. The relaxation time $\tau_a = 2Q/\omega_a$ thus characterizes both the rate of decay after a high-energy excitation and the rate of amplitude change when the mode is in thermal equilibrium with the reservoir.

Clearly, if τ_a is large and the rate of fluctuation is low, the antenna becomes more deterministic on time scales that are short compared with τ_a. The mean energy is still kT,

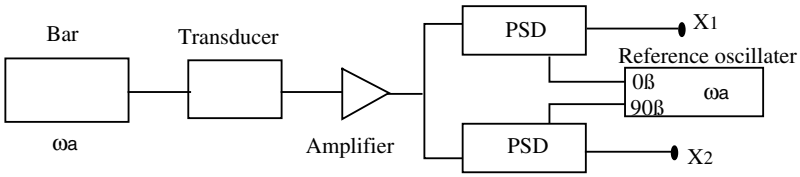

Figure 18. Antenna readout systems for obtaining harmonic oscillator coordinates X_1 and X_2. The down-conversion with the PSD was conventionally done with analogue electronics but today can be achieved in software using fast digital sampling [78].

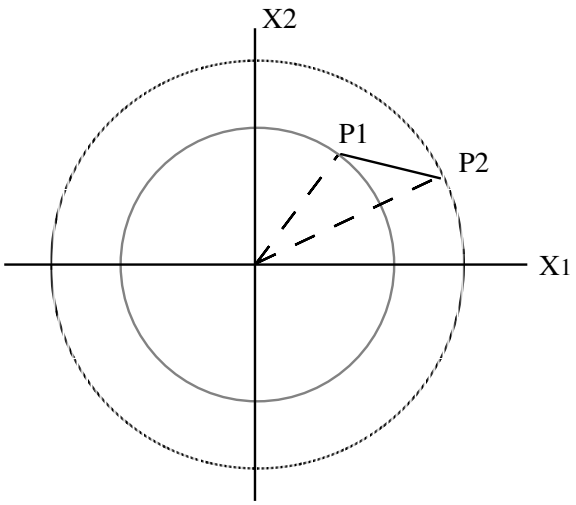

Figure 19. X_1–X_2 representation of the state of the antenna.

but the expected change in energy in a sampling time τ_i is $kT(\tau_i/\tau_a)$. The temperature $T(\tau_i/\tau_a)$ is the effective temperature or noise temperature of the resonator, and quite clearly can be made less than the actual temperature. Indeed, even when transducer readout noise is included, a noise temperature of less than 2×10^{-4} of the thermodynamic temperature has been demonstrated in the detector NIOBE. To use temperature to describe the antenna noise implies that the distribution of Δ^2 has a Boltzmann distribution. This is an excellent approximation (see figures 17 and 28). The slope of the distribution as well as its mean value gives the antenna noise temperature.

The above analysis describes a predictive filter for the detection of short bursts. In this case our prediction is that the amplitude and phase of the detector will remain unchanged over the integration time. Today all operating detectors use optimum filters for the detection of short bursts. The optimum filter improves on the simple predictor discussed above because it implicitly takes into account the dynamics of the system for times of the order of the antenna ring-down time over which the motion is correlated. They are implemented as discussed in section 3 and enable the antenna noise temperature to be improved by a small factor. The most popular optimum filter or matched filter is the Weiner–Kolmogoroff filter which is designed to detect short delta function bursts [92]. Today, such filters are routinely used since they were shown by Pizzella *et al* [93] to give substantially improved performance.

Every antenna must use a sensitive transducer to read out the motion. The transducer, like all electronic devices, has a residual broadband noise floor. This noise floor is equivalent to the Johnson or Nyquist noise of a resistor, given by $V_n^2 = 4kTRB$, where R is the effective resistance of the transducer and B is the measurement bandwidth. However, the bandwidth is roughly the reciprocal of the measurement integration time τ_i. Thus it follows that the noise power is $4kT/\tau_i$. Comparing this with the Brownian motion noise, we see that one noise source varies as τ_i while the other varies as $1/\tau_i$. Thus there is clearly an optimum bandwidth set by the value of τ_i that minimizes the total noise.

Gibbons and Hawking [91] introduced a parameter β to characterize the coupling between the bar and the transducer. They defined β as the proportion of the elastic energy of the detector that can be extracted electrically through the transducer in one cycle. A bar–transducer system with low β (weak coupling) requires more time for the signal energy to appear in the transducer. The longer the energy transfer takes, the more time there is for fluctuations in the antenna to dominate the noise. This point can be clarified by two alternative viewpoints. One is a thermodynamical model. The antenna is considered as a thermal bath at temperature $T_{\rm eff} = T_a\tau_i/\tau_a$, coupled to a transducer with noise temperature T_t which itself is coupled to an amplifier of noise temperature T_n.

A gravitational wave causes slight 'heating' of the fundamental mode and energy flows through the coupling β. As long as $\beta > 0$ the transducer will eventually come into equilibrium with the bar, but for a rapid response β has to be large. The thermodynamic approach emphasizes that the coupling is not unidirectional: thermal fluctuations in the amplifier or the transducer act back on the antenna producing *back-reaction noise*. Indeed, it is clear that the transducer is a source of thermal fluctuations comparable to those originating within the bar. Voltage noise in the transducer will convert into force noise acting on the bar. Like the forces which act on the bar from the thermal reservoir, the back reaction will produce an additional noise contribution which will diminish as τ_i reduces to zero, as does the Brownian noise.

The second viewpoint is that the antenna–transducer system is effectively a transmission line designed to couple energy into the transducer. One can think in terms of phonons in the bar which may be absorbed by the transducer, with the emission of a photon into the amplifier, or they may be reflected back into the bar. Then β determines the *impedance match* between the output impedance of the bar, $Z_{\rm out}$, and the transducer's mechanical input impedance Z_{ll}. The ratio $Z_{ll}/Z_{\rm out}$ is simply the coupling coefficient β. See below for more discussion of this point.

Once we begin to think in terms of quanta we are led to ask: what happens if the induced strain in the antenna is equivalent to less than one quantum $h\omega_a$? The profound significance of the quantum mechanical limit to macroscopic measurements was realized independently by several groups, particularly by Braginsky [94] and Giffard [95]. Giffard used the much earlier result of Heffner [96] who showed that, by the uncertainty principle, a linear amplifier has a fundamental limit to its sensitivity, given approximately by $\hbar\omega_a$. Similarly, Giffard showed that a transducer used with a linear amplifier (an amplifier which preserves phase and changes the amplitude by a multiplicative factor) has a maximum sensitivity corresponding to a gravitational wave which produces an equivalent of two quanta in the bar. The term *equivalent* is used because the actual energy absorbed by the antenna depends on its instantaneous amplitude. For linear systems the signal-to-noise ratio is independent of the amplitude, and corresponds exactly to the signal produced in an ideal stationary antenna at absolute zero. Giffard's result meant that the maximum achievable sensitivity of an antenna would be limited to about the single phonon level corresponding to a strain sensitivity $\sim 10^{-21}$. This is described as the standard quantum limit.

Meanwhile, at least as early as 1974, Braginsky and Vorontsov proposed that in principle it might be possible to devise *quantum non-demolition devices* which could read out the state of a system without disturbing it. Braginsky *et al* [97], Caves *et al* [98], Unruh [99] and others went on to identify methods whereby gravitational waves of amplitude less than that required to induce one quantum can in principle be detected using *quantum non-demolition* or back-action-evading techniques. The possibility of mechanical measurements down to and below the quantum limit in sapphire bars has been investigated in detail by Tobar *et al* [100]. The most promising technique is through the use of amplitude-modulated parametric transducers. This represents a small elaboration of parametric transducers of the type we will discuss in section 4.4. The pump signal is amplitude modulated at the signal frequency to create an intrinsically phase-sensitive measuring system. However, classical noise sources need to be beaten down close to the quantum limit before such techniques can successfully pass the quantum limit on real antennas.

4.3. The signal-to-noise ratio for burst detection

Resonant-mass detectors may be used to detect all of the signal classes discussed in section 4.2. However, most effort has concentrated on the detection of bursts. In general, when a gravitational wave in the right frequency range arrives, it excites all normal modes of the bar that have a high quadrupole moment. A transducer attached to the bar will pick up the signal, which must be discerned in the presence of transducer noise and a large Brownian motion background, as discussed in the previous section.

The efficiency of the detector is determined by the fraction of the wave energy absorbed and converted into acoustic energy inside the bar. Clearly, it is important that the bar absorb as much as possible of the energy of the passing gravitational wave. This can be quantified in terms of the antenna cross section as discussed below. Denoting the incident spectral energy density of gravitational waves as $w(f)$, the energy deposited in the bar is given by

$$\varepsilon_g = \sigma w(f). \tag{4.2}$$

The term σ in the above equation is the so-called cross section of a bar, which is the ratio of the absorbed energy to the incoming energy, and thus a measure of the sensitivity of the bar. The cross section is actually a function of frequency $\sigma(f)$ because the detector will absorb energy more readily around the resonant frequency f_o of the antenna. The total energy deposited in the bar is then

$$E = \int \sigma(f) w(f)\, \mathrm{d}f. \tag{4.3}$$

Since for a high-Q system, $\sigma(f)$ is sharply peaked around the resonant frequency f_0, only a narrow portion of the gravitational wave signal around the resonant frequency of the bar can be picked up by the detector. In this case we may write

$$\sigma(f) w(f)\, \mathrm{d}f = w(f_0) \int \sigma(f)\, \mathrm{d}f. \tag{4.4}$$

The cross section, first elaborated by Weber, can be expressed in several forms [7]. The cross section of the bar, integrated over the frequency band, can be expressed as [101]

$$\int \sigma(f)\, \mathrm{d}f = \frac{8GM}{\pi c} \left(\frac{v_s}{c}\right)^2 \ \mathrm{m^2\ Hz}, \tag{4.5}$$

where v_s is the sound velocity in the bar, and M is the mass of the bar. Clearly, to obtain high sensitivity it is desirable to build detectors as massive as possible and from a material having a sound velocity as high as possible. Usually, the size of the bar is chosen such that

the fundamental mode is at about 1 kHz—about the expected frequency for the collapse of a massive stellar core to a black hole. Aluminium has been used for most resonant bars. Niobium is used for the bar detector at the University of Western Australia. Other materials could give substantial advantages, as discussed in section 4.5 below.

A gravitational wave carries an energy flux S(J m^{-2} s^{-1}) given by

$$S = \frac{c^3}{16\pi G}\langle h_+^2 + h_x^2\rangle, \tag{4.6}$$

where h_+ and $h_\times$ denote the dimensionless strain amplitudes of the two possible polarizations of the wave. Since the shape of expected gravitational wave pulses from gravitational collapse events is not accurately known, we cannot accurately determine the expected excitation of an antenna even knowing the total pulse energy. We need to know both the spectral distribution of the pulse energy, and the relationship between h and its time derivative. The details of the expected pulses depend not only on the dynamics of the gravitational collapse, but also on the mass of the collapsing object, both of which are uncertain.

If we assume only knowledge of the pulse duration τ_g (expected to be $\sim 10^{-3}$ s), and that it is predominantly a single cycle, it is sufficient to assume that $\mathrm{d}h/\mathrm{d}t \sim 2h/\tau_g$. Then equation (4.6) can be rewritten

$$S = \frac{c^3}{16\pi G}\frac{4h^2}{\tau_g^2}. \tag{4.7}$$

The total pulse energy E is then given by $S \cdot \tau_g$:

$$E = \frac{c^3}{16\pi G}\frac{4h^2}{t_g^2}. \tag{4.8}$$

If we assume that the spectral distribution of the pulse energy $F(\omega)$ is uniform over a bandwidth $\Delta\omega \sim 1/\tau_g$, it follows that

$$F(\omega) \sim E/\Delta\omega, = E\tau_g \sim c^3 h/4\pi G \text{ J m}^{-2} \text{ Hz}^{-1}. \tag{4.9}$$

Numerically $F(\omega) \sim 20 \times 10^{34}\, h^2$.

The assumption used in obtaining the result must be emphasized: the result is simply an order-of-magnitude estimate of the expected signal spectral densities. Moreover, variations in the pulse durations could make any chosen antenna frequency only suitable for a small proportion of actual events.

The energy deposited in an initially stationary antenna of mass M by a signal pulse $F(\omega)$ follows directly from equation (4.5) combined with geometrical terms:

$$U_s \sim F(\omega)\sin^2\theta\cos^2 2\phi\frac{8}{\pi}\frac{G}{c}\left(\frac{v_s}{c}\right)^2 M \tag{4.10}$$

where θ and ϕ are coordinates describing the orientation of the bar relative to the incoming wave (as given in figure 20).

For a short burst of gravitational waves the bandwidth of the pulse is roughly the inverse of the pulse duration which is roughly equal to the peak frequency. Under these circumstances the strain amplitude $\delta 1/1$ induced in the bar is roughly equal to the incoming wave amplitude h; there is no resonant excitation.

The incoming gravitational wave will only be detectable if the signal U_s is greater than the noise in the antenna U_n. From an engineering point of view it is useful to characterize the noise U_n; we generalize the transducer to a two-port device described by a 2×2 impedance matrix Z_{ij}. The transducer accepts force and velocity inputs F and v, giving current and voltage outputs I and V:

$$\begin{pmatrix} F \\ V \end{pmatrix} = \begin{pmatrix} Z_{11} & Z_{12} \\ Z_{21} & Z_{22} \end{pmatrix}\begin{pmatrix} v \\ l \end{pmatrix}. \tag{4.11}$$

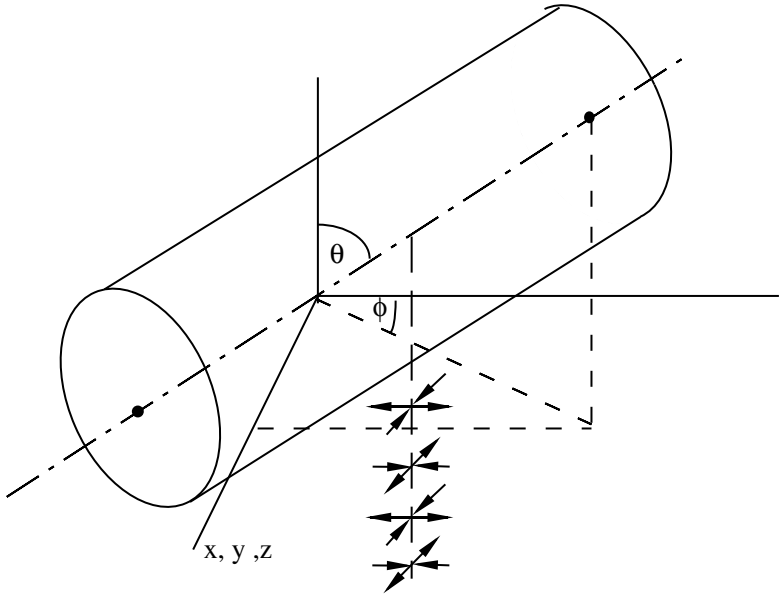

Figure 20. Coordinate system for resonant antenna.

The transducer has input impedance Z_{ll}, measured in kg s^{-1}, and output impedance Z_{22}, measured in ohms. The forward transductance Z_{21}, measured in V m^{-1} s, determines the transducer sensitivity whereas the reverse transductance Z_{12}, measured in kg A^{-1}, determines the back-acting force on the antenna due to currents in the output circuit: see [100, 102–104] for more details. Quantum mechanics tells us that it is impossible to make $Z_{12} = 0$: it is impossible to create a perfect one-way valve.

All the noise sources in the transducer and amplifier can be expressed as equivalent spectral densities of current and voltage noise at the input of the amplifier, denoted $S_i(\omega)$ and $S_e(\omega)$, respectively, as illustrated in figure 21. The current noise S_i is the source of back-action noise in the antenna, whereas S_e describes the series noise contribution. In terms of these quantities the total system noise is given by

$$U_n = 2kT_a\frac{\tau_i}{\tau_a} + \frac{|Z_{12}|^2}{2M}S_i(\omega)\tau_i + \frac{2M}{|Z_{21}|^2}\frac{S_e(\omega)}{\tau_i}. \tag{4.12}$$

The first term in equation (4.12) is the Brownian motion or thermal noise in the antenna discussed above. The second term describes the energy fluctuations arising from the current noise acting back through the reverse transductance, and giving the back-action noise, also proportional to integration time. The third term is the series electronics noise, which for given S_e is reduced as Z_{21} increases. As we saw above this term is proportional to the bandwidth τ_I^{-1}. Only the first term in equation (4.12) can ever be reduced below the quantum limit.

The problem of detecting gravitational waves with resonant-bar antennas to a large extent consists of minimizing equation (4.12). The technical means of achieving this requires some or all of the following:

(a) Reduce the antenna temperature T_a.
(b) Use a transducer with high Z_{21} and low Z_{12}.
(c) Use amplifiers with S_e and S_i as low as possible.

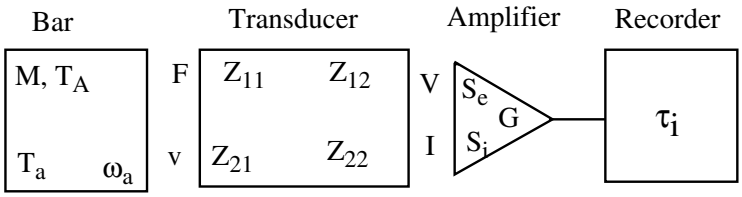

Figure 21. The various quantities used to characterize a gravitational wave antenna system.

(d) Reduce the acoustic loss in the antenna as well as the acoustic and electrical losses in the transducer to obtain high-Q or large relaxation time.
(e) Obtain a reasonable impedance match between antenna and transducer to enable τ_i to be small.

The last requirement can only be achieved by good impedance matching between the mechanical input impedance of the transducer and the mechanical output impedance of the antenna, which we shall discuss further below.

It is convenient to scale the noise in the system relative to the *standard quantum limit* of one equivalent quantum induced in the bar. To do this we rewrite the noise equation (4.12) in terms of *noise number A* (a quantity first used by Weber to characterize noise in masers):

$$A = U_n/\hbar\omega_a = A_T + A_B + A_S. \tag{4.13}$$

Here A_T, A_B and A_S are the equivalent numbers of noise quanta due to thermal noise, back-reaction noise and series noise in the measurement system. The experimentalists need to achieve a total system noise number A approaching unity. For a 1 kHz resonant bar this corresponds to a noise temperature of $\sim$0.1 μK. To achieve this it is necessary not only to have a low-noise transducer, but also to use a low-acoustic-loss antenna material, and to suspend and isolate the antenna so as not to increase the acoustic loss, nor to couple in excess noise from the environment. Because the noise number contributions are additive there is no particular advantage in reducing one of them far below the others.

It is useful to express the thermal and transducer noise contributions directly in terms of the gravitational wave strain equivalent noise. The *Brownian motion noise* h_B is given by [105]

$$h_B \sim \left(\frac{k_B T \tau_i}{M\omega_a l^2 Q}\right)^{1/2}. \tag{4.14}$$

For a bar detector, $\omega_a l = \pi v_s$, so the Brownian noise is given by

$$h_B \sim \left(\frac{k_B T \tau_i \omega_a}{\pi^2 M v_s^2 Q}\right)^{1/2}. \tag{4.15}$$

Expressing the above equation numerically, we have

$$h_B = 10^{-21}\left[\left(\frac{f_0}{1\ \text{kHz}}\right)\left(\frac{10^{10}\ \text{J}}{M v_s^2}\right)\left(\frac{10^9}{Q}\right)\left(\frac{T}{0.1\ \text{K}}\right)\left(\frac{\tau_i}{10^{-2}\ \text{s}}\right)\right]^{1/2}. \tag{4.16}$$

This means that a resonant-mass detector with the hypothetical parameters implied in the above equation will have a Brownian motion noise strain of about 10^{-21}. However, some of the parameters given above are difficult to achieve in practice. For example, the energy term is satisfied by about 10 tonnes of sapphire or 100 tonnes of bronze or niobium. In the case of the UWA niobium bar with mass of 1.5×10^3 kg, resonant frequency of 700 Hz, sound velocity of 3.4×10^3 m s^{-1}, temperature of 4 K, Q-factor of 3×10^7 and measurement integration time 1 s, the Brownian noise strain amplitude is 2.2×10^{-19}. It can be seen that the bar must

have a very high acoustic quality factor or much shorter integration time to reduce the effect of the thermal noise. With today's multimode impedance matching techniques, τ_i can indeed be reduced to 10^{-2} s.

The sensor noise lower limit (series noise and back-reaction noise $A_B + A_S$) is set by the standard quantum limit [105]

$$h_{\mathrm{SQL}} \sim \left(\frac{2\hbar\omega_a}{\pi^2 M v_s^2}\right)^{1/2} \sim 1.1 \times 10^{-21} \left(\frac{f_m}{1\ \mathrm{kHz}}\right)^{1/2} \left(\frac{10^3\ \mathrm{kg}}{M}\right)^{1/2} \left(\frac{10^4\ \mathrm{m\ s^{-1}}}{v_s^2}\right). \tag{4.17}$$

This sets a strain amplitude limit $\sim 10^{-22}$ for a 100 tonne resonant-mass detector such as the proposed spherical detectors.

4.4. Transducers

Transducers for resonant-mass gravitational wave antennas fall into two categories: *passive* transducers and parametric transducers. Passive transducers have no external power source, and their power gain is less than unity. They must always be used with a high-gain, low-noise amplifier at the frequency of the antenna. Parametric transducers, on the other hand, have an external power source (a pump oscillator at frequency ω_p) which is modulated by the antenna motion. They have intrinsic power gain associated with the transfer from the antenna frequency ω_a to the higher frequency ω_p. A laser interferometer is a parametric transducer operating at an optical pump frequency. Parametric transducers for resonant-mass readouts may be optical, microwave or radiofrequency devices.

Most parametric transducers use a high-frequency resonator combined with a low-noise high-frequency amplifier. Passive transducers use an inductive or capacitive readout, coupled to a SQUID amplifier. Figure 22 illustrates their basic structure. The passive transducer illustrated uses a superconducting inductor whose inductance (if constructed in a planar fashion) is proportional to the gap spacing between the coil and the superconducting ground plane on the antenna. Relative motion modulates persistent current trapped in the inductor (since the magnetic flux LI must be conserved). The changing current is detected by a SQUID magnetometer. The parametric transducer illustrated uses a capacitor in a resonant circuit. The capacitance is modulated by the gap spacing between the capacitor and the antenna. The change in capacitance due to motion modulates the resonant frequency of the circuit, creating modulation sidebands on the output signal. Both types of transducer may use capacitive or inductive sensing.

Fundamentally, there is little difference between passive and active transducers. Active transducers use a transduction process that is combined with power amplification but additional amplification of the high-frequency signal is usually necessary. Passive transducers have a complete separation between the transduction process and the amplification process. However, the amplifier itself (such as a SQUID) makes intrinsic use of a parametric up-conversion process. Thus the difference between passive and active transducers is simply in the choice of whether the parametric up-conversion occurs during or after transduction. In the case of an optical pump frequency, amplification is unnecessary: the entire power gain is realized through the up-conversion of the signal frequency to the optical frequency.

One important difference between passive and parametric transducers is in the transducer impedance mismatch ratio or coupling factor β. For the parametric transducer

$$\beta_{\mathrm{para}} \frac{1}{2} \frac{C V_p^2 Q_e}{m\omega_a^2 x^2}. \tag{4.18}$$

In the limit $Q_e > \omega_p/\omega_a$, the electrical Q-factor of the transducer resonator Q_e is replaced by the frequency ratio ω_p/ω_a.

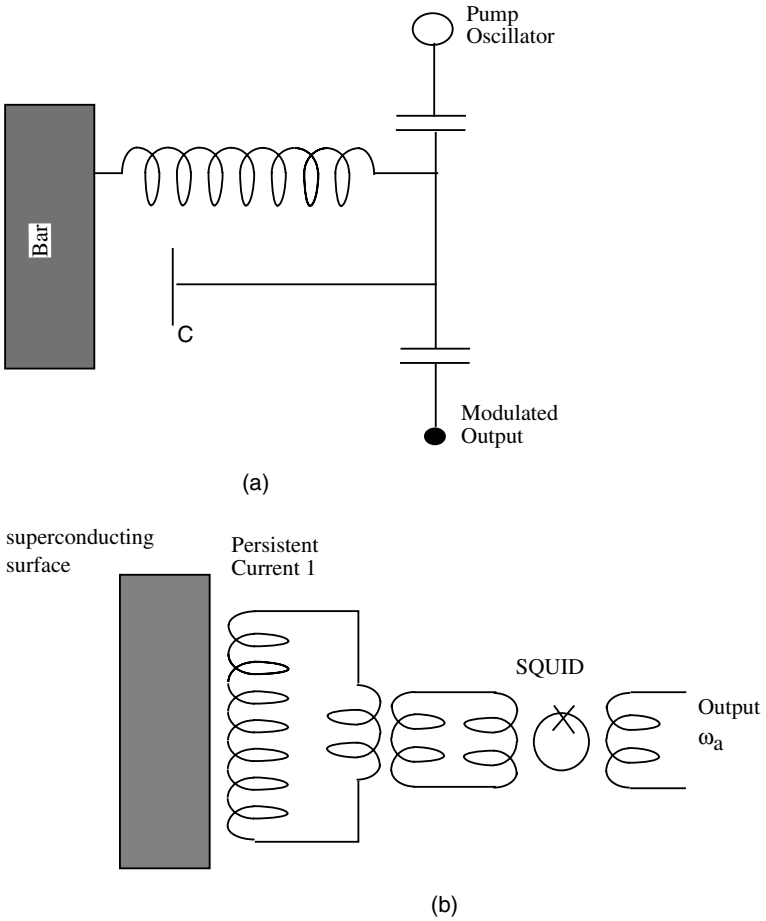

Figure 22. Inductance or capacitance is modulated by a gap spacing. (*a*) Active or parametric transducer use a low-loss resonant circuit pumped by an external oscillator. (*b*) Passive transducers use an inductive or capacitive readout, coupled to a SQUID amplifier. All the circuits are made from superconducting and very-low-loss components.

For the passive inductive transducer

$$\beta_{\text{pass}} = \frac{1}{2}\frac{LI^2}{m\omega_a^2 x^2}. \tag{4.19}$$

Note that the passive transducer coupling factor is not enhanced by a Q-factor term. For a capacitive passive transducer the inductive stored energy $\frac{1}{2}LI^2$ is replaced by the capacitive stored energy $\frac{1}{2}CV^2$. The parametric transducer effectively samples the incoming signal Q_e times per cycle up to a maximum value of ω_p/ω_a, and therefore increases its coupling by the same factor.

Parametric coupling is *reactive* as a result of the position-dependent mechanical forces which act across the electrical resonator. The mechanical forces vary strongly over the transducer *position bandwidth*, defined as the halfwidth of the electrical resonator, measured in terms of displacement. Typically the position bandwidth is ∼pm (10^{-12} m). The stored electrical energy exerts forces across the capacitance which vary strongly over the position

bandwidth. Hence the effective spring constant can be very large, and due to its reactive nature can create problems in maintaining stability.

The passive transducer does not have the same coupling advantage. However, the advantage is to some extent illusory because by moving the coupling structure to a high frequency one reduces its size, so that the absolute value of the L or C is significantly reduced.

The practical problems of the two types of transducer are quite different. Passive transducers are limited by a poorly understood problem of AC losses in their superconducting circuits, and the performance of available SQUID amplifiers. Parametric transducers, on the other hand, are limited by phase noise in the pump oscillator, tuning difficulties, noise degradation in amplifiers at high microwave power, and sometimes by the effects of low-frequency seismic noise. All transducers, both active and passive, are limited in noise performance by the noise of the amplifier with which they are used. In terms of noise number equation (4.13), at 1 kHz a noise number of 1 corresponds to a noise temperature of about 100 nK, whereas at 10GHz the same performance corresponds to $T_n \sim 1$K. In principle, both types of transducer can reach close to the quantum limit. In practice, none have reached this level to date, although SQUID amplifiers have been developed close to 1 μK, and amplifiers for microwave parametric transducers have long been available with $T_n \sim 10$K. The microwave parametric transducer on NIOBE at UWA has achieved about 1 mK noise temperature, while the SQUID transducer on NAUTILUS has achieved similar noise performance. It is not obvious which type of transducer will ultimately be the most successful.

Johnson and Bocko [106–108] and Tobar *et al* [100] have presented designs for quantum-limited microwave transducers, while Richard and the Legnaro group have presented design for optical transducers [109, 110]. See [94, 98, 111, 112] for further discussion of these issues.

A sensitive transducer and a low-loss resonant mass are not sufficient to create a sensitive gravitational wave antenna. There is a major problem at the interface: mechanical impedance matching. The impedance mismatch ratio (introduced as the coupling factor β) arises because the mechanical output impedance of the bar is very high, characterized by the elastic stiffness of the bar itself, whereas the mechanical impedance of the electric or magnetic field which couples this motion into the transducer is not large. The solution is to create an acoustic transformer at the end of the bar. Such a transformer is analogous to acoustic horns used in loudspeakers, or to the mechanisms in the human ear that couple the motion of the air into the fluid of our cochlea.

All successful impedance matching schemes have consisted of low-mass secondary acoustic resonators tuned to the antenna frequency. This creates a two-mode resonator with a pair of normal modes. The acoustic energy beats between the high-mass resonator and the low-mass resonator, while the transducer is coupled to the low mass. The scheme can be generalized to multimode transformers, consisting of nested sets of resonators reducing in mass by a geometric progression.

Three secondary resonator configurations have been used successfully on antennas: diaphragms (first developed by Paik at Stanford [113]), mushrooms (developed by the Rome group [114]) and bending flaps (developed at UWA [115]). Pang and Richard [109], Hamilton *et al* [116] and Tobar [63] have proposed and tested 3–5 mode systems but these have yet to be implemented. Four of the systems are illustrated in figure 23. The antenna NIOBE uses a 400 g bending flap (figure 23(a)). The bending flap is a convenient form of secondary resonator, which has open geometry suitable for an attachment of a microwave re-entry cavity parametric transducer readout. The microwave readout system consists of a carrier suppression interferometer, and a microwave amplifier followed by a demodulation stage. This achieves reasonably high coupling to the microwave transducer, as demonstrated by the fact that the elastic forces provided by the transducer are sufficient to detune the mechanical oscillator by

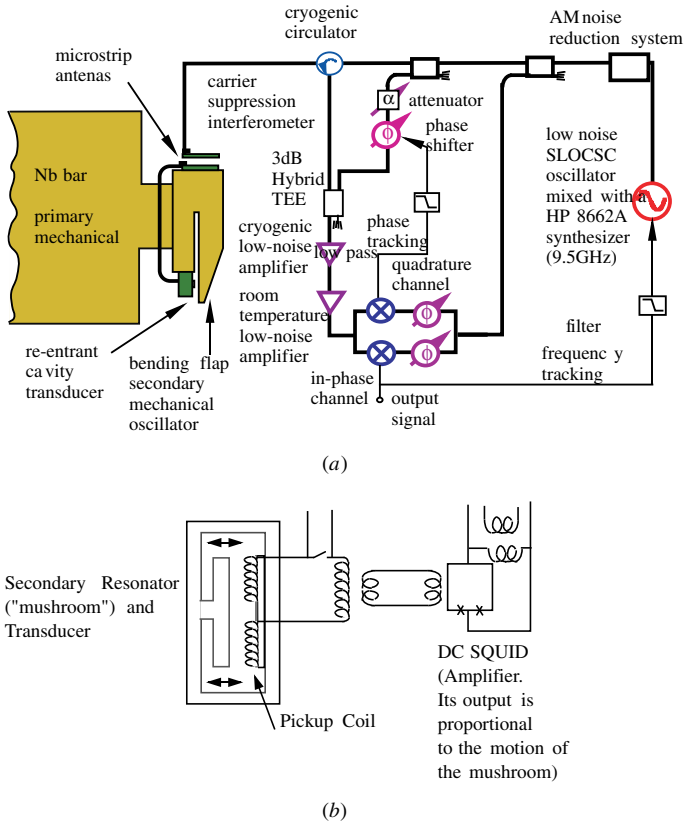

Figure 23. Bar antenna transducer readout systems. (*a*) Bending flap [115]; (*b*) mushroom [114]; (*c*) diaphragm [113]; (*d*) multimode transducer [116].

several Hz. The following three configurations, (*b*) the mushroom, (*c*) the diaphragm and (*d*) a multimode transducer, use similar SQUID amplifier readout circuits. The moving mass modulates the inductance of a flat coil, which by flux conservation leads to a modulated current through a SQUID amplifier. The Rome group has used capacitive readout for a mushroom, in which case currents are induced by charge conservation in capacitor. The multimode transducer uses a massive 'diaphragm' coupled to a small tertiary mass plate supported by small niobium cantilever springs.

4.5. Antenna materials

An ideal resonant bar would consist of a piece of nuclear matter, with high density and a velocity of sound comparable to the velocity of light! Since this is not available except in neutron stars, we must find a form of molecular matter which, to maximize coupling to gravitational waves, combines high velocity of sound v_s, and high density ρ. To reduce the thermal noise we require a low acoustic loss Q^{-1}.

For an antenna limited by thermal noise the best antenna material (at a practical frequency) will have the largest value of $Q\rho v_s^3$. This quantity is proportional to the ratio of energy absorbed ($\sim\rho v_s^3$) and the thermal noise in the antenna ($\sim Q^{-1}$). Of the three controlling parameters, only the Q-factor can be modified significantly in a particular material, depending on its preparation

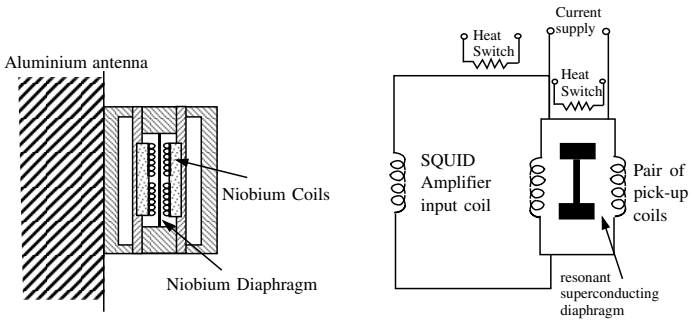

(*c*)

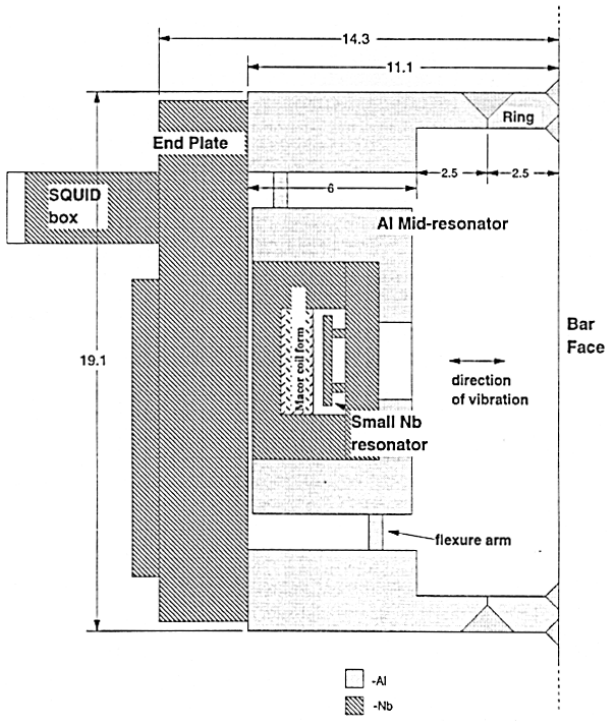

(*d*)

Figure 23. (Continued)

and suspension.

Table 2 lists the values of ρ, v_s and ρv_s^3 for various materials, along with the maximum achieved Q-value to date, and the signal-to-noise ratio figure of merit, $Q\rho v_s^3$. The table shows that nearly one order of magnitude improvement is obtained (at a given frequency) in ρv_s^3 by changing from aluminium or niobium to sapphire, and when the Q-factor is included the very low losses in sapphire make it about 500 times superior to Nb or Al (at a given operating temperature). Silicon is more than 100 times better than Nb and Al. Unfortunately, at present silicon and sapphire are not available in sufficiently large masses for these apparent advantages to be useful. Note that a lower Q-factor can always be compensated for by sufficient

Table 2. Comparison between antenna materials.

Material	ρ(g cm^{-3})	v_s(km s^{-1})	Q	ρv_s^3 (10^{13} kg s^{-3})	$Q\rho v_s^3$ (10^{20} kg s^{-3})
Aluminium 6061	2.7	5.1	5×10^6	36	18
Aluminium 5056	2.7	5.1	7×10^7	36	250
Niobium	8.57	3.4	2.3×10^8	34	800
Silicon	2.33	8.5	2×10^9	140	2.8×10^4
Sapphire	3.98	9.4	3×10^9	330	10^5
Lead	11.36	1.1		1.5	
Tungsten	18.8	4.3		150	
Copper(94)/Al(6)	8.0	4.6	2×10^7	77.8	155

cooling, so that fundamentally only the ρv_s^3 term need be considered. Copper-based alloys have been selected as preferred materials for very-high-mass spherical antennas, chiefly because superconducting materials (for which the thermal conductivity becomes very low) are very difficult to cool to ultralow temperatures.

For comparison, table 2 also shows lead and tungsten. Lead is very poor, because of its low sound velocity, whereas tungsten is comparable to silicon. If massive high-Q tungsten masses could be obtained, they would have the significant advantage that the cryogenic system necessary to house the antenna would be smaller (and cheaper and simpler) than that needed for lower-density materials.

4.6. Antenna suspension and isolation systems

Typical *seismic noise* has the spectrum of $x_s = \alpha f^{-2}$ m Hz$^{-\frac{1}{2}}$ in the frequency range 1 Hz to a few kilohertz, where f is the frequency and α is a constant. Measurements by gravitational wave research groups at various sites have shown that the constant varies between 10^{-6} and 10^{-9} (e.g. [117–119]). A vibration isolation system is needed to isolate seismic noise to well below the signal level at the antenna resonant frequency. A variety of metallic suspensions have been developed for resonant gravitational wave detectors (e.g. [120–122]). All are designed to have the normal-mode resonant frequencies of the isolator well below the antenna frequency, and the internal modes of the isolator elements above the frequency range of interest. In general, the normal modes define a set of low-frequency resonances. Internal modes of the mass and spring elements are generally at high audio frequencies. Such isolators therefore have good isolation above a low-frequency corner, and also below the high-frequency internal resonances. For resonant-bar antennas, the isolation band required is from a few hundred hertz to a few kilohertz. In principle, it is fairly easy to realize a mechanical isolator which will attenuate the seismic motion at 1 kHz ($\sim 10^{-12}$ m Hz) by 10^{10} (e.g. [121, 122]). However, practical problems such as nonlinear up-conversion can degrade the performance [123].

Figures 24 and 25 illustrate two of the resonant-bar antennas constructed to date. For antennas operated at 4 K the bar is supported by a low-loss multistage suspension in an experimental chamber with which the antenna has no direct contact. A room temperature vibration isolation stage suspends the cryogenic suspension stage. In the case of NIOBE, vibration can only act on the antenna by traversing the entire 18 stages of vibration isolation, or through transmission through the residual gas in the experimental vacuum. There are no wires connecting to the antenna (which can transmit vibration) because the transducer is

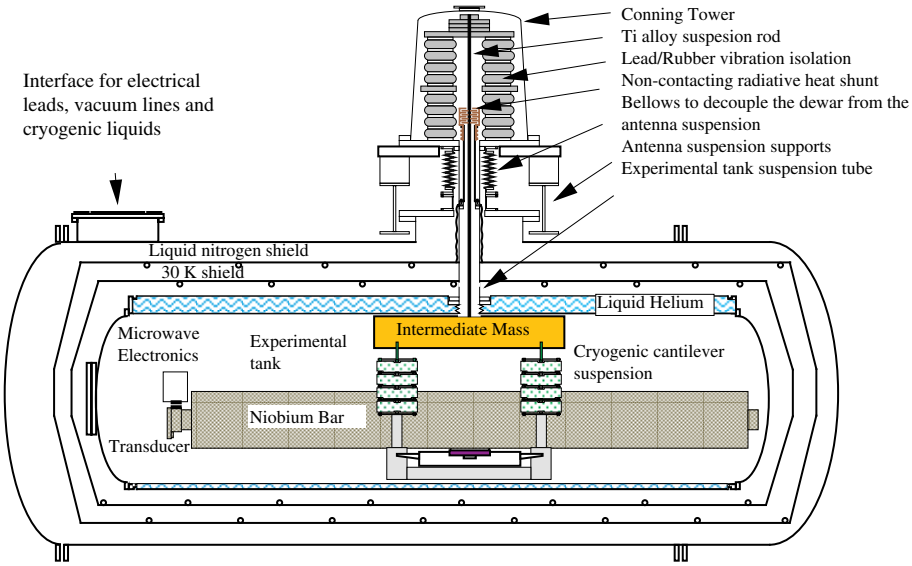

Figure 24. Cross section of the NIOBE antenna. The cryostat is 5 m long and 3 m high.

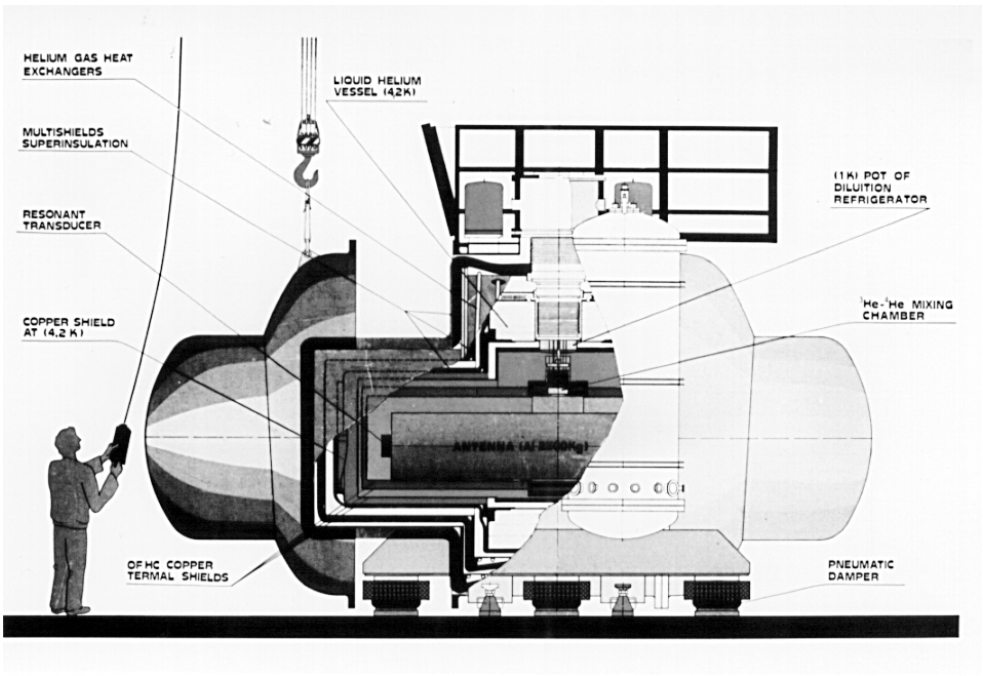

Figure 25. View of the ultracryogenic antenna AURIGA showing cryogenic shields and the Al bar.

interrogated entirely by radiative contact. In the case of antennas using passive transducers superconducting cables can act as transmission lines to conduct vibration, so that great care must be taken to isolate cables using *Taber isolators* [124], consisting of additional mass spring stages (using thin wires as springs) to which the cables are bonded.

The *cryogenic suspension and isolation stage* of an antenna is one of the most critical components. It must isolate against the noise which bypasses room temperature isolation, as well as the thermal noise of the room temperature stage. In addition, it must suspend the antenna using low-loss elements so as to maintain a high antenna quality factor. It is essential that the cryogenic stage, at least, does not have any resonant modes near the antenna frequency. Several different systems have been used with reasonable success. Traditionally, cable suspensions have been used: a cable slung around the belly of the resonant bar. This method has the risk of introducing vibration by the violin string mechanism: slip–stick frictional transitions associated with the motion of the belly cable at the point of tangential contact with the bar. This process arises because of the seismically driven low-frequency pendulum motion of the bar. Such boundary condition effects can be avoided if the antenna is somehow bonded or clamped to the bar at the tangent point. The now defunct Stanford group and the LSU group used welded rods instead of wires to avoid this problem. The third method consists of a cantilever suspension. High Q-factor curved cantilever springs such as the Catherine wheel used on NIOBE support the bar from below. This can have well defined contact points to the antenna to minimize nonlinear processes, and has given the highest Q-factor ever observed in a metal [125]. A fourth method, first suggested by Coccia [126], is the use of a nodal point suspension. In the case of a bar or sphere, the nodal point for the fundamental mode is located at the centre of mass. This means boring a hole to the centre and attaching a rod or cable. While this has many advantages in reducing sensitivity to external noise, it has not been used in a full-scale antenna.

Antennas cooled to ultracryogenic temperatures (below 100 mK) have a particular problem to contend with. Helium exchange gas can no longer be used at such temperatures (the vapour pressure is too low) so the antenna must be cooled by conduction. This means that there must be direct cryogenic conduction paths to the antenna from the dilution refrigerator. Pure and nonsuperconducting metals must be used (such as OFHC copper). Yet the thermal conduction must exist without significant vibration conduction, especially since the dilution refrigerator is likely to be a substantial source of vibration.

Ultracryogenic detectors used to date have exhibited excess sensitivity to local vibration, due presumably to the inadequate performance of the thermal conduction/vibration isolation system. However, recently both NAUTILUS and AURIGA have yielded improved performance, down to a noise temperature of 1 mK.

4.7. Present status of resonant-mass detectors

At the time of writing five resonant-mass gravitational wave detectors are in operation. These consist of three liquid helium temperature detectors, ALLEGRO, EXPLORER and NIOBE at Louisiana State University, CERN (operated by the University of Rome Group) and the University of Western Australia, and two ultracryogenic detectors, NAUTILUS and AURIGA at INFN Frascati and INFN Legnaro, Italy. The latter detectors have been successfully cooled to below 100 mK. Table 3 below summarizes the basic parameters of these antennas. The noise performances quoted are typical/best rms noise levels for the detection of broadband bursts.

As well as undertaking long periods of operation, the antennas are all in the process of upgrade, either through installation of improved transducers, or through installation of improved vibration isolation. Due to the large size of the cryogenic systems, resonant antennas have a rather long cycle time (several months) of cooling and warm-up. Combined with the probability of malfunction in experimental apparatus (a particular problem during the 1980s) the rate of progress has been slower than predicted.

Table 3. The resonant mass detectors which belong to the international Gravitational Events Collaboration.

Antenna	Location	Material	Temperature	Noise Temperature (mK)	Frequency (Hz)	Strain sensitivity
ALLEGRO	Baton Rouge	Al	4 K	6	900	7×10^{-19}
EXPLORER	CERN	Al	2 K	6	900	7×10^{-19}
NIOBE	Perth	Nb	5 K	1	700	5×10^{-19}
NAUTILUS	Frascati	Al	100 mK	4	900	6×10^{-19}
AURIGA	Legnaro	Al	100 mK	1	900	3×10^{-19}

4.8. Performance of resonant bars

The long-term operation of cryogenic resonant bars has been invaluable in characterizing their instantaneous performance, and evaluating various possible filtering techniques for extracting events from a long data record in the presence of excess noise. With regard to instantaneous performance it has been important to verify that the noise performance is consistent with the noise parameters of the bar, transducer and readout system. In nearly all cases extremely good agreement has been obtained, such as illustrated in figure 26. In the case of parametric transducers their performance can be characterized not only by noise spectra, but also by their variable interaction with the antenna, as discussed in section 4.5.

From the experimentally observed noise spectral density, such as figure 26, one can determine the sensitivity of the antenna to various signals such as stochastic background, CW signals and bursts. Figure 27 shows the calibrated burst sensitivity of NIOBE during a 24 h period. The data are presented as mean noise temperature (bottom curve) and the largest noise temperature observed in 100 s. This allows the antenna performance to be quickly assessed, including the presence of excess noise. Figure 28 presents the same data in the form of Brownian motion noise histograms. From the single antenna data there are clearly few events above 10 mK, corresponding to $h \sim 10^{-15}$ (all of these could normally be eliminated by coincidence analysis.

The resonant-bar detector network has recently been able to set new upper limits to the strength and event rate of gravitational wave burst signals from coincidence analysis of three- and four-antenna data. Figure 29 shows this result in comparison with previous upper limits [127].

We saw in section 4.2 that the noise energy for burst detection is reduced by the factor τ_i/τ_a, where τ_i is the signal integration time and τ_a is the antenna ring-down time. The reduction of the noise with τ_a is a manifestation of the fluctuation dissipation theorem. In the case of CW signal detection the noise energy reduces proportional to $(\tau_i \tau_a)^{-1}$. This means again that the best detector is one with very high Q-factor, and that very long integration times improve the amplitude sensitivity as $\tau_i^{1/2}$. Figure 30 presents an FFT analysis of one month's data from the ALLEGRO detector in the search for pulsar signals form the globular cluster 47 Tucanae. In this case the deep integration, over a narrow frequency band, has set limits for CW pulsar signals $\sim 10^{-23}$. The analysis has been repeated for various directions in the two low-noise bands of ALLEGRO.

For the detection of stochastic backgrounds one simply has to multiply the output of two nearby detectors and integrate the result. However, as discussed in section 3, the detectors need to be sufficiently close that the incoming waves are correlated. Their space should be within about $\lambda/3$ where λ is the gravitational wave wavelength c/f. Cross correlation between the detectors NAUTILUS and EXPLORER (as mentioned in section 3) have yielded a limit to

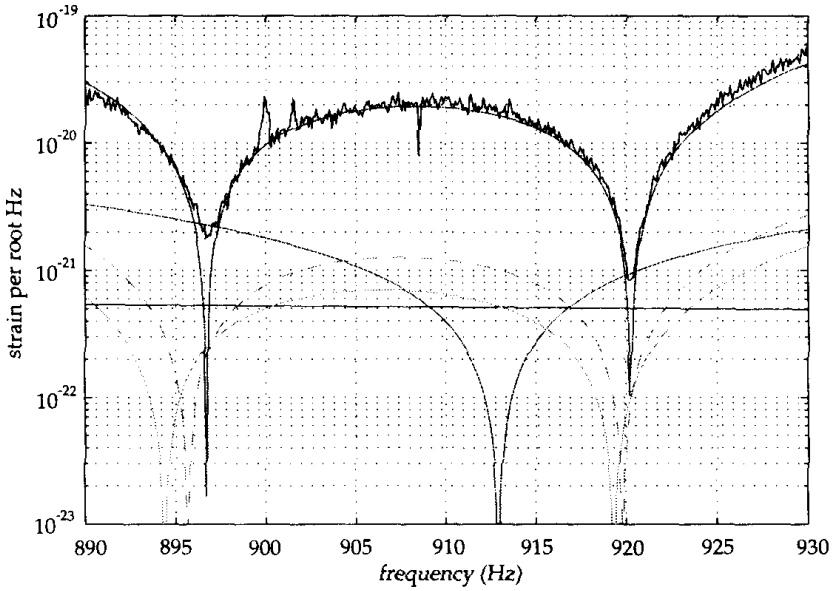

Figure 26. The measured strain noise of ALLEGRO, shown as the irregular trace. The various noise contributions estimated from the noise model are shown as smooth curves. The noise is dominated by the SQUID's wide-band and the transducer's narrow-band noise [71].

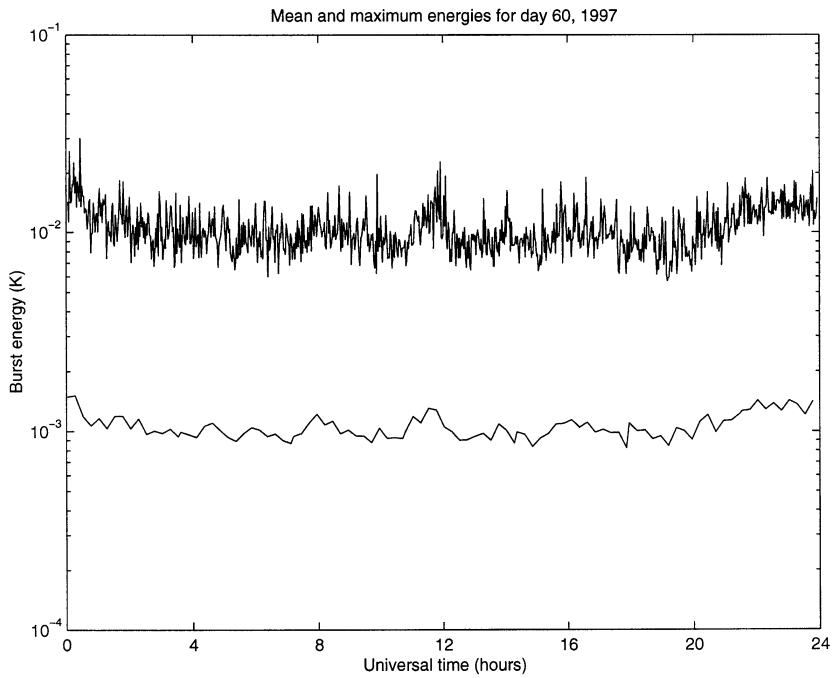

Figure 27. The calibrated burst sensitivity of NIOBE during a 24 h period. The data are presented as mean noise temperature (bottom curve) and the largest noise temperature observed in 100 s [78].

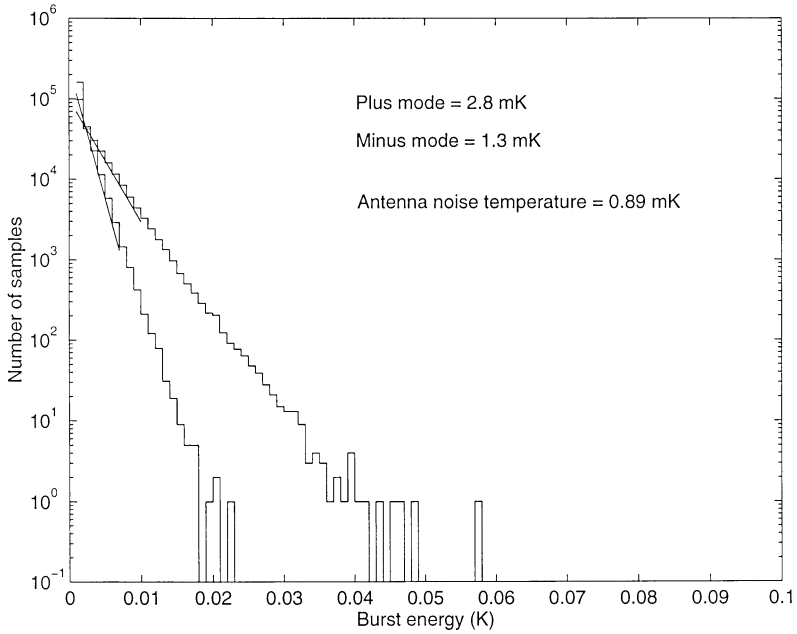

Figure 28. Histogram of the noise of NIOBE after optimal filtering for burst signals, showing the expected Boltzmann distribution. When the weighted mean of both normal modes is evaluated the overall system noise temperature is 0.89 mK.

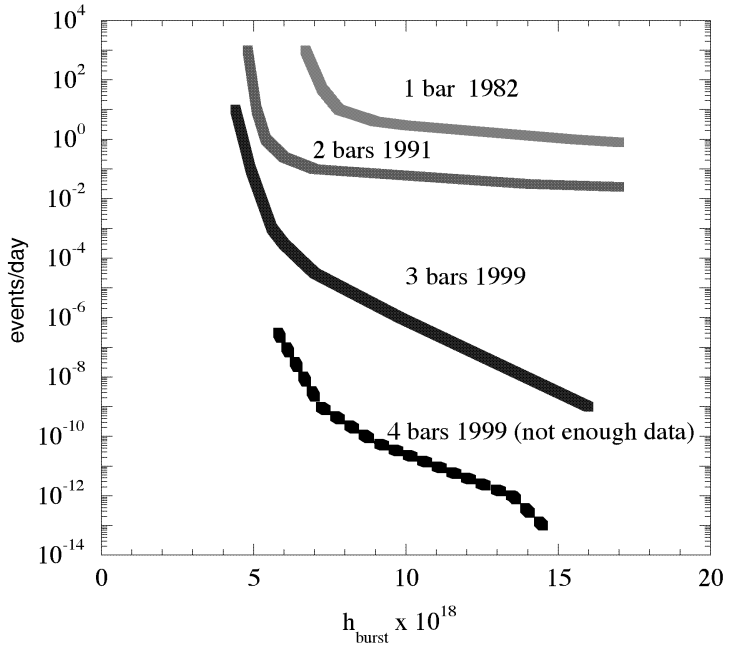

Figure 29. The rate of burst events versus strain amplitude set by one-two-three- and four-antenna experiments. The 4-antenna result is based on a short period of data and hence has weaker significance.

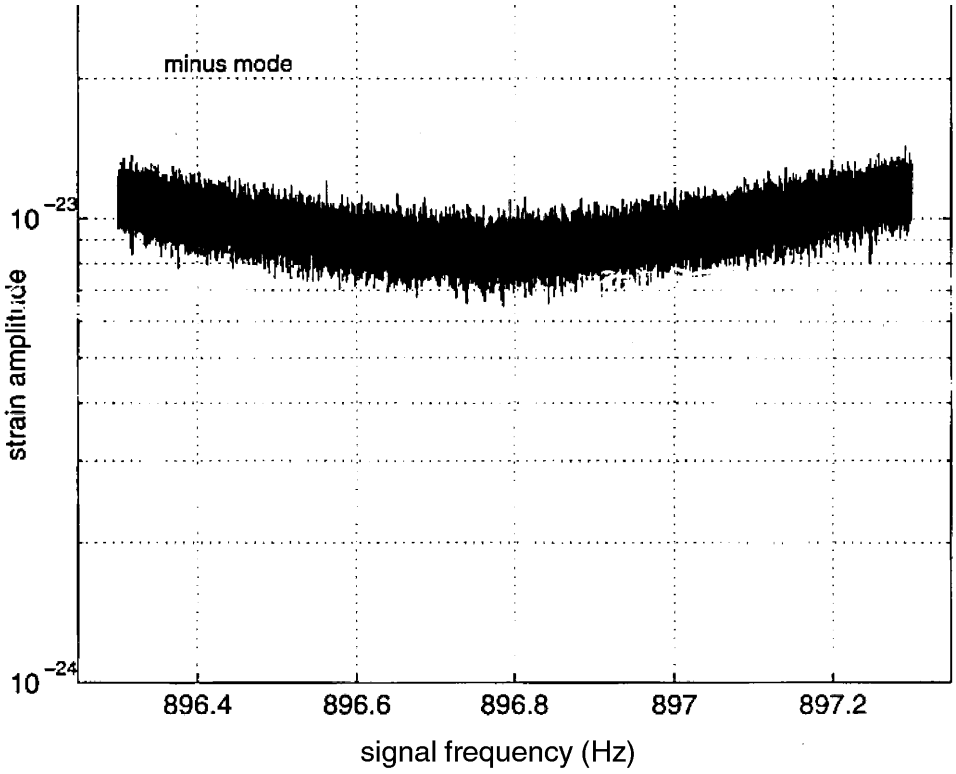

Figure 30. Search for narrow-band continuous waves from possible pulsars in 47 Tucanae [71]. Over about 1 Hz range no CW signal is visible above a strain amplitude $\sim 10^{-23}$.

stochastic gravitational waves of $\sim 10^{-22}$ at 900 Hz. The results achieved were limited because the detectors were too far apart. Vitale *et al* [128] have shown that NAUTILUS and AURIGA can be expected to achieve improvement of more than two orders of magnitude over this figure. However, they should be located within about 100 km of each other to achieve best sensitivity. This would bring the sensitivity to within the range of possible stochastic signals from the era of early star formation.

4.9. Multiple antenna correlation

In the future we can expect detailed correlation experiments to take place between a worldwide array consisting of both resonant-mass and laser interferometer gravitational wave detectors. The analysis would take into account the relative amplitude of the signals observed by detectors with different orientations relative to an incoming signal, and the phase delay due to the propagation time of signals through the Earth. Such a combined analysis would allow source direction and polarization to be accurately determined. Today we are still far from achieving this goal. Here we will discuss the analysis performed to date on data from a far less optimal array.

Besides seismic noise excitation, all cryogenic antennas have shown evidence of excess noise of indeterminate origin [81], as mentioned in section 3. Low noise performance may be achieved for considerable periods of time; but interspersed are periods of excess noise which

is not identifiably correlated with known noise sources. This can degrade performance by many orders of magnitude. While there are opportunities (as discussed above) for nonlinear up-conversion driven by low-frequency pendular modes, and also for thermal-stress-driven excitation as regions of the cryostat vary in temperature, no firm correlation is generally apparent. Thus the seismic, acoustic, electromagnetic pulse and cosmic ray shower detectors that are generally used to discriminate possible noise signals are not sufficient to eliminate excess noise, and much careful work still needs to be done. It has been shown that at a noise temperature of $\sim$1 mK about 2 cosmic ray events will occur per day, and this increases to 103 events per day at the 1 μK noise sensitivity [129]. The Rome group has convincingly demonstrated the presence of cosmic ray excitation events in their data [130].

Multiple antenna coincidence correlation can minimize the effects of excess noise, as demonstrated by many coincidence experiments (e.g. [131]), which sets new lower limits on the gravitational wave flux. When four or more antennas are operated in coincidence the rate of accidental coincidences becomes extremely small, as we discuss further below.

Candidate gravitational wave events consist of either unknown environmental perturbations, occasional rare Gaussian high-energy excursions, and possibly real gravitational wave signals. These may be idealized as an independent set of background events, occurring at a constant rate R per unit time. There is evidence that the background events are not entirely independent but to some extent are clustered. This can occur if a local vibration source acts over a period of time. In spite of this, the data are generally well described by a Poisson distribution.

The probability of a background event in one antenna during the antenna resolving time τ_r is given by

$$P_1 = R\tau_r. \tag{4.20}$$

Now if there are N independent antennas, the probability of accidental coincident excitation of all N antennas in a coincidence window τ_c that must always satisfy $\tau_c \geqslant \tau_r$, is given by the product

$$P_N = \tau_c^N \prod_{i=1,N} R_i. \tag{4.21}$$

If we simplify by assuming that all antennas experience the same background at the rate R, equation (4.21) becomes

$$P_N = R^N \tau_c^N. \tag{4.22}$$

From this it follows that the mean number of accidental coincidences during a coincidence experiment of duration $t_{\rm tot}$ is given by

$$N_{ac} = R^N \tau_c^{N-1} \cdot t_{\rm tot}. \tag{4.23}$$

Table 4 summarizes the mean number of accidental coincidences for experiments with one or more detectors, assuming various coincidence windows. The coincidence window depends on several factors. It cannot be smaller than the poorest clock precision of the detectors in the experiment. Second, it depends on the timing resolution of the optimal filters in the antenna readout. The latter depends on the signal size, but for the typical thresholds used to extract candidate events it is about 0.1 of the optimum integration time. At the improved antenna sensitivity expected in the near future, cosmic ray events could produce one event per 100 s (10^3 events per day). To detect rare events such as gravitational waves from supernovae in our Galaxy, we should be looking for $N_{ac} < 1$ in any coincidence experiment. The probability that a single coincidence is accidental is given roughly by the value of N_{ac} (for N_{ac} less than 1).

Table 4 emphasizes that multiple antenna operation is essential to reduce the background coincidence rate. Two-way coincidence experiments to date have been meaningful because

Table 4. Mean number of accidental coincidences for $R = 10^{-2}$ s^{-1} in a four-month (10^7 s) coincidence experiment.

Number of antennas	Coincidence window (s)			
	1	0.1	0.01	0.001
1	10^5	10^5	10^5	10^5
2	10^3	10^2	10	1
3	10	0.1	10^{-3}	10^{-5}
4	0.1	10^{-4}	10^{-7}	10^{-10}
5	10^{-3}	10^{-7}	10^{-11}	10^{-15}

$R < 3 \times 10^{-4}$ has usually been achieved. At the increased rate of candidate events expected due to cosmic rays as sensitivity improves towards $h \sim 10^{-20}$, it will be difficult to obtain significant data unless at least three detectors are used, or else if separate vetos can eliminate the cosmic rays themselves. The very low probability of accidental coincidences achievable with four- and five-antenna arrays apparent in table 4 demonstrates that with high time resolution it is possible to eliminate a substantially larger background than the assumed value of R. For example, even if R was increased to 1 s^{-1}, the probability of a five-way accidental coincidence using the smallest assumed window is 10^{-5} in a four-month experiment. Note that if the antennas have different resolving times, the τ_c used in equation (4.23) must be greater than the longest resolving time.

The issue of multiple antenna coincidences is not as simple as indicated above due to the fact that the antennas have varying orientations on the surface of the globe. The angular dependence of the signal S observed in a single resonant-bar antenna is given by

$$S(\theta, \phi, \varepsilon) = (0.5(1 - \varepsilon) + \varepsilon \cos^2 2\phi) \sin^4 \theta, \tag{4.24}$$

where θ is the angle of the incoming plane wave relative to the cylinder axis of the antenna, and ϕ is the polarization angle of the wave measured relative to the plane of the antenna and the source. The polarization fraction ε measures the fraction of linear polarization of the wave. For $\varepsilon = 0$ the wave is circularly polarized, whereas for $\varepsilon = 1$ the wave is 100% linearly polarized, with polarization angle ϕ.

To assess the probability of multiple antenna coincidences we must investigate the antenna pattern of a set of antennas on the globe. Since all antennas are horizontal, their orientation with respect to the sky is largely determined by their locations on the Earth, and considered as a whole this leads to a complex antenna pattern when the responses S as given by equation (4.24) are combined into a synthetic multiple antenna pattern. Antenna patterns for one and two resonant-bar antennas have been analysed by Frasca [132] and Nitti [133]; Blair and Frasca *et al* have analysed multiple antenna arrays [134], while Schutz and Tinto [135] have analysed antenna patterns for pairs of laser interferometers.

An analysis of antenna patterns for the geographical locations of four antennas [134] shows that four antennas are sufficient to obtain near-100% sky coverage for two-way coincidences. That is, if we are content with only two antennas being suitably aligned for a random source, we can observe practically 100% of the sky. On the other hand, if we are to demand four-antenna coincidences then we require the antenna orientations to be adjusted such that they optimally search the same part of the sky, and the sky coverage is reduced to about 50%. With eight operating antennas one can achieve near-100% sky coverage and a minimum of four antennas in coincidence for any one event. Note, however, that since spherical antennas have 100% sky coverage, such an eight-antenna array could be replaced by three or four spherical antennas, thus avoiding the sky coverage problem.

We now return to the practical problems of the existing array of bars. We have seen that the presence of local sources of background noise lead to the minimum detection requirement that a two-antenna zero time delay coincidence be observed. With unknown source direction we can apply no constraint on the signal based on the relative size of the signal observed in each antenna. However, it is possible to utilize the fact that the rotation of the Earth causes the antenna sensitivity to be strongly modulated for specific source directions. For example, it may be reasonable to consider that the nearest sources (such as coalescing black holes) will be concentrated near the galactic centre. Under this assumption one can reject data when the antenna sensitivity in this direction (defined by equation (4.24)) is below some predetermined value. Due to the $\sin^4\theta$ factor in equation (4.20) this provides a rather steep angular cut-off and in practice one can eliminate $\sim$50% of data by applying such a *direction filter*. This automatically reduces the number of accidental coincidences (since these occur randomly in sidereal time) and increases the statistical significance of any zero time delay excess). Such a procedure is statistically dangerous, however. The reason for this is that there will always be some direction in which an apparent excess is statistically significant. The direction and the cut-off threshold must always be preset before the analysis.

A second means of improving the statistical significance of the data rests on the fact that the energy distribution for true signals (such as gravitational waves or calibration pulses) is different from the distribution of excess noise events. This is easy to verify experimentally. Astone *et al* [136] have shown that the energy resolution achievable in a typical resonant bar with a threshold for candidate events about 10 times the mean noise energy is uncertain within a range typically 0.3–3 (for signal energy $= 1$). This uncertainty has been verified experimentally, indicating that the use of relative amplitudes to determine source direction can only be used effectively at large signal-to-noise ratio [137]. While this energy spread is large, the energy spread of accidental coincidences is always much larger, typically spanning up to two orders of magnitude. This follows immediately from the high effective temperature of the excess noise distribution (see figure 17). As a result one can apply an energy ratio filter to coincidence data, thereby eliminating from consideration any coincidences for which the energy ratio exceeds a predetermined value. (This depends on the relative orientation of the detectors, and on their excess noise distribution.) Appropriate criteria can be set for such filters based on the measured distribution of non-true-time coincidences. In practice this scheme allows about 50% of the total coincidences to be excluded, again allowing substantial improvement in the statistical significance.

In an unpublished NIOBE–EXPLORER coincidence experiment a total of about 25 zero time delay coincidences was reduced to a total of seven coincidences by the application of both an energy ratio filter and a galactic centre direction filter. This figure was substantially above the background, but timing uncertainties and the fact that these filters were developed during the data analysis period ruled out attribution of statistical significance to the result. If it had been a blind experiment and there had not been timing uncertainties the probability of the zero time delay peak occurring by chance would have been improved from $\sim$0.01 to $\sim 3 \times 10^{-4}$. Future experiments can utilize one or both of the above filters to improve statistics. It is a technique that is likely to be applicable in the search for burst sources in laser interferometer detectors.

4.10. Future prospects

4.10.1. Spherical gravitational wave detectors. Spherical gravitational wave detectors have been analysed extensively by Coccia and co-workers [138–143], Johnson and Merkowitz [34, 144], Zhou and Michelson [145] and Stevenson *et al* [146–149]. A spherical detector consists

of a large approximately spherical mass instrumented with five or more transducers to read out the orthogonal quadrupole modes and the gravitational wave insensitive monopole mode. Such a detector has a high cross section for gravitational waves and omnidirectional sensitivity. A spherical detector can be suspended close to its centre of mass to achieve quite good decoupling of the suspension from the antenna normal modes. This cannot be perfect however, because of another problem: the matching of transducers to the large normal mode masses. All operating resonant-bar transducers use a secondary resonator to match the antenna normal mode mass (about one tonne) to the transducer (see section 4.4). Typically, the secondary resonator (such as the UWA bending flap, figure 23) has a mass of several hundred grams. This is roughly the maximum mass that can be coupled to existing transducers with electromechanical coupling coefficient in the range $1–10^{-3}$.

In the case of a 100 tonne sphere aiming for high sensitivity to bursts in the kHz range, the impedance matching problem is more complex. The maximum effective bandwidth of a two-mode system is set by the beat frequency between the two normal modes. This is given by $\Delta f = f_0(M_1/M_2)^{1/2}$. For a 1000:1 mass ratio this represents a bandwidth of 3%. Since bandwidth translates directly into burst sensitivity, it is necessary to reduce this ratio, which can best be done with a multistage impedance matching network. A reasonable choice is a factor of about 30, which gives a fractional bandwidth of $(\frac{1}{30})^{1/2}$, or about 18%. However, to match to a transducer using such mass ratios between a 50 tonne normal mode mass and a 50 g transducer coupling mass requires the use of four stages, with the second-stage resonator exceeding 1 tonne, a third-stage resonator of tens of kilos, coupled to the final low-mass transducer stage. The sphere becomes a rather hairy sphere, possessing not five fundamental quadrupole modes that couple to gravitational waves, but 20. Care must be taken that there are no adverse couplings between the normal modes, since perfect orthogonality will be difficult to achieve in such a complex structure. Negligible cross-coupling can easily be achieved by deliberately choosing coupling mass parameters such that all modes are offset from each other by a few Hz.

A scheme for creating some of the additional resonators required on a sphere is illustrated in figure 31. It makes use of bending flaps, which have the advantage that they have low surface-to-mass ratio (to minimize surface losses), simple geometry for fabrication, and minimum wasted volume. The first intermediate mass is realized by simple machining of the sphere. The second could be welded or cast *in situ*, or it could also be cut from the first intermediate mass by suitable machining (the latter would save more space but has been omitted in the figure for clarity). Just two of the necessary five resonator structures are shown here. This design concept ensures that the antenna and most of the impedance matching system can be fabricated with complete mechanical integrity, thus avoiding unmodelled losses from bolts or glue joints. Here it is worth pointing out that the presence or absence of cylindrical symmetry is not an issue in antenna design, as demonstrated in the NIOBE bending flap at UWA. For large mass ratios the symmetry breaking creates a very small torsional reaction at the suspension point, which could only modify losses if the suspension itself had very large differences in acoustic losses for different degrees of freedom. In reality, suspension systems must be designed to isolate all linear and rotational degrees of freedom since intrinsic cross-coupling always occurs, determined by the Poisson ratio which has a value $\sim$0.3 in all pure homogeneous materials.

The final transducer stage on a spherical antenna can follow the noncontacting microwave parametric transducer concept to avoid the need for cable isolation and save space in the ultracryogenic volume. The transducer could be a sapphire transducer [150–152] or it could be a superconducting re-entrant cavity, as shown in figure 23. For ultralow-temperature applications it is necessary that the transducer have low power dissipation, generally below 1–10 μW. This requires the transducer losses to be lower than niobium transducers demonstrated

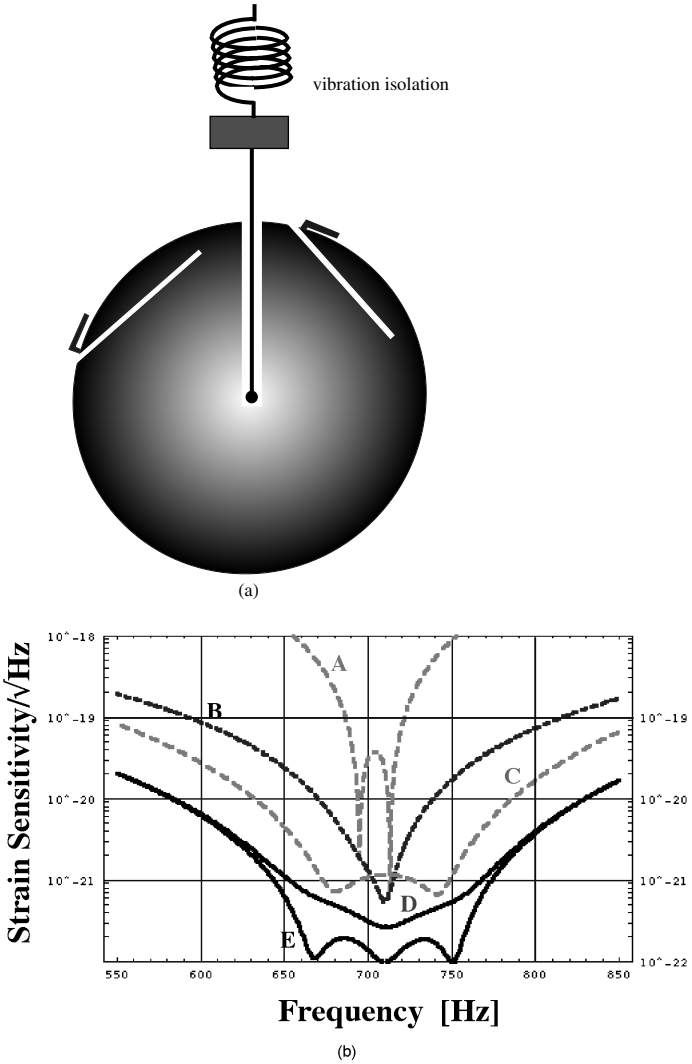

Figure 31. (*a*) A 100 tonne spherical antenna with two of the five cuts required to create ∼1 tonne secondary resonators to readout the orthogonal normal modes. To each secondary resonator is bonded a bending flap ∼30 kg to create the third normal mode of the impedance matching network. The fourth resonator (too small to show here) would consist of an additional bending flap of mass ∼50 g. A parametric transducer could read out such an antenna using radiative coupling thus avoiding vibration coupling through wires. (*b*) [153] Noise performance of a similar spherical detector. Curves A–E show the increasing bandwidth as the number of secondary resonators increased from 1 to 5 respectively.

so far. However, this can easily be achieved by using a larger gap spacing, and a frequency below 10 GHz. In the case of sapphire transducers, sideband pumping allows the dissipated power to be reduced below 1 μW. Figure 31(*b*) [153] shows that broadband noise performance ∼250 Hz can be achieved with a four-mode transducer on a large sphere. The bandwidth is significantly degraded as the number of modes is reduced.

At the transducer it becomes necessary to make a materials transition from the Al or Cu–

Al antenna material, to niobium or sapphire. No definitive solutions for such transitions have been defined, but shrink fitting (by thermal differential contraction), glue bonding or brazing are likely to allow suitably low-loss assembly. It will be important to develop bonding systems in small-scale tests before construction of large-scale spheres.

Spherical detectors cooled to ultralow temperatures can offer difficulties in cooling due to their small surface-to-mass ratio. Frossati has determined that forced convective cooling is essential if the cooling time is to be reasonable. If the material is superconducting, thermal conductivity freeze-out makes this a much more severe problem. For this reason Cu–Al and Be–Cu have been proposed for the antenna material.

4.10.2. Arrays of small high-frequency detectors. A part of the gravitational wave spectrum that has had insufficient attention is the high-frequency band between 2 and 20 kHz. In this band one expects gravitational waves from stellar mass black hole formation and their normal modes. At high frequencies, laser interferometers lose sensitivity due to shot noise, while resonant-mass detectors lose sensitivity due to the smaller size required for such high resonant frequency. Frasca and Papa [154] has proposed a solution consisting of phase coherent arrays of short stumpy antennas, designed so that that all five lower quadrupolar modes (the longitudinal mode, the two discoidal modes and the two 'pantograph' modes) have comparable quadrupole moment and sensitivity. Using five transducers, such stumpies can be read out similarly to the five quadrupole modes of a sphere, and thus have omnidirectional sensitivity. In principle, the total energy sensitivity increases linearly with the total detector mass, so that an array can be enlarged arbitrarily by simply adding additional identical elements.

Whereas a large sphere achieves high sensitivity in a single device, but at the expense of a rather low resonant frequency, the array of stumpies is claimed to achieve the same sensitivity at an arbitrarily high frequency, chosen by astrophysical considerations. It can have cost advantages too, through replication of identical elements.

Such an array obviously requires the individual elements to be sensitive to the same part of the spectrum. However, with adequate impedance matching the stumpies should have bandwidth $\sim$15% similar to that achievable in spheres and bars. This means that there is minimal difficulty in tuning individual detectors.

However, the practical limitations to achieving high sensitivity, such as the limits imposed by noise, have yet to be demonstrated. Further research in this area would be very valuable, including an in-principle demonstration of the concept using calibration signals. The array of stumpies provides an opportunity to achieve great increases in high-frequency sensitivity in the future, but will probably not be implemented until positive results are obtained with existing detectors, or astrophysics provides a very strong justification for improved high-frequency sensitivity.

4.10.3. Transducer developments and prospects. The implementation of improved transducers and impedance matching structures is essential to increasing the bandwidth and burst sensitivity of resonant-mass detectors. Successful transducers have been developed based on capacitative or inductive modulated superconducting circuits with RF or DC SQUID amplifiers, as well as microwave parametric transducers based on superconducting cavities and cryogenic GaAsFET amplifiers. Both systems have comparable sensitivity and a variety of advantages and disadvantages.

The sensitivity of a SQUID-based transducer depends on the SQUID noise performance, and on the mechanical and electrical quality factors of the superconducting elements. A persistent problem has been AC electrical losses in the niobium superconducting coils used for

sensing and coupling transformers in passive transducers. It has sometimes been difficult to obtain sufficient trapped persistent current in inductive sensing circuits, and sufficient electric field across capacitative sense elements. AC losses introduce thermal noise, while low current or electric field reduces the forward transductance, reducing the electromechanical coupling and increasing the antenna noise temperature.

A critical factor for SQUID transducers is the SQUID noise. Recently there has been progress in this area. Two groups have created SQUIDs with noise measured to be below about $30\hbar$, one to two orders of magnitude better than commercial devices. However, recent results [155] indicate that noise is degraded in a transducer environment due probably to trapped flux.

Parametric transducer performance also depends on the mechanical and electrical quality factor of the transducer structure. This is less of a problem however, since the simpler mechanical structures used have shown Q-factors $\sim 10^7$, and electrical Q-factors $\sim 10^5$–10^6, both of which are high enough to be negligible noise sources at current sensitivity. Microwave amplifiers have for many years been shown in radio astronomy to have near-quantum-limited noise, but in the only successful such implementation the amplifier noise contribution is in excess of this [156]. Critical to achieving excellent amplifier noise is very low signal levels, requiring excellent carrier suppression, since otherwise pump power reflected from the cavity greatly exceeds the signal sidebands.

Another critical problem is pump oscillator phase noise. The NIOBE transducer required an ultralow phase noise microwave oscillator to be especially developed.

To achieve sensitivity near to the quantum limit with a parametric transducer will require a higher Q-factor electrical resonator and a lower noise pump oscillator. Fortunately, oscillators 30 dB better than that used on NIOBE have now been developed, and a sapphire transducer with mechanical and electrical Q-factor exceeding 10^8 should allow this technology to advance to within a factor $\sim$30 of the quantum limit [100, 152, 157].

4.11. Vibration isolation and suspension developments

The vibration isolation and suspension system for resonant-mass detectors has always consisted of both room temperature and cryogenic isolation stages such as those discussed above. In the case of ultracryogenic detectors there has been greater emphasis on cryogenic isolation but careful isolation of the cryostat structure itself has been necessary to prevent local disturbances. It is tempting but incorrect to consider the vibration isolation problem solved, since improvements of more than 1000-fold in energy sensitivity are projected, and already detectors show signs of inadequate isolation. In the case of NIOBE there are signs of variable noise temperature by about a factor of two which is observed as degrading mode temperature without change to the wideband noise. Sometimes diurnal variations associated with human activity are observed. This can be understood as arising from vibrational short circuits, perhaps due to a small piece of superinsulation or whiskers of solid air crossing the narrow spaces in the radiative cooler in the suspension tube, or residual conduction through the low pressure (10^{-5} torr) gas in the experimental volume.

EXPLORER is operated at 2 K, below the helium superfluid transition to eliminate the vibrational effects of boiling liquid helium, which otherwise causes degraded performance. NAUTILUS operates well only when local activity is low, again indicating inadequate vibration isolation. Thus it appears that all currently operating detectors are operating close to a vibration isolation limited noise floor, at which improved antennas and transducers will not provide the anticipated noise advantages.

In principle, isolation can be easily improved by further isolation stages, such as the

cantilever spring stages used at UWA. However, short circuits can easily occur, especially through unmodelled resonances in components such as masses, springs or wires, which can cause catastrophic degradation of performance. Not only great care, but excellent design and deep understanding of complex mechanical structures is essential. One point in favour of advanced detectors such as spheres is the advantage of near-nodal-point suspension achieved using centre of mass suspension [126], which can improve isolation by 40–60 dB depending on the proximity of the suspension point to the node. As already emphasized, this can never be perfect due to the finite size of suspension elements and the multimode nature of detectors.

4.12. Conclusion

Resonant bars have been brought to a high level of development. There is now an excellent understanding of the technology and clear proposals for substantial future advances. In particular, it is likely that large spherical detectors will be found to be the best solution for obtaining high sensitivity in the 1–10 kHz range. Meanwhile, an extremely vigorous research effort in laser interferometer detectors is underway, as discussed in the next section.

5. Interferometer detectors

5.1. History

The Michelson interferometer has long been known as an extremely sensitive instrument to measure length changes. The idea of using a laser interferometer as a gravitational wave detector was suggested as early as the 1960s [65, 158] and experimentally investigated in the 1970s [66, 159, 160]. But the first experimental attempt, giving high sensitivity to the displacement of test masses was due to Forward [161]. Forward used a retro-reflector to reflect a beam to a beamsplitter and used active control for locking the interferometer to a fringe. He obtained a spectral strain sensitivity of 2×10^{-16} Hz$^{-\frac{1}{2}}$. The state of the art in sensitive interferometers at the time of writing is represented by three prototype instruments of 10 to 40 m in arm length. These are at Garching [162], Glasgow [163] and CalTech [164]. The 30 m delay line interferometer at Garching has achieved test mass differential position sensitivity of 2.5×10^{-18} m Hz$^{-\frac{1}{2}}$ dominated by shot noise between 1 and 6 kHz. The 10 m Fabry–Perot interferometer at Glasgow has reached $\sim 7 \times 10^{-19}$ m Hz$^{-\frac{1}{2}}$ from 500 Hz to 3 kHz and is close to being limited by shot noise. The 40 m Fabry–Perot interferometer at CalTech has achieved its best displacement sensitivity of 3×10^{-19} m Hz$^{-\frac{1}{2}}$ near 450 Hz. The broadband noise background (neglecting the narrow peaks which can be removed by appropriate filtering of the data) between 300 and 1000 Hz gives a rms differential displacement of less than 10^{-17} m, corresponding to an rms gravitational strain noise level of 2×10^{-19} which is comparable to the sensitivity of current resonant-bar detectors.

In pursuit of increasing the interferometer sensitivity, several optical schemes have been invented. *Power recycling*, proposed by Drever [165], reuses the otherwise unused laser power from the interferometer bright fringe. The light is reflected back towards the beamsplitter, thus increasing the total light power entering the interferometer. *Dual recycling* proposed by Meers [166] allows both laser power and signal power to be recycled, thus increasing sensitivity at the expense of signal bandwidth. Various other schemes such as synchronous *recycling* [165], *detuned resonant recycling* [167], and *resonant sideband extraction* [168, 169] provide various advantages. In general, recycling schemes allow high power built-up in the interferometer arms (which may or may not contain optical cavities) to increase the sensitivity while controlling the signal sideband storage time to maintain detection bandwidth.

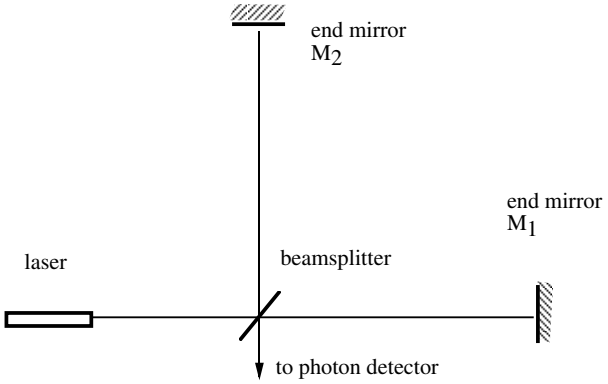

Figure 32. Simple Michelson interferometer.

Power recycling has been demonstrated on both tabletop [170–172] and suspended interferometers [173, 174] with success. Power recycling factors of 300 and 450 have been achieved [173, 174]. The broadband and tuned signal recycling has been demonstrated on tabletop by ANU group [175]. Dual recycling has been tested experimentally by both Glasgow [176] and Max Plank groups [177].

Long-baseline detectors are under construction at: Hanford, Washington and Livinston, Louisiana, USA (American LIGO project) [32], Pisa, Italy (3 km Italy/France VIRGO project) [178], Hannover, Germany (600 m British/Germany GEO project) [179] and Tokyo, Japan (300 m TAMA project) [180].

During the past few years the development of diode-pumped Nd:YAG lasers and ultralow-loss optical coatings has offered greatly improved performance in laser interferometer devices. Nd:YAG lasers are intrinsically stable and efficient. Low-loss coatings (for mirrors working in the infrared frequencies) offer very high recycling gain. Development of polishing techniques for sapphire means that improved material less susceptible to thermal lensing is becoming available. New ideas in suspension and isolation means that it appears likely that future interferometers need only be limited by fundamental limits, while there remains substantial room for future advances.

5.2. Configurations

5.2.1. Simple Michelson. A simple Michelson interferometer detector is shown schematically in figure 32. The interferometer consists of three 'free masses'—one beamsplitter, and two test masses at right angles to form the end mirrors. These masses are vibration isolated and suspended so that at frequencies well above resonance they can move freely as inertial test masses in the direction of the optical path of the interferometer in the frequency range of interest. When a gravitational wave passes it creates relative displacements of the test masses. The relative motion of the end mirrors is read out as intensity variations in the interferometer output, giving information about the incoming gravitational wave.

For simplicity, consider the case of an incident gravitational wave perpendicular to the plane of the interferometer with a polarization direction parallel to the interferometer arms. The passing wave will make one arm of the interferometer shorter and the other longer in half of the wave period, and reverse the contraction–elongation process in the other half-period. The relative change of optical length of the two arms $\Delta L = L_2 - L_1$ can be described as a

phase shift,

$$\Delta F = 2\pi \Delta L/\lambda. \tag{5.1}$$

This results in a change in the interference pattern at the output of the beamsplitter. The relative difference in optical path ΔL is proportional to the arm length $\Delta L = hL$. Generally, an interferometer is sensitive to a linear combination of the two polarization fields, and h in the above equation is

$$h = F_+ h_+ + F_\times h_\times \tag{5.2}$$

where F_+ and $F_\times$ are coefficients depending on the direction to the source and the orientation of the interferometer.

Because the gravitational signal is extremely small, it is very difficult to monitor the small time-varying changes in the interference pattern due to the passing gravitational wave. In practice, the phase difference arising from the optical arm length variations is obtained by the so-called 'nulling method'. The idea is to always keep the light returning from the two arms 180° out of phase so that its output is a dark 'fringe'. When the end mirrors are moved by the passing gravitational waves, the error signals applied to end mirrors to maintain the dark fringe contain the information of the gravitational wave signals. In this way the effect of power fluctuations in the laser beam can be minimized, and the shot noise level can be reduced.

Since the detection of gravitation waves with an interferometer is achieved by measuring the relative optical path (phase) change between the two arms, and since this path difference is proportional to the optical path L, it is clear that the size of the signal can be increased by lengthening the optical path of each arm. However, there is an optimum length $L_{\rm opt}$. At such a length the storage time of the light within the interferometer arms is equal to half the period of the gravitational wave. For arms longer than $L_{\rm opt}$, the gravitational wave signal will change sign during the light travelling time in the arm and the effect will partially cancel out. For example, for a gravitational wave signal of frequency $f_g \sim 1$ kHz, the optimum arm length is $L_{\rm opt} = c/(2f_g) = 150$ km. Such a long optical path length can be easily realized in a space-based interferometer (see section 3.2). In an Earth-based interferometer this is made possible by using multi-pass techniques. One such technique is the multi-pass Michelson interferometer in which an optical delay line [66] is inserted in each of the interferometer arms. The other is a Fabry–Perot Michelson interferometer [181] in which a second mirror is inserted in each arm to form a Fabry–Perot cavity.

5.2.2. Delay line Michelson interferometer. A delay line Michelson interferometer is shown schematically in figure 33. The two beams coming out of the beamsplitter are reflected many times between the beamsplitter and the end mirrors before they are recombined. For example, a 3 km long interferometer can have an optical length of 150 km by having 50 bounces. Apart from the restriction that the optical path length be shorter than $L_{\rm opt}$, the useful number of reflections is in practice limited by the reflection losses at the mirror.

A practical difficulty of the delay line Michelson interferometer configuration is the scattered light problem. The delay line uses a large number of beams zigzagging back and forth between mirrors. It is easy for light to scatter from the mirrors or from the side of vacuum pipes into the main beam at the photodetector. This scattered light could have a large phase difference $\alpha = 2\pi f \delta l/c$ with respect to the main beam, where f is the laser light frequency and δl is the path difference from the main beam. When the scattered light interferes with the main beam, it results in a phase shift β of the recombined light given by $\beta \sim a \sin\alpha$, where a is the fraction of the scattered light. This change of phase will be sensed by the output photodetector when combined with the beam from the other arm. It can be seen that any fluctuation of

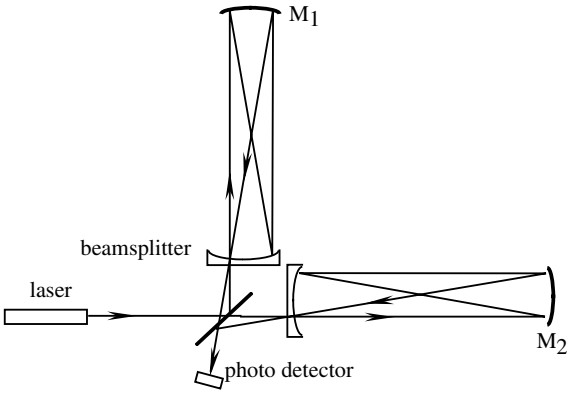

Figure 33. Schematic diagram of a delay line Michelson interferometer.

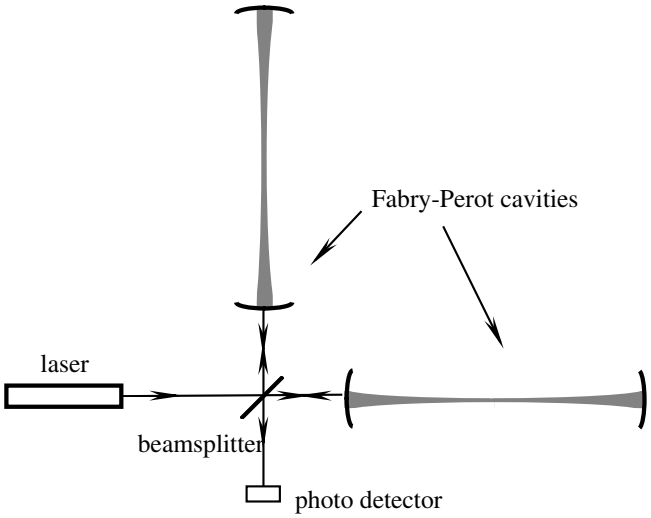

Figure 34. Schematic diagram of a Fabry–Perot cavity interferometer.

laser frequency or vibration of the vacuum pipes (which results in a change of δl) will cause a phase fluctuation of each beam, and thus a fluctuation in the final signal. This effect can be reduced by stabilizing the laser frequency. Modulation of the laser light [182] can improve the performance to some extent. This is done by changing the laser frequency f such that over a certain measurement time the scattered light phase difference α changes from 0–$2n\pi$. The average effect of the scattered light is then zero. This technique is limited by the dynamic range of the modulation. Another disadvantage of a delay line Michelson interferometer is that it needs large mirrors. However, excellent sensitivities of the order $h \sim 10^{-19}/\mathrm{Hz}^{1/2}$ have been obtained using a delay line Michelson interferometer of arm length 30 m [183].

5.2.3. Fabry–Perot cavity interferometer. The Fabry–Perot cavity interferometer gravitational wave detector was first introduced by Drever *et al* [181]. The idea is to add two additional mirrors near the beamsplitter, as shown in figure 34.

The near mirror and the end mirror in each arm form an optical cavity. Light travelling

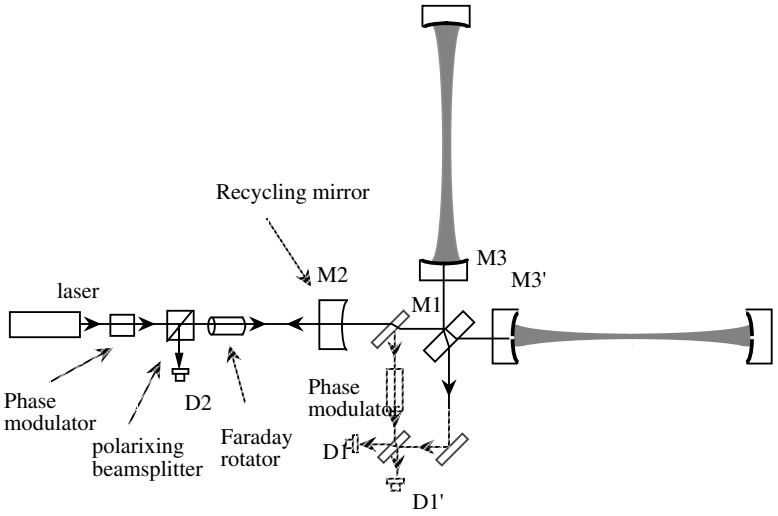

Figure 35. Basic arrangement of a Fabry–Perot interferometer system [324].

in one arm is reflected between the same pair of spots on the two mirrors, forming a sharp resonance. This Fabry–Perot cavity is very sensitive to the changes in cavity length, and to the change in frequency of the light. Because no laser has achieved the required stabilization level to directly detect the change in cavity length induced by gravitational waves, two cavities are needed to detect differential changes. The light from a single source passes through a beamsplitter and illuminates the cavities in the two arms of the interferometer. By looking at the differential phase change of the two arms, the effect of frequency fluctuations of the light source can be eliminated, and the signal is a measure of the passing of a gravitational wave. The size of the suppression of the laser frequency fluctuation noise depends on the balance of the two cavities. Typically, with a highly stabilized laser, the cavities must be balanced to one part in 10^3 or better.

Another approach is to lock the laser in wavelength to one of the cavities, and then to lock the second cavity to the laser wavelength. The locking signal of the second cavity then gives the relative cavity length change with respect to the first cavity, due to the passing gravitational wave. A practical arrangement of a Fabry–Perot cavity interferometer with such a readout system is shown in figure 35.

The Fabry–Perot cavity interferometer has the advantage of having smaller mirror size, and thus smaller vacuum pipe size, than that in a delay line Michelson interferometer. Also, the scattered light problem can be reduced greatly in a Fabry–Perot cavity arrangement because the scattered light is made to travel the same path as the main beam in the cavity.

5.2.4. Sagnac interferometer. A Sagnac interferometer is schematically shown in figure 36 in which light beams travelling in opposite directions experience common optical paths. With its common-path nature, the Sagnac interferometer is insensitive to a range of noise sources that affect other interferometers. Noise from low-frequency mirror displacements, laser frequency and intensity fluctuations, laser beam pointing fluctuations, thermally induced birefringence, and reflectivity asymmetry in the arms are all suppressed. This means that the Sagnac configuration can have a simplified control system and reduced optical tolerance requirements. Low-temporal-coherence illumination can be used in a common-path interferometer to reduce

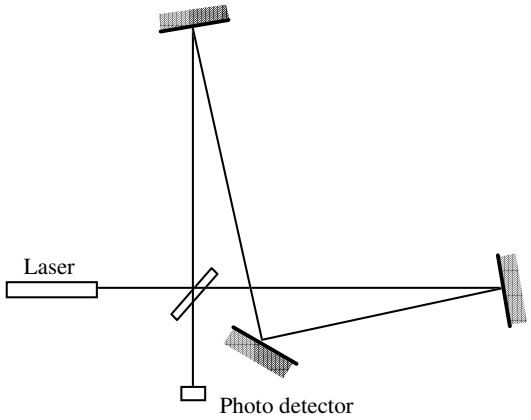

Figure 36. Schematic diagram of a Sagnac interferometer.

the noise caused by parasitic paths introduced by scattered light. In 1986, Weiss proposed an open-area Sagnac interferometer for gravitational wave detection. Recently, the zero-area Sagnac interferometer shown in figure 36 has been analysed and experimentally investigated as a topology for an advanced gravitational wave detector [184,185]. For 4-km 20-bounce (storage time of 0.53 ms) LIGO-scale interferometers illuminated with a 1064 nm Nd:YAG laser, the Sagnac interferometer has its first peak response at 690 Hz with 3 dB bandwidth from 220 to 1250 Hz [184], as shown in figure 37. Proper setting of the storage time allows the peak response frequency to be tuned to the gravitational wave band of interest. A shot-noise-limited phase sensitivity of 9×10^{-10} rad $\mathrm{Hz}^{-1/2}$ has been achieved on a tabletop Sagnac interferometer [185]. It has been demonstrated that precision phase measurement can be performed with a laser bearing a substantial amount of frequency and amplitude noise [185]. The Sagnac interferometer with resonant sideband extraction has been demonstrated on the tabletop [186].

The comparison between the Sagnac and Michelson interferometers is detailed by Mizuno [187] and colleagues. Their conclusion is that, once cavities are used either in the arms or for power- or signal-recycling, the advantages of the Sagnac interferometer over the Michelson interferometer disappear. Without power recycling, $\gg$1 kW laser with quite high stability is required to achieve the desired sensitivity for Sagnac interferometer.

5.2.5. All-reflective interferometer. Extremely high light power incident on the beamsplitter is needed to reduced the photon shot noise which is a major limiting factor in the high-frequency regime ($\sim$1 kHz) in laser interferometers. However, high light power poses problems for transmissive optics such as beamsplitters and the input/output mirrors of Fabry–Perot cavities, because there is always some optical absorption causing heating. The optical components are heated both by absorption in the substrate and in the reflective coatings. Heat from both regions leads to thermal lensing and birefringence in the substrate, and also to distortion of the optical surfaces. The Sagnac interferometer might alleviate these problems since the counterpropagating laser beams in principle share the same optical path.

A more certain method of reducing adverse thermal effects is to eliminate transmissive optical components completely. The losses in optical coatings are generally less than absorption losses, so by using reflective diffractive components instead of lenses and beamsplitters, it should in principle be possible to make interferometers much more tolerant of high optical powers. The idea of an entirely diffractive reflective interferometer has

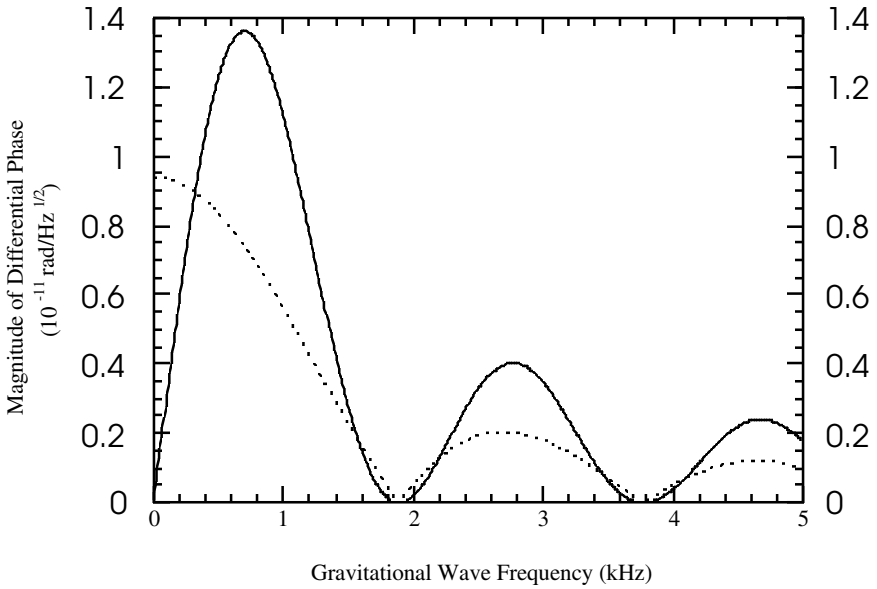

Figure 37. Theoretically calculated differential phase generated by a gravitational wave with strain $h_g \sim 10^{-23}/\sqrt{\text{Hz}}$, in a 20-bounce delay line, 4 km arm length Sagnac interferometer illuminated by a 1064 nm laser. The Michelson interferometer response (dotted curve) is shown for comparison [184].

been discussed by Drever [188]. The concept would allow test masses to be created using nontransmissive materials such as silicon or niobium, where low thermal noise did not have to be combined with excellent optical properties. One possible interferometer configuration using a diffractive beamsplitter is shown in figure 38. Veitch *et al* [189] have reported tests of a holographic beamsplitter used to remove optical aberrations and guarantee high fringe visibility and complete destructive interference at the interferometer output even in the presence of aberrations. An experimental demonstration of various grating beamsplitter tabletop interferometers (Michelson, Sagnac and Fabry–Perot) has been performed at Stanford [190]. For a practical diffractive interferometer it will be necessary to perfect reflective diffractive elements. If optical cavities are to be used, the mirror coatings will have to include a diffractive coupling beam. For example, a mirror may be required that has 99.999% reflection, and 0.001% coupling into a beam that leaves the mirror at a suitable angle. This problem sets a challenge for optics in the next decade, which can lead to major improvements in gravitational wave detection in the future.

5.3. Recycling

5.3.1. Power recycling. The sensitivity of an interferometer is ultimately limited by shot noise due to photon quantum statistics. The standard quantum limit for an interferometer can be obtained from the balance of two competing quantum noise sources as described by Caves [191, 192], Braginsky *et al* [112] and others. The first is the photon-counting error due to $N^{1/2}$ fluctuations in the number of output photons from the interferometer. The second is the radiation-pressure error. This arises from the perturbations on the end mirrors produced by fluctuating radiation-pressure forces which also scale as $N^{1/2}$. As the input laser power P increases, the relative photon-counting error decreases as $N^{1/2}/N$, while the radiation-pressure

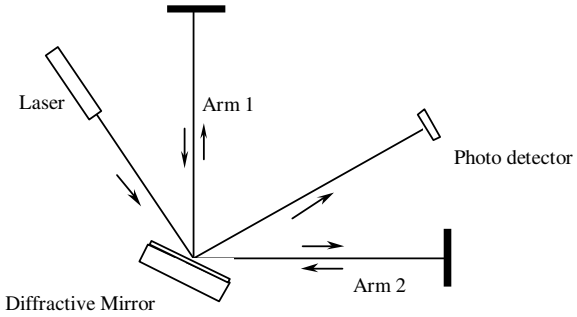

Figure 38. Schematic diagram of a Michelson interferometer based on the use of reflective diffraction grating as a beamsplitter.

error increases as $N^{1/2}$. Minimizing the total error with respect to P yields a minimum error of order of the standard quantum limit and an optimal input power for a simple Michelson interferometer,

$$P_{\text{opt}} = \frac{\lambda mc}{8\pi\tau^2\sqrt{\eta}}, \tag{5.3}$$

at which the minimum error can be achieved. Here, m is the mass of an end mirror, λ is the wavelength of the light, τ is the measurement duration, and c is the light velocity.

With a reasonable set of values for interferometer parameters, $m \sim 10^2$ kg, $\tau \sim 10^{-3}$ s, $\lambda \sim 1\ \mu$m, the optimum laser power P_{opt} is approximately 6×10^7 W—a power far higher than the power of present CW lasers. The low available input power means that the interferometer for use as gravitational wave detectors will be limited not by the standard quantum limit, but rather by photon-counting statistics (shot noise) which scales inversely to the square root of incident power at beamsplitter.

As mentioned above, the technique of power recycling [165, 166] can be used to increase the power incident at the beamsplitter and improve the sensitivity of interferometer detectors. The basic idea is that because the interferometer detector operates at a dark fringe output, almost all of the light (reduced only by losses in mirrors and beamsplitters) is reflected back towards the laser, and can therefore be used again as long as it is phase coherent with the input laser beam. This technique is realized by inserting a recycling mirror M_2 in between the laser and the beamsplitter as shown in figure 35. The position of the recycling mirror (or the laser frequency) is then carefully adjusted so that the recycling mirror combined with the two main cavities and the beamsplitter form a large resonant optical cavity containing the interferometer. By doing so, an effective laser power perhaps 1000-fold larger than the original laser may be built up inside this cavity, thus reducing the shot noise.

5.3.2. Resonant recycling. The resonant recycling technique [165] uses a mirror arrangement such that after each half gravitational wave period, the light in the two arms exchange arms instead of recombining at the output photodetector. In this way, the light of each beam always experiences phase shift in the same direction. The phase shift builds up during the total storage time over many gravitational wave cycles. In the end, a large phase difference between the two arms can be detected at the output of the interferometer. This technique can be used in both delay line Michelson interferometers and in Fabry–Perot interferometers. Figure 39 shows resonant recycling arrangements for both delay line interferometer and Fabry–Perot cavity interferometer.

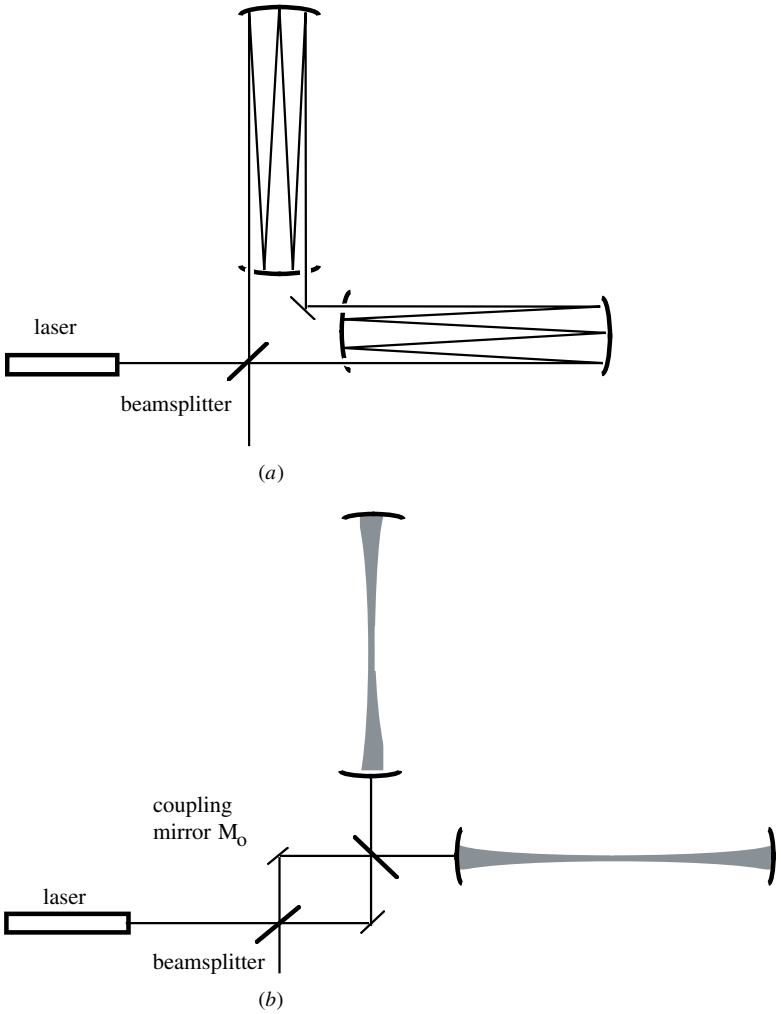

Figure 39. (*a*) Resonant recycling arrangement for a delay line interferometer. (*b*) Resonant recycling arrangement for a Fabry–Perot cavity interferometer.

In the case of resonant recycling in a Fabry–Perot cavity interferometer, it is considered that the two cavities are coupled through the high-reflectivity mirror M_0. This coupled system then has two modes of oscillation. The interferometer is tuned so that one of the modes of the coupled optical cavity system matches the frequency of the laser light and the other matches the frequency of the optical sideband produced by the motion of the end mirrors due to an incident gravitational wave. Both the laser light and the sideband signal produced by gravitational wave are enhanced at the output. In principle, resonant recycling gives better sensitivity for detecting periodic signals of known frequency. The total storage time is limited by the losses of the mirrors.

5.3.3. Dual recycling. A simple arrangement for dual recycling [193] is shown in figure 40. In addition to the power recycling mirror M_3, a new signal recycling mirror M_4 is placed at the output of the interferometer. Generally, the light at laser frequency (carrier) cannot

reach M_4 when the interferometer is locked on a dark fringe. However, when the gravitational wave arrives, it modulates the interferometer arm length difference and generate sidebands at frequencies offset from the laser frequency by the gravitational wave frequency. The sidebands leak from the interferometer output towards M4 as gravitational wave signal. So M_4 has no effect on the carrier but reflects the signal sidebands back to the interferometer. If we adjust the position of the mirror M_4 to allow the reflected signal sidebands and the signal in the interferometer arms to be in phase, the signal power (sensitivity) will be increased. The relative position of the recycling mirror M_4 determines the tuning frequency of the dual recycling. The bandwidth is determined by the reflectivity of the signal recycling mirror and the loss of the two arms. The dual recycling with tuning frequency at zero is called broadband dual recycling. The relative signal-to-noise ratio of a 3 km, 16-reflection delay line interferometer with different degrees of tuned dual recycling is shown in figure 41. The central frequencies are at 200 and 1000 Hz respectively. Even a relatively short arm interferometer can obtain impressive sensitivity. For example, figure 42 shows the predicted shot-noise-limited strain sensitivity of a 400 m, four-pass delay line [194]. The input power is 5 W. The tunned frequency is at 200 Hz. Curves (a) and(c) are based on application of recycling factors (450) already achieved in the laboratory [174], curves (b) and (d) employ somewhat higher factors.

5.3.4. Simple dual recycling instruments. The advantage of the Fabry–Perot Michelson interferometer is that high laser power and low mechanical noise requirements are predominantly restricted to optical cavities. Thus one needs only four very-high-performance components (the main Fabry–Perot mirrors) while the beamsplitter and other components are far less critical. When this scheme is extended to dual recycling as shown in figure 43. The interferometer consists of nested cavities, a pair of Fabry–Perot cavities within the overall power recycling and signal recycling cavities. This requires rather complex control systems.

A much simpler arrangement would be a four-pass dual recycling Michelson interferometer (GEO project) as illustrated in figure 43 [195]. Such a system utilizes only two cavities. Now, to regain the sensitivity of the Fabry–Perot Michelson, the interferometer must use high levels of power recycling, plus moderate signal recycling. Because of the thermal lensing problem [196], this arrangement requires excellent mechanical and optical performance of the beamsplitter.

It appears that very-low-loss silica beamsplitters may allow recycling factors up to 10^4 [197]. An alternative would be to use sapphire beamsplitters, which have intrinsic advantages associated with their high rigidity, and high thermal conductivity. However, the disadvantage of sapphire is its optical birefringence which requires control of the orientation of the crystal relative to the input and output beams.

5.3.5. Resonant sideband extraction. Resonant sideband extraction [168, 169] is a similar configuration to dual recycling for laser-interferometric gravitational wave detectors with Fabry–Perot cavities in the arms. This scheme reduces the thermal load on the beamsplitter and the coupling mirrors of the cavities and allows one to adapt the frequency response of the detector to a variety of requirements.

To obtain a good sensitivity in interferometric gravitational wave detectors one requires high light power in the arms of the interferometer to increase the photon shot-noise-limited signal-to-noise ratio. This can be done by increasing the finesses of the arm cavities. But since high finesse cavities have narrow bandwidth, (i.e. long optical storage time) this sets a limit to the detector bandwidth. The same power build-up can equally be obtained in principle by using power recycling to compensate for the limitation to the power enhancement in the

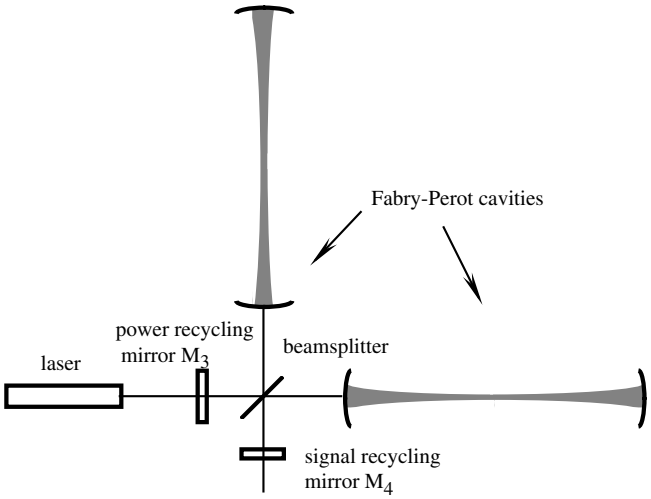

Figure 40. Dual recycling arrangement of an interferometer.

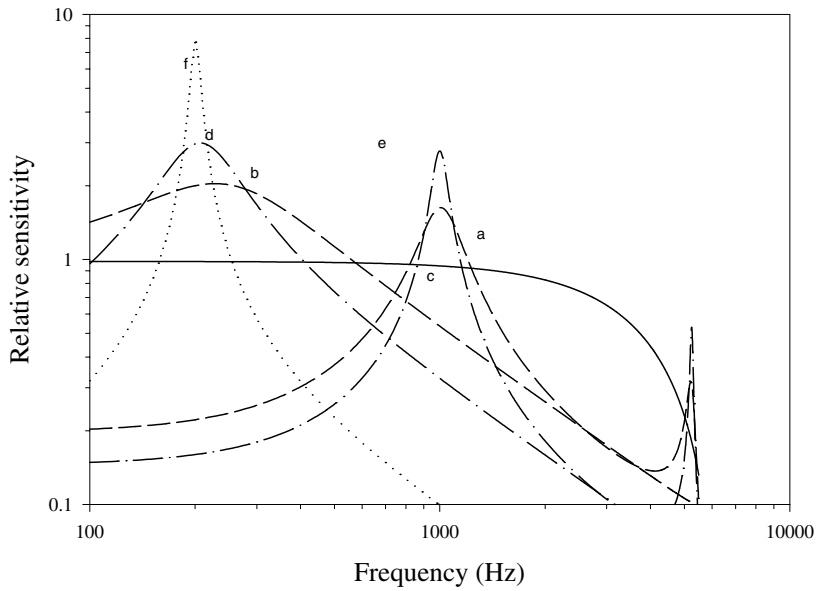

Figure 41. Relative signal-to-noise ratio of a 3 km 16-reflection delay line with different degrees of tuned dual recycling. The tuning frequencies are at 200 Hz and 1 kHz respectively. The vertical axis is in arbitrary units. The solid curve is for power recycling only; the dashed curve is for signal recycling mirror reflectivity, $R_s = 75\%$; the dash-dotted curve for $R_s = 90\%$; the dotted curve for $R_s = 99\%$ [325].

arm cavities. However, in practice the power recycling gain achievable is likely to be limited by imperfect contrast as well as losses in the beamsplitter and the coupling mirrors of the arm cavities. Furthermore, as already discussed, high power may induce thermal lensing and birefringence in the beamsplitter.

Resonant sideband extraction allows this dilemma to be avoided in an interferometer with

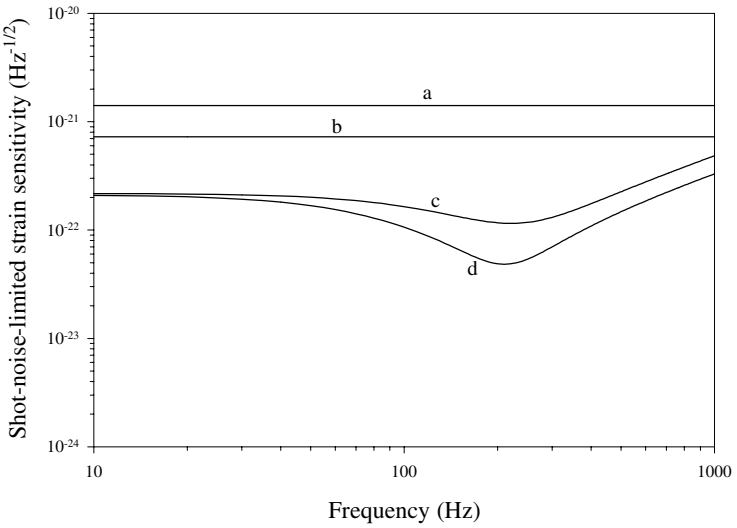

Figure 42. Frequency response of a 400 m interferometer. Input power is 5 W. Curve (*a*) power recycling factor of 450, no signal recycling; curve (*b*) power recycling factor of 1700; curve (*c*) dual recycling with power and signal recycling factors of 450; curve (*d*) power recycling factor of 1700, signal recycling factor of 800 [194].

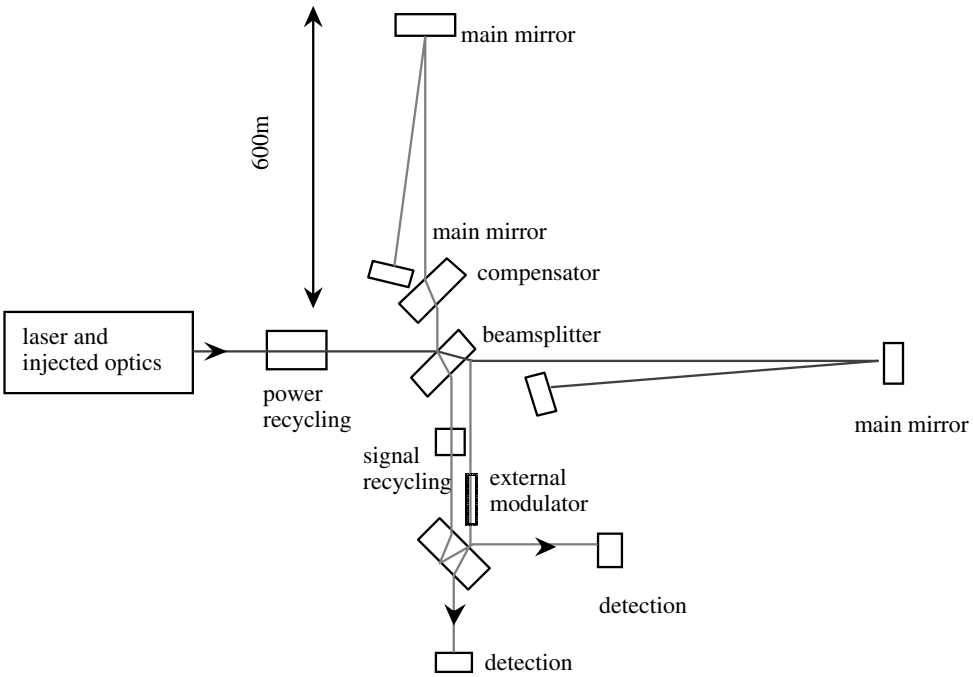

Figure 43. Schematic diagram of a four-pass delay line interferometer with both power and signal recycling (i.e. dual recycling). The angles and lengths are not to scale. The test masses of the interferometer are formed by the main mirrors and the beamsplitter [195].

arm cavities. The scheme resembles signal recycling, but uses a *signal extraction mirror* between the beamsplitter and the photo-detector. The purpose of this mirror is to *decrease* the storage time of the signal sidebands and therefore increase the detector bandwidth. This is achieved because the signal extraction mirror and arm cavities form a three-mirror-coupled cavity. Because the interferometer is locked to dark fringe the signal extraction mirror has no effect on the carrier. The signal extraction cavity formed by the signal extraction mirror and the coupling mirrors of the arm cavities forms a compound mirror which has frequency-dependent transmittance and reflectivity. Tuning the signal extraction cavity allows the transmittance for the signal frequencies of interest to be higher than that of arm cavities alone. For these frequencies the storage time in the three-mirror cavity is shorter than that in the unmodified arm cavity. In this case, the reduction of the storage time results in an increased detection bandwidth and unchanged high-finesse arm cavities for the carrier. In principle, the power enhancement in the arm cavities could be so great that no power recycling would be required. Yet the power passing through the beamsplitter and the coupling mirrors of the arm cavities could be low enough to have little thermal load. Figure 44 shows the frequency response of 3 km arm length interferometer with resonant sideband extraction configuration at various conditions [168].

5.4. Vibration isolation

At Earth-based sites for gravitational wave detectors, the ground is continuously vibrating with a rms amplitude of $x_s \approx \alpha f^{-2}$ m Hz$^{-\frac{1}{2}}$, where $\alpha \approx 10^{-6}$–10^{-9}. This is far greater than the signals we want to measure. Thus it is of great importance that terrestrial gravitational wave detectors, both resonant-bar and laser interferometers, are isolated from the seismic noise background. High-performance mechanical vibration isolation systems are required for this purpose. An ideal vibration isolator would not only cut out all significant seismic vibration in the pass band of the gravitational wave detector, but also cut out the seismic noise at much lower frequencies, so that the suspended test masses were effectively stationary with respect to the laser light field. If the total rms motion were much less than an optical fringe width, the servo control requirements would be minimized: components would be as stable as if rigidly attached to an optical table, or placed in interplanetary space. Operation of an interferometer would then be very simple. We show below that total rms motion from all frequencies above 0.2 Hz can in principle be reduced to about 1 nm.

This ideal level of isolation has not yet been achieved but there are various approaches that when combined, should approach the ideal performance discussed above. We subdivide the approaches to this problem under the headings passive isolation, active isolation and pre-isolation.

5.4.1. Passive mechanical isolation. Passive mechanical vibration isolators are mass–spring low-pass filters. For a multistage isolator, each stage of the isolator with resonant frequency f_0 will attenuate vibration by a factor $(f_0/f)^2$ at frequencies $f \gg f_0$. The total attenuation of the multistage isolator at frequencies above the *corner frequency* (the highest normal mode frequency of the isolator) is $(f_1 f_2 \ldots f_N/f^N)^2$, where N is the number of stages.

Figure 45 shows the typical behaviour of such an isolator. The figure shows a typical transfer function of a five-stage isolator with $f_0 = 2$ Hz. Below the corner frequency the normal modes amplify the seismic noise, while above it the isolation improves as the tenth power of the frequency ratio.

Traditionally, vibration isolators for gravitational wave detectors were based on industrial vibration isolators, using systems such as alternating layers of lead (or steel) and rubber [5].

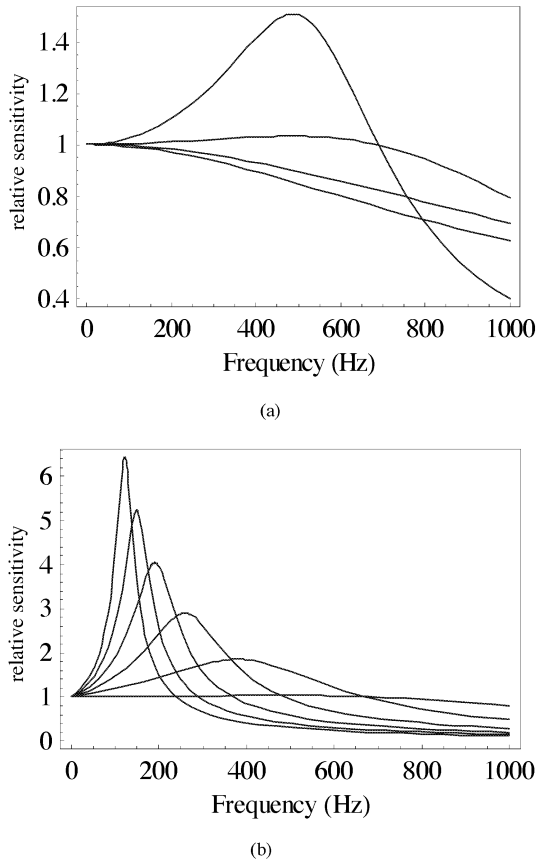

Figure 44. Typical frequency response of a 3 km arm length interferometer with resonant sideband extraction configuration. (*a*) Dependence of the frequency response on the length of the sideband extraction cavity (SEC) when the carrier is resonant in SEC. The curves, in order of increasing response at 400 Hz, are for SEC length of 1 m, 30 m, 100 m, 300 m. (*b*) Dependence on the tuning of SEC to carrier. The broadest response corresponds to the carrier resonant in SEC, and the others are detuned from it (carrier resonant condition). The length of SEC is 100 m, and detuning is by steps $2\pi/1000$. In both figures, the vertical units are arbitrary [168].

Isolators of this type have been used for room temperature vibration isolation in both resonant-mass gravitational wave detectors and prototype laser interferometer detectors. The disadvantage of these isolators is that they are not suitable for use in high vacuum (unless the rubber is outgassed or packaged in metal bellows); moreover, they are not suitable for uses at low temperatures where elastomer materials harden. In addition, this type of isolator generally shows large temperature coefficients and drift, due to the properties of the rubber, as well as having a relatively high corner frequency, limited by the compressive yield of the elastic elements.

Ideally, a multistage pendulum could be used to provide sufficient horizontal isolation for a laser interferometer gravitational wave antenna. Several groups have used double or triple pendulum suspensions combined with rubber and steel isolation stacks [198–201]. However, the curvature of the Earth creates intrinsic cross-coupling between the horizontal and vertical directions, due to the fact that the laser beam in an interferometer can only be perpendicular to the local vertical at one location. In a large-scale laser interferometer detector, the magnitude

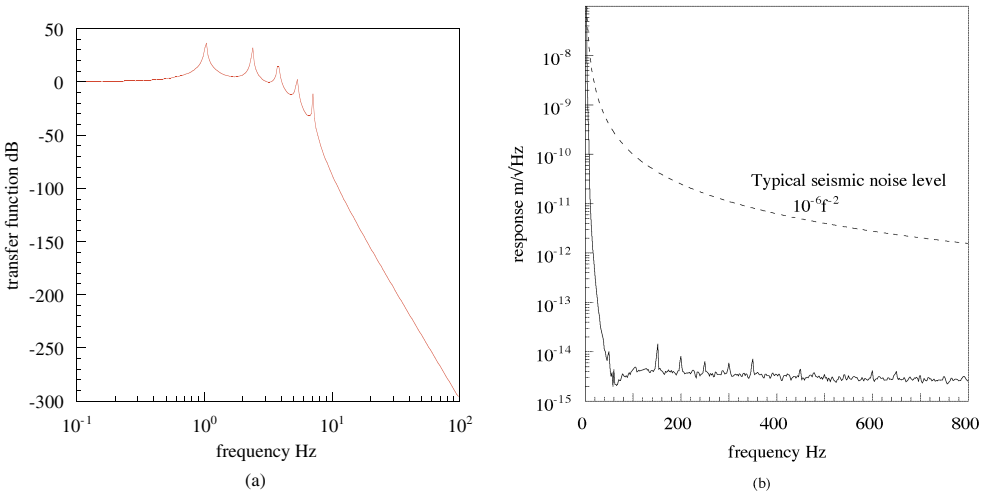

Figure 45. (*a*) Theoretical transfer function of a five-stage vibration isolator. Each stage has a natural frequency of 2 Hz. (*b*) Experimental upper limit of performance of a five-stage isolator [326], with a typical seismic curve of $10^{-6} f^{-2}$. At high frequencies the isolation reaches the noise floor of the sensing transducer of 3×10^{-15} m Hz$^{-1/2}$. Below 58 H the mechanical resonant frequency of the transducer, the sensitivity of the transducer degraded. Practically all the data above 50 Hz are transducer noise.

of the cross-coupling in ideal circumstances is $\sim 10^{-3}$. In real isolators the cross-coupling is likely to be degraded by mechanical imperfections. Thus it is important that the vertical vibration isolation should also be very high. The isolators must also be strong enough to support a total weight $\sim 10^2$–10^3 kg.

In interferometer antennas, the corner frequency needs to be pushed as low as possible to create the broadest possible bandwidth for observations. There is a great advantage in operating an interferometer antenna at the lowest possible frequencies. Not only does it extend the range of sources accessible to the detector, but for specific sources such as binary neutron star coalescence events, it increases the number of cycles of the coalescence that can be observed, thus allowing the signal-to-noise ratio to be increased. Giazotto pioneered the development of low-frequency vibration isolation. A very-large-scale multistage low-frequency superattenuator based on a gas spring was developed at Pisa [202, 203]. It had a high load-bearing capacity and a corner frequency of 2–3 Hz. However, gas springs have strong temperature coefficients, and so such isolators have problems of thermal stability and complexity. At the University of Western Australia, tapered metal cantilever spring vibration isolators [118], were developed, which showed excellent performance but somewhat higher corner frequency. The Pisa group replaced gas springs with similar tapered cantilevers and reduced the mechanical frequencies by use of magnetic antisprings, created by using magnetic repulsion between like poles of permanent magnets. This allowed low-frequency behaviour similar to the gas spring system to be achieved [204].

5.4.2. Active isolation. Active isolation techniques have been investigated extensively in gravitational wave research [205–210]. The basic idea is simple, as shown in figure 46: the relative displacement between the test mass to be isolated and the suspension point (the error signal) is sensed and fed back to an actuator to servo the suspension platform so that the motion of suspension point follows the motion of the test mass. In this way, the motion of the

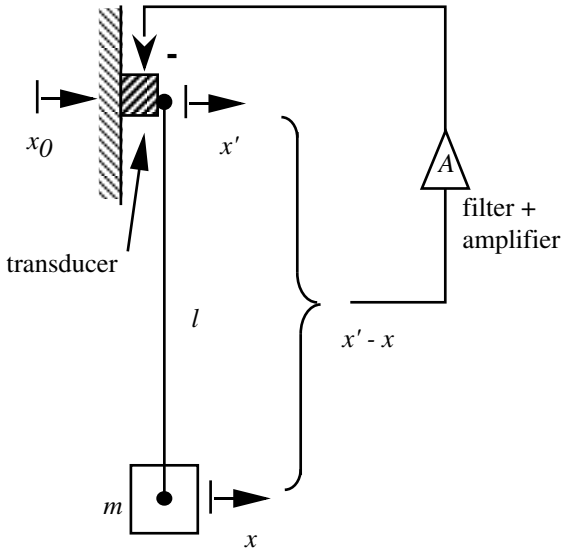

Figure 46. Schematic diagram of an active pendulum [205].

suspension platform is reduced and hence the motion of the test mass. If we look at the simple case of figure 46, the equation of motion of the mass is (for simplicity we ignore the damping term)

$$\ddot{x} = \omega_0^2(x' - x_0), \qquad \omega_0^2 = \frac{g}{l}. \tag{5.4}$$

Assuming the error signal is fed back to the suspension point so that $x' = x_0 - A(x' - x)$, then the transfer function of the system is

$$\frac{x}{x_0} = \frac{\omega_0^2}{-\omega_2(1 + A) + \omega_0^2} = \frac{\omega_0^2/(1 + A)}{-\omega^2 + \omega_0^2/(1 + A)}. \tag{5.5}$$

It can be seen that this system behaves like a pendulum with an equivalent resonant frequency of $\omega_0/\sqrt{(1 + A)}$. At frequency $f \gg f_o$, the attenuation is $[f_o/f/(1 + A)]^2$ instead of $(f_o/f)^2$. This means that the isolation of mass m is improved by a factor of $(1 + A)$.

The basic arrangement for vertical active isolation is shown in figure 47. The final transfer function is slightly complex. However, from the block diagram (figure 48), it can be seen that

$$x = G'x', \qquad G' < 1, \tag{5.6}$$

$$x' = G[xo - H(x' - x)] \qquad G < 1, \tag{5.7}$$

where GG' is the passive transfer function of the system and H is the loop gain of the feedback. The closed loop transfer is then

$$\frac{x}{x_0} = \frac{GG}{1 + H(G' - G'G)}. \tag{5.8}$$

The performance of this active system is improved by a factor of $[1 + H(G' - G'G)]$. However, it is impractical to assume very large gain H to obtain high-performance isolation. There are several limitations. One is the presence of internal resonances of the isolation structure. At each resonance there will be a phase shift added to the loop transfer function which can make the servo unstable. To ensure stability, the gain of the servo should be within the limit that

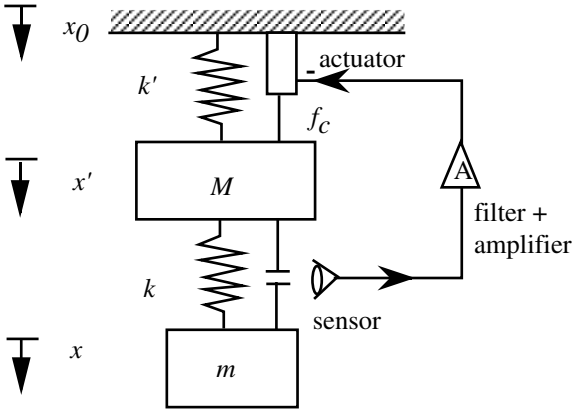

Figure 47. Schematic diagram of the active isolation model [206].

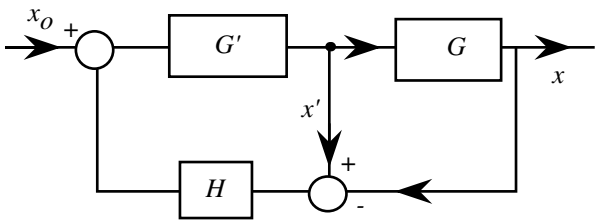

Figure 48. Block diagram of the active isolator [209].

all the internal resonant peaks are below unity gain. Another limitation is the noise in the sensor. This noise is treated the same by the servo system as the error signal between test mass and suspension platform. This noise will be amplified and fedback to the platform to create a displacement. At low frequency, where the attenuation of the test mass from the platform is not high, sensor noise plays an important role since the test mass tends to follow the movement of the platform.

5.4.3. Residual motion and the need for ultralow-frequency pre-isolation. A suspended test mass in a laser interferometer is required to be very precisely located to within $\leqslant 10^{-6}$ of an optical wavelength. Residual motion of the test mass in interferometers operated to date is typically ∼few microns. This has caused two problems. First, it makes it difficult to acquire lock, because very large forces must be applied to decelerate the test mass and locate it within operating range. Second, it makes it impossible to act directly on the test mass (by say a magnetic actuator) because the electronic noise of the actuator circuit is never less than 10^9 times smaller than the maximum signal which can be applied. (This is the dynamic range of a low-noise amplifier.) If the maximum signal is able to correct 10^{-6} m of motion, then the noise level will create noise motion just 10^9 times smaller, i.e. 10^{-15} m. This is unacceptably large.

There are two possible solutions to the problem. One is to create a more complex servo system and, in particular, to apply control forces to the stage above the test mass. All detectors constructed to date use this approach. The second possibility is to greatly reduce the residual motion.

Residual motion, and in particular residual accelerations, can be greatly reduced if a

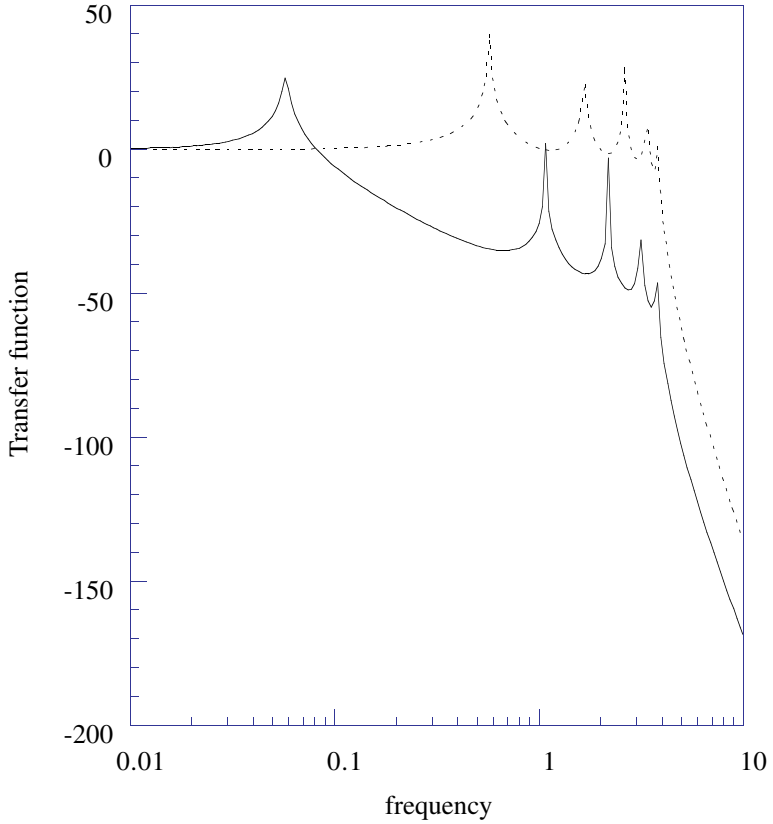

Figure 49. Comparison of transfer functions of a multistage isolator with and without an ultralow-frequency stage. Dotted curve: five-stage 2 Hz isolator, solid curve: four-stage 2 Hz isolator plus a 0.1 Hz ultralow-frequency pre-isolator.

conventional isolator is suspended by a pre-isolator with a much lower resonant frequency. This is illustrated in figure 49, where the addition of a single low-frequency stage reduces the amplitude of the normal mode peaks by about 50 dB. To realize this advantage requires the development of ultralow-frequency (ULF) mechanical suspension stages. As mentioned before, the isolation performance of an isolator with resonant frequency of f_o above the corner frequency is $(f_o/f)^2$. Thus the lower the resonant frequency f_o, the better isolation performance and the lower the corner frequency. This does not guarantee that with one or several ULF stages one can obtain very high isolation performance at high frequency. The problem is that internal mechanical resonances usually occur at frequencies that are typically about 10^2–10^3 times the fundamental resonant frequency of the mechanical resonant structures. Thus, for example, a stage with 10^{-1} Hz resonant frequency is likely to have an internal resonance from 100 Hz upwards and these will corrupt its isolation performance.

As a result, ULF stages are best used as pre-isolation stages in conjunction with low-frequency isolators. For an N-stage isolator, there are N normal mode peaks with amplitude up to 100 times the seismic background, depending on the Q-factor of the isolation elements. It is predominantly these normal modes which make it difficult to control and lock the interferometer. As discussed in section 5.4.1, different methods have been used to damp the normal modes, such as magnetic eddy current damping [200,211] and vibration absorber [212].

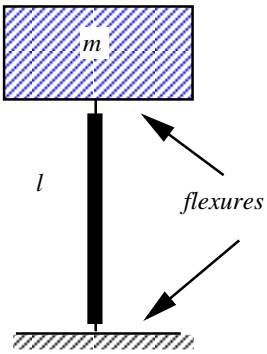

Figure 50. Simple model of an inverted pendulum.

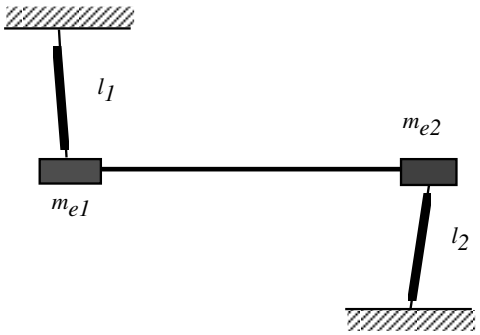

Figure 51. Simplified diagram of a folded pendulum.

A ULF-stage pre-isolator efficiently and passively reduces the normal mode amplitude as shown in figure 49. All the normal modes are on the cut-off slope of the ULF stage and are greatly reduced, leaving one very-low-frequency mode which is easy to control. This greatly simplifies the control system of the interferometer.

There are two main approaches to achieving very low frequency. One is to use a negative spring or antispring. A simple version is the inverted pendulum [213,214] as shown in figure 50. The resonant frequency of an inverted pendulum is given by

$$\omega_0 = \sqrt{\frac{k}{m} - \frac{g}{l}}, \tag{5.9}$$

where k is the spring constant of the flexure elements, m is the mass and l is the length of the inverted pendulum. Gravity provides a negative spring constant. The device has a low frequency when $g/l \sim k/m$, and it becomes unstable for $g/l > k/m$. Inverted pendulums for gravitational wave detectors were first investigated in UWA [213]. Because a mechanical Hooke's law spring is being used to counter a gravitational spring, and because the temperature coefficient of length differs from the temperature coefficient of Young's modulus, such antispring devices generally have relatively large temperature sensitivity. Thus servo control is needed to maintain a stable operating position. A full-scale inverted pendulum pre-isolation stage about 6 m high has been built for VIRGO's supperattanuator [215], and a 1 m stage has been developed at UWA [216].

For horizontal isolation, more elegant devices minimize the contribution of mechanical springs. One such device is the folded pendulum [217–219]. It combines a positive and negative pendulum as shown in figure 51. The resonant frequency of the folded pendulum is given as

$$\omega = \sqrt{\frac{1}{M_e}\left(\frac{m_{e1}g}{l_1} - \frac{m_{e2}g}{l_2}\right) + \gamma}, \tag{5.10}$$

where γ is a small additional term which takes into account elastic contributions from the flexures, $M_e = m_{e1} + m_{e2}$ is the equivalent mass of the pendulum and l_1, l_2 are the lengths of the positive and negative arm respectively. This device has low temperature sensitivity and has achieved a resonant frequency of 15 mHz [220]. With a resonant frequency of 17 mHz, this device gives isolation of more than 90 dB at 10 Hz. Above 15 Hz, the attenuation is degraded due to internal resonances of the isolator structure, as discussed above.

Another type of ULF stage is the X-pendulum [221, 222]. It uses two cross-wire linkage arrangements that mimic the motion of a very long pendulum. A resonant frequency of

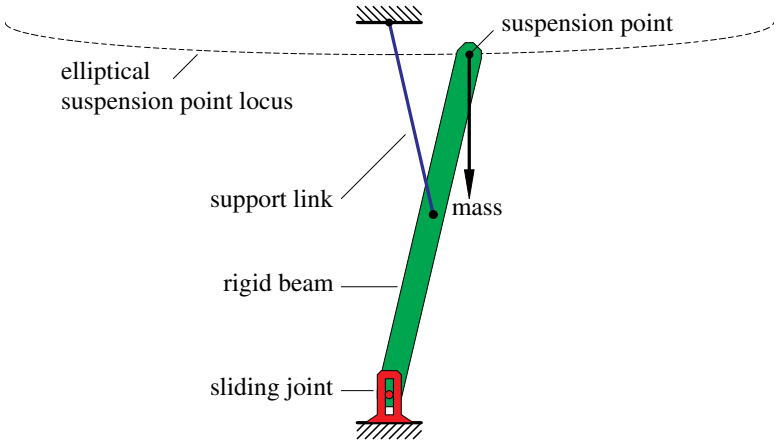

Figure 52. Scott–Russel linkage.

50 mHz has been demonstrated. With a resonant frequency of 0.21 Hz, the X-pendulum has demonstrated 30 dB isolation at 3 Hz. Above 3 Hz, the internal resonances dominate.

Both the folded pendulum and X-pendulum are most easily implemented as one-dimensional isolators. Although they can be cascaded to form a two-dimensional horizontal isolator, there are significant construction problems. Winterflood and Blair [223] have used the Scott–Russel linkage, shown schematically in figure 51. This device mimics the motion of a very long conical pendulum, achieving two-dimensional horizontal isolation in one single stage. A full-size prototype pre-isolator [224] has demonstrated a resonant frequency of 7 mHz and with a resonant frequency of 17 mHz, it achieves an isolation exceeding 75 dB at 0.5 Hz.

It is interesting to note that only one of the four horizontal stages discussed above is dependent on a carefully designed spring. This is the inverted pendulum, where a gravitational antispring balances on angular mechanical spring. In the other cases, mechanical springs are eliminated, except in so far as being an intrinsic, but small, component of a flexure suspension. All the linkage-based devices have the advantage that the temperature coefficients and nonlinearity of springs are minimized.

As mentioned above, cross-coupling requires a high level of isolation for both horizontal and vertical isolation. Thus there is little point in building an isolator with excellent horizontal pre-isolation unless it also has good vertical pre-isolation. Since the vertical isolation must always counteract a large gravitational force, it is almost impossible to avoid the use of large mechanical springs for vertical load bearing. However, several practical means of counteracting the spring constant have been demonstrated. The first is the magnetic antispring, demonstrated at Pisa [204, 225]. Pairs of magnets in a repulsive arrangement create a potential hill in the middle line of the magnet pairs. The negative spring constant represented by the potential hill partially cancels the positive spring constant, substantially reducing the total stiffness of the spring. Unfortunately, most magnets have high temperature coefficients, so that the magnetic antispring must be very carefully temperature controlled.

An alternation which avoids magnets is the geometric antispring. This was first demonstrated by LaCoste in his seismometer design [226], in which a zero length coil spring suspends a horizontal arm by acting on it at an angle (figure 53). The torsion crank linkage developed by Winterflood and Blair [224] uses a different geometrical antispring concept, as illustrated in figure 54. This design makes use of the nonlinearity produce by the torsion arm connected to a suspension link. It is arranged so that the effective spring constant

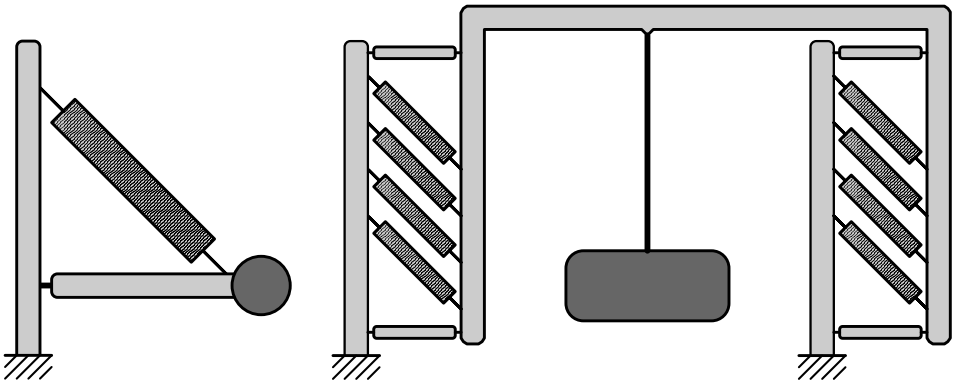

Figure 53. (*a*) LaCoste linkage. (*b*) Vertical preisolation using LaCoste linkage.

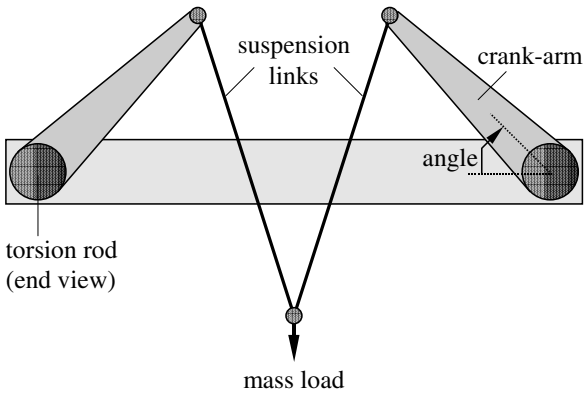

Figure 54. The torsion crank linkage arrangement [224].

$k = \partial_F/\partial_y (F = \text{force}, y = \text{vertical displacement})$ is almost zero and constant in a certain range. In a simple model, the torsion crank achieved a resonant frequency of 50 mHz. This vertical ULF stage can be combined with a Scott–Russel stage to create a three-dimensional pre-isolator as shown in figure 55.

De Salvo has demonstrated a geometric antispring based around a pair of cantilever blade springs [227]. The torsion rods of figure 54 are replaced by cantilever blades, and using appropriated angled suspension wires the same geometry effect causes nulling of the spring constant for a certain deflection angle.

Figure 56 shows the residual motion predicted for a passive isolator being developed at UWA [216]. This system utilizes passive eddy current damping, as well as seismic tilt control. The predicted performance is 10^{-9} m rms above 0.2 Hz. If such an isolator can be realized, interferometer operation will be greatly simplified.

5.5. Thermal noise

Once the seismic noise cut-off is lowered sufficiently through the use of high-performance vibration isolators, thermal noise will become the critical source of noise. From the fluctuation–

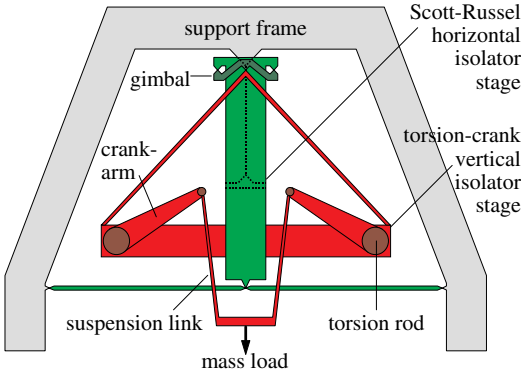

Figure 55. Three-dimensional pre-isolation stage, consisting of a torsion crank vertical stage and a Scott–Russel horizontal stage.

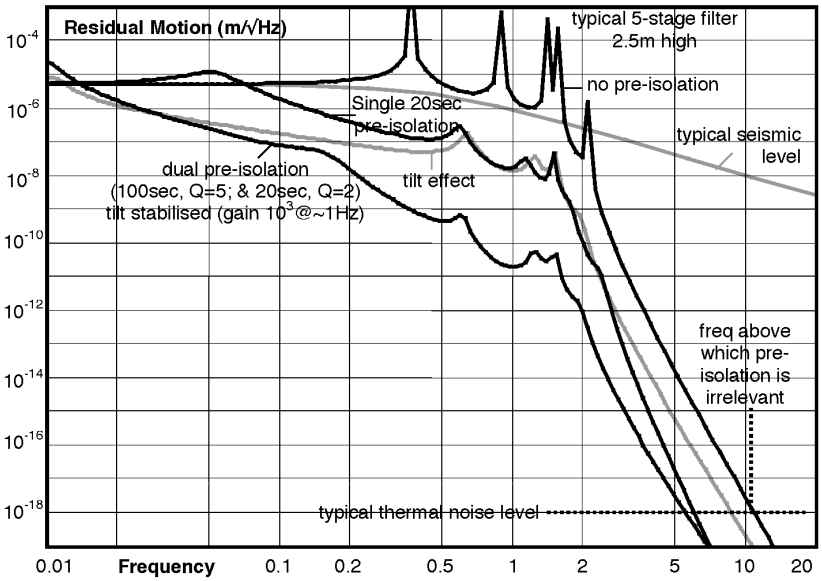

Figure 56. Successive reduction of residual motion. The bottom curve is the predicted overall isolation performance with pre-isolation stage, eddy current damping and tilt control.

dissipation theorem [90] the general power spectrum of the minimal fluctuation force is

$$F_{\mathrm{th}}^2 = 4k_{\mathrm{B}}TR(\omega), \tag{5.11}$$

where k_{B} is the Boltzmann constant and $R(\omega)$ is the real part of the impedance of the system. Using $Z = F/v$, the above equation can be expressed as

$$x_{\mathrm{th}}^2 = \frac{4k_{\mathrm{B}}T\sigma(\omega)}{\omega}. \tag{5.12}$$

$\sigma(\omega)$ is the real part of the admittance $Y(\omega) = 1/Z(\omega)$. For a simple harmonic motion system with spring constant k, mass m and a damping r, the thermal noise displacement power spectrum is [228]

$$x_{\mathrm{th}}^2 = \frac{4k_{\mathrm{B}}Tr}{(k - m\omega^2)^2 + r^2\omega^2}. \tag{5.13}$$

If a damping mechanism of structural damping is assumed, which can be described with a complex modulus of elasticity [229], $k = k_0[1+\mathrm{i}\varphi]$, $\varphi =$ constant (i.e. $r = k\varphi$), equation (5.18) becomes

$$x_{\mathrm{th}}^2 = \frac{4k_{\mathrm{B}}Tk\varphi}{\omega[(k - m\omega^2)^2 + k^2\varphi^2]} = \frac{4k_{\mathrm{B}}T\omega_0\varphi}{\omega m[(1 - \frac{\omega^2}{\omega_0^2})^2 + \varphi^2]}, \tag{5.14}$$

where $\omega_0 = \sqrt{\frac{k}{m}}$ is the angular resonant frequency.

In a laser interferometer gravitational wave detector, thermal noise is mainly divided into two classes—the suspension thermal noise and the internal thermal noise of the test mass.

5.5.1. Suspension thermal noise and Q-factor of the pendulum. Suspension thermal noise is mainly the Nyquist noise of the test mass pendulum of the interferometer. The Q-factor of a pendulum suspension can in principle be very high because the energy storage is predominantly in the effectively loss-less gravitational field. However, some elastic energy must always be stored in the flexure which supports the pendulum. The Q-factor of a pendulum is limited by the losses in this element. The Brownian motion noise amplitude of a simple pendulum at angular frequency ω, for any normal mode at frequency $\omega_p \ll \omega$ is given by

$$x_p^2(\omega) = \frac{4k_{\mathrm{B}}T\omega_{p^2}}{Q_p m\omega^5}. \tag{5.15}$$

The Q-factor of the pendulum is given by $Q_p = \gamma Q_0$, where $Q_0 = 1/\varphi$ is the intrinsic Q-factor of the flexure material, and γ is the enhancement factor, which depends on the geometry and material of the pendulum flexure [228, 230].

Applying equation (5.20) to a simple pendulum, it has been shown that the thermal noise in a simple pendulum scales as [228]

$$x_{\mathrm{th}}^2 \propto m^{1/2}. \tag{5.16}$$

It can be seen that the suspension thermal noise can be reduced by increasing the mass of the pendulum and the quality factor of the test mass pendulum stage. To obtain numerical estimates, consider a typical interferometer with parameters of $L = 3$ km, $T = 300$ K, $m = 30$ kg, $f_p = \omega_p/2\pi = 1$ Hz, and $Q_p = 10^9$. We then have

$$h = \frac{x}{L} \sim 10^{-21}\left(\frac{10\ \mathrm{Hz}}{f}\right)^{5/2} \Big/ \sqrt{\mathrm{Hz}}. \tag{5.17}$$

This shows that extremely-low-loss pendulums are essential. For example, to obtain the sensitivity goals of $10^{-23}/\sqrt{\mathrm{Hz}}$ at 10 Hz, a pendulum Q-factor of 10^{10} is required.

At current sensitivity levels, it is barely possible to measure directly the thermal noise floor for high Q-factor test masses over the frequency range of interest for gravitational wave detectors. The thermal noise has to be inferred from Q-factor measurement of some resonance at other frequencies. However, the Q-factor and frequency relation is model dependent, and the calculated thermal noise floor differs with different damping mechanism assumptions. Frequency-independent Q-factors over a large frequency range have been approximately confirmed in some materials [214, 231–234]. The mechanism of structural damping is now widely accepted. However, it still needs more investigation, particularly to confirm the phenomenon in low-loss single-crystal materials.

Various types of suspension have been studied to obtain a high pendulum Q-factor. Most researchers have assumed that wires are necessary. Suspensions with a thin wire double-loop simple pendulum configuration are widely used [199, 200, 235–237]. A pendulum Q-factor of

$Q \sim 10^8$ with wire suspension is expected [238], assuming reasonable Q-factors for the wires. Pendulum Q-factors exceed 10^7 had been observed with fused silica fibre suspension [239]. The highest pendulum Q-factor reported so far is $>3 \times 10^8$ by Braginsky *et al* [240] with a monolithic silica fibre and a 30 g mass.

The simple pendulum suspension system inevitably will have a set of middle-frequency violin string modes from the suspension wire. Those modes will contaminate the window of gravitational wave detection. The problem of the thermal noise of pendulums suspended by wires has been intensively studied [232–234, 241–243]. Studies have shown that high pendulum Q-factor is related to a high violin string mode Q-factor. So each violin string mode is confined within a very narrow frequency band.

Theoretical analysis has shown that significant improvements can be achieved if the pendulum is replaced by a compound pendulum supported by a thin membrane which acts as a hinge [230]. A pendulum with hinge suspension has been shown to achieve $Q \sim 10^7$ [244]. Using known high-Q materials such as niobium which has a Q-factor $\sim 10^5$ in thin membrane, and assuming that Q is independent of frequency, it can be shown that Q-factors exceeding 10^7 [245] can be expected. Also, since the test mass pendulum is suspended by a very short membrane, the violin string mode will be high enough to be neglected. The membrane flexure can be made much thinner than the wire flexure and thus has lower thermoelastic effect.

5.5.2. Test mass internal resonance thermal noise. The test mass will have many internal resonances. The total thermal noise thermal noise spectral density can be expressed as [228]

$$x_{\mathrm{th}}^2 = \frac{4k_{\mathrm{B}}T}{\omega} \sum_i \frac{\omega_i^2 \varphi_i}{m_i[(\omega_i^2 - \omega^2)^2 + \omega_i^4 \varphi_i^2]}. \tag{5.18}$$

Here i is the index of the ith mode, m_i is the effective of ith mode and $\varphi_i = 1/Q_i$, where Q_i is the quality factor of the ith mode. Typical internal resonances of a test mass are at about several kilohertz. The thermal noise spectral density far below the internal resonant frequency $\omega \ll \omega_i$ (assuming loss factor $\varphi_i = \varphi =$ constant) is given by

$$x_{\mathrm{th}}^2 \frac{4k_{\mathrm{B}}T\varphi}{\omega} \sum_i \frac{1}{m_i \omega_i^2}. \tag{5.19}$$

Although it can be seen from the above equation that the lowest internal resonance contributes most to the thermal noise, detailed theoretical studies [246, 247] has shown that higher-order modes cannot be neglected, especially when the laser beam is not perfectly aligned.

From equation (5.19) it can be seen that to reduce internal thermal noise it is required that the test masses have high internal resonances and very high Q-factors $(1/\varphi)$. Since ω_i is proportional to the velocity of sound, high sound velocity materials are required. It is worthwhile pointing out that the dimensions of the test mass should not be too large so as to keep the frequency of internal resonances as high as possible. This is contradictory to the requirement of using a big test mass to reduce the pendulum thermal noise. There is a compromise in choosing the size and mass of the test mass. High Q-factor materials (such as quartz and silicon) have been investigated in prototype laser interferometer detectors [248]. At present, fused silica test masses are widely used in prototype interferometer detectors. The Q-factor of silica test masses were observed to be of the order of 10^6 [249, 250] with a higher value of $>10^7$ in some resonant modes recently observed by Beilby and Startin [251]. The highest Q-factor of silica was reported by Braginsky of 6×10^7 [252].

Using another high Q-factor material, sapphire, as test mass has been proposed [230]. The excellent thermal and mechanical properties of sapphire makes it a promising material for use in test masses. Compared with silica material, the high thermal conductivity means the thermal

lensing problem can be minimized, while the very high Young's modulus means the internal resonance will be high. The highest reported sapphire Q-factor is 4×10^8 by Braginsky [112] and recent measurements reported a reproducible result of $2–3 \times 10^8$ Q-factors [239, 253]. Theoretical analysis [254] suggests that the thermal noise can improve by a factor of >10 by using sapphire test mass instead of silica test masses.

In practice, the suspension joint to the test mass plays an important role in obtaining both high-Q pendulum motion and high internal Q-resonance. Monolithic suspension systems have been suggested and investigated. These include bonding the silica fibre to the silica test mass using silicate bonding method [255], and bonding niobium flexure to sapphire test mass using active alloy bonding [256] and possibly silicate bonding [257].

5.6. Control systems

As mentioned above, the test masses in the interferometer must be suspended to isolate against seismic and environmental vibration. To achieve operation of an interferometer a feedback system must be used control the test mass position to high precision. Firstly, a local control system is necessary to suppress large-scale motions and align the mirrors to the point where the best interference contrast may be achieved. Secondly, to allow maximum sensitivity, a global control system is required to control the interferometer arm lengths to a relative motion of $\sim 10^{-12}$ m rms [183]. This is achieved by locking the interferometer to a dark fringe.

5.6.1. Local controls. Various damping methods to suppress low-frequency normal mode in vibration isolators have been investigated. Passive damping such as magnetic eddy current damping has been investigated [200, 211]. The problem with this type of damping is that the damping is usually relative to a support structure and can introduce noise into the isolators both through seismic noise and resonant peaks of the support structure. This degrades the high-frequency performance of the isolator.

An alternative method of magnetic damping uses the narrow-band resonant absorber. In this case, individual modes of an isolator can be damped using a tuned resonator which is itself magnetically damped.

The low-frequency normal modes can also be attenuated by active damping [162, 199, 258–261]. A correction force corresponding to the motion of the suspended masses (measured by an inertial or non-inertial sensor) is applied to the appropriate part of the suspension system. A non-inertial sensor such as shadow sensor [162] is widely used on prototype interferometers [162, 163]. It consists of a small vane mounted on the sensed surface, a light-emitting diode (LED) and an opposing photodiode (PD) mounted on the reference surface. The vane is free to move between the LED and PD and develops a signal proportional to the displacement of the vane by partially interrupting the light. The correction forces are applied by a small permanent magnet mounted integrally with the vane, and a coil mounted on the reference surface. The reference surface is usually the support frame, which is attached to the ground. Then the problem arises that the seismic noise can be injected into the servo loop both in sensing and in force actuation. If motion sensing is done with respect to the frame, it is impossible to avoid seismic noise in the sensing. This sensing noise has components in the signal band which must be prevented from driving the test mass and appearing in the signal output. This is readily achieved by electronic filtering of the signal [162, 260]. The noise injection through the coil can be overcome by carefully positioning the coil so that the magnetic field gradient is maximized at the magnet. This results in the best decoupling of the forces applied on the controlled masses [162]. Another way to overcome frame vibration is to use two coils to linearize the field and create a magnetic force which is independent of the position and motion

of the frame [260]. If the reference surface is a reaction mass [262] which is well isolated from the seismic noise, the noise injection will not be such a problem. However, such a sensor will not damp the common-mode motion of the test and reference masses. An inertial sensor such as a mass-loaded piezoelectric accelerometer [263] or a wideband accelerometer [264, 265] can in principle avoid the problem of sensing frame vibrations. Inertial sensing avoids any coupling with seismic noise. Its ultimate sensitivity is set by electronics noise, thermal noise and thermal drifts of the accelerometer and the feedback actuators.

Another kind of non-inertial sensor is the capacitance transducer [266]. A convenient implementation for use on dielectric test mass surfaces consists of two interleaving combs of parallel conductors etched onto a circuit board. The dielectric constant of the sensed surface contributes to the capacitance between the combs. A voltage applied to the capacitor will exert a force on the test mass, while motion of the test mass modulates the capacitance. Thus this system can provide both sensing and feedback forces. There is no need for lossy magnets or vanes to be attached to the test mass, so the test mass acoustic losses need not be degraded [249].

5.6.2. Global controls. It is necessary to extract error signals to control the interferometer lengths or mirror positions to lock the output at the dark fringe and the recycling cavity or arm cavities on resonant with the laser frequency. In order to avoid the noise due to the laser power fluctuations and $1/f$ electronics noise at low frequencies, the measurement has to be shifted to the quieter MHz domain using modulation–demodulation techniques. Various modulation configurations have been proposed and extensively studied. Schemes known as external [176, 267–269] and frontal [270–274] modulation have been particularly investigated because their modulators are outside the interferometer. Thus, as opposed to internal modulation, these schemes avoid introducing losses or wavefront distortion within the interferometer [275]. Although quantum-noise-limited sensitivity has been achieved with internal modulation at low laser power level [276–278], all the proposed large-scale laser interferometer detectors will not use this configuration because it introduces losses and wavefront distortion.

In the external modulation configuration (figure 36), a reference beam from the antireflective coated face of the beamsplitter is extracted, phase modulated and mixed with the main interference as in a Mach–Zehnder interferometer. This configuration needs additional optical components that, in order to avoid noise, must be suspended. The length of the reference Mach–Zehnder arm must be controlled to maximize the phase sensitivity. The modulation index m in the external arm is an independent variable and can be set to maximize $J_1(m)$ when m reaches its optimum value of 1.84 radians. A larger modulation index leads to more power being transferred to higher-order sidebands, which are normally not utilized by the demodulation process. Furthermore, in power-recycling and arm-cavity configurations, another modulation is needed to extract error signals to control the recycling mirror and arm cavities. Because the arm lengths of the interferometer can be equal and because the reference beam extracted from the back face of the beamsplitter has travelled almost the same path length as the main beam, this configuration is insensitive to the laser frequency noise.

In the frontal modulation configuration (figure 57) the interferometer has two arms with a small difference in length. The laser beam is phase modulated before entering the interferometer. The laser field at the interferometer input may be expressed as a superposition of three monochromatic plane waves if the modulation index is not too high: the carrier with the original laser frequency and two sidebands with the frequency shift of the modulation frequency f_m. In the simple Michelson, when the dark fringe condition is fulfilled for the carrier, the sidebands transmitted to the interferometer are maximum when arm length difference is a quarter of the modulation wavelength, $c/4f_m$.

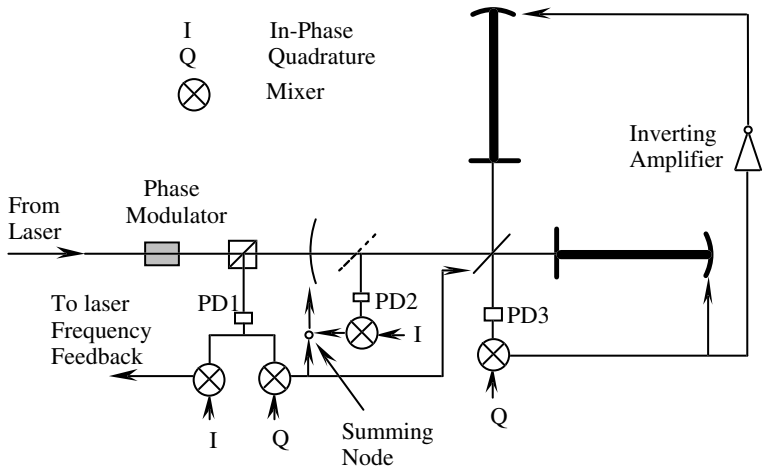

Figure 57. Global control configuration with frontal modulation [272].

If a recycling mirror is added, the modulation frequency and arm length difference must fulfil two conditions. First, the sidebands must resonant in the recycling cavity, otherwise the effective modulation index will be very small. Second, the signal must have maximum phase sensitivity. If R_r and R_m are respectively the intensity reflectivity of the recycling mirror and the interferometer, the modulation frequency f_m and the arm length difference Δl have to satisfy the following condition [273]:

$$\cos\left(2\pi f_m \frac{\Delta l}{c}\right) = \sqrt{R_r R_m}. \tag{5.20}$$

This condition also ensures the optimum enhancement of the modulation index inside the recycling cavity.

Even with cavities in two arms, one modulator is enough to get all the error signals to control each mirror. This configuration is simple and rather easy to realize. But because of the nonsymmetric configuration, the interferometer is sensitive to laser frequency and beam jitter noise. Frontal modulation was first demonstrated by successfully locking a tabletop prototype of a power-recycled Michelson interferometer with Fabry–Perot cavities in the arms [272].

5.6.3. Analogue and digital controls. Implementing the control discussed above can be achieved by either analogue or digital control systems. Analogue control is a well developed technology. Conventional PID servo control techniques can be used. Most prototype interferometers use analogue control for local damping, alignment and fringe locking [279]. The results have been successful, with sensitivity of 3×10^{-19} m Hz$^{-1/2}$ achieved [164] and generally not limited by servo system noise. However, for large-scale interferometers like LIGO and VIRGO, there are a large number of degrees of freedom (more than 200) [280] which need to be controlled and many of them are coupled each other. It is also planned that many error signals will be monitored and archived, to allow cross-correlation with the signal from the interferometer output PD. Many automated features are also required. All of the above points incline towards the use of digital control systems. Since Barone *et al* [281] introduced the idea of digital control into the automatic alignment of a Michelson interferometer, they have demonstrated theoretically and experimentally that all the specification on the noise requirements, the dynamic range and the control bandwidth can be satisfied using all-

digital control systems [282]. A fully digitally controlled interferometer prototype has been successfully operated in Naples, Italy for development and test of some VIRGO subsystems.

Heflin and Kawashima [283, 284] implemented both analogue and digital alignment control for the TENKO-100 DL interferometer. The results indicate that digital feedback control for application onto interferometer systems with target search frequency $\sim$1 kHz or less is a feasible alternative to analogue feedback systems. It has been shown to reproduce many of the same desirable features as the analogue systems.

Improved vibration isolation, especially that with very low residual motion, is likely to allow the undoubted complexity of the control problems discussed above to be substantially simplified.

5.7. Laser stabilization

Laser interferometers are designed to be sensitive to the optical phase difference of two arms, and should not be sensitive to common-mode fluctuations of the input light. But in practice, because of asymmetry between the two arms, fluctuations in the input light will couple into the output signal. In the frontal modulation scheme some asymmetry is unavoidable. In addition, differences in the optical components will cause, for example, intensity fluctuations to give rise to a differential radiation pressure force between both arms. Thus, laser intensity and frequency fluctuations must be strongly suppressed.

5.7.1. Laser pre-stabilization. The laser frequency noise Δf can couple into interferometer phase fluctuation $\Delta\varphi$ via arm length difference ΔL [162]:

$$\Delta\varphi \cong 2\pi\,\Delta f\,\Delta L/c. \tag{5.21}$$

The interference of the scattered light with the main beam can also couple the frequency noise into the output signal [182]. To ensure that frequency noise is sufficiently low that it does not compromise the sensitivity in the signal frequency regime, an active stabilization system is necessary to reduce the laser frequency noise.

An effective method of laser frequency stabilization was proposed by Drever and Hall *et al* [285], modelled on a technique used in microwave systems which was first proposed by Pound [286]. In optics the technique is called Pound–Drever–Hall (PDH) modulation. Light incident on a cavity is frequency modulated. The cavity creates intensity modulation whose phase depends on the relative frequency between the laser and the cavity resonance. The reflected light can be thought of as containing two beams: light simply reflected from the cavity input mirror and the light which has entered the cavity, resonated in the cavity and leaked back via the input mirror. The cavity leakage has a strong phase shift with respect to the directly reflected light from the input mirror, depending on the detuning from the cavity resonance. The interference between these two beams allows the detection of the phase difference, and hence the frequency difference, of the laser frequency compared with the cavity resonant frequency. The light from the laser is usually modulated at a RF frequency to shift the measurement to the quiet high-frequency domain. This helps overcome technical noise such as low-frequency electronics noise.

The schematic diagram in figure 58 shows a typical laser frequency stabilization scheme. A small fraction of laser light is phase modulated at a radio frequency by a Pockel cell (PC) and injected into a reference cavity. The reflected light is detected by a PD and mixed with the RF reference signal. If the laser frequency is tuned to one of the cavity resonances the reflected light has two balanced sidebands with opposite phase and a carrier. The mixer output is zero. If the laser frequency fluctuates the two sidebands will be unbalanced and the mixer will give

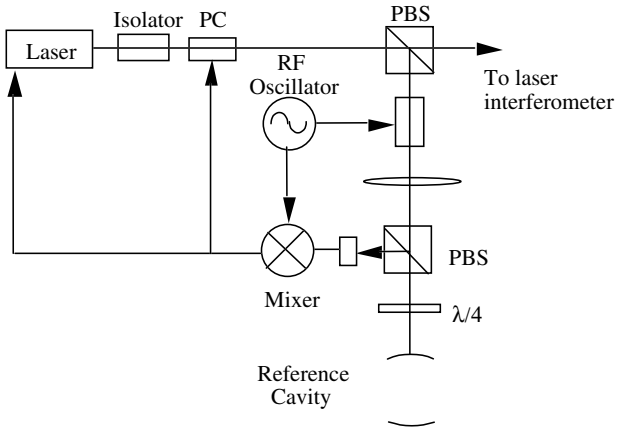

Figure 58. Frequency stabilization.

a signal proportional to the laser frequency difference with respect to the cavity resonance frequency. This signal can be fed back to a piezomirror (for low-frequency correction) and an extra-cavity Pockel cell (for high-frequency correction) to lock the laser frequency to the cavity.

The performance achievable in PDH stabilization is theoretically set by the quantum limit: the balance of shot noise and radiation pressure fluctuations which deform the reference cavity. However, in practice the laser shot noise limit is always dominant. This sets a limit to the frequency noise spectral density Ssn, and if the cavity has no losses this is given by [287]

$$S_{sn}(\mathrm{Hz}/\sqrt{\mathrm{Hz}}) = \frac{\Delta\nu}{J_0(\beta)}\sqrt{\frac{h\nu}{8\eta P_i}}. \tag{5.22}$$

Here $\Delta\nu$ is the cavity linewidth, P_i is the power incident on the cavity, ν is the laser frequency, η is the quantum efficiency of the PD, β is the modulation index, and $J_0(\beta)$ is the zeroth Bessel function.

Every gravitational wave detection group is involved in the development of laser stabilization. A frequency noise on the order of $\sim$10 mHz $\mathrm{Hz}^{-\frac{1}{2}}$ at 1 kHz has been achieved with a diode pumped Nd:YAG laser actively stabilized to a rigid reference cavity [288–291].

Another noise source in PDH locking is the mechanical and thermal noise of the reference cavity. The cavity resonant-frequency fluctuation $\Delta\nu$ is directly linked to the cavity length fluctuations ΔL. That is,

$$\frac{\Delta\nu}{\nu} = \frac{\Delta L}{L}. \tag{5.23}$$

If the reference cavity length is very long the noise contribution from a given cavity length fluctuation is much less than that of a short cavity. For this reason, the laser frequency is often stabilized to one arm cavity [163, 289] of an interferometer for further stabilization of the light frequency, and a frequency noise on the order of $\sim$10 μ Hz $\mathrm{Hz}^{-\frac{1}{2}}$ at 1 kHz has been achieved. In recent designs special-purpose *mode cleaner* cavities have been used [292] (see below) as a reference cavity. The Max Planck group has stabilized to an interferometer's power recycling cavity [173].

5.7.2. Mode cleaners. It is inevitable that the laser beam has geometric fluctuations (beam jitter) because of the vibration of the laser cavity. Vibration of the injection optics may also

introduce the beam jitter. The beam jitter noise will couple into the interferometer output signal if the two arms are not perfectly symmetric. For example, if the beamsplitter is misaligned from the optimal symmetric orientation by a small angle θ the lateral movement Δx of incident beam may produce an effective differential displacement signal Δs given by [293]

$$\Delta s = 4\theta \Delta x. \tag{5.24}$$

A simple way to clean the beam jitter noise of a low-power laser beam is to pass it through a single mode fibre [162]. In a single-mode fibre geometric fluctuations are transformed into fluctuations of the power coupling into the fibre. The problem in that because the core of a single-mode fibre has a small radius (of the order of a few wavelengths) the intensity inside the core is very high and this generates nonlinear effects including stimulated Brillouin scattering [294, 295]. This sets an upper limit on the maximum power that can be transported in a single-mode fibre. In addition, fibres themselves can be subject to vibration which can introduce additional beam jitter.

Another method to suppress beam jitter is to use a long optical cavity in transmission, called a mode cleaner. The geometric fluctuations of the laser beam are suppressed because they are not resonant within the cavity. The geometric beam fluctuations can be described in terms of higher transverse modes of the resonant cavity. In rectangular coordinates Hermite–Gaussian functions can be used to describe the eigenmodes of a cavity to a good approximation. Since the Hermite–Gaussian modes form a complete set, an incident beam with small translational movement Δx, angular fluctuation $\Delta\theta$, beam waist size mismatch $\Delta\omega_0$, and beam waist position mismatch Δb can be expanded in terms of cavity eigenmodes [292] as follows:

$$E_{\rm in} = E_{00}\left(\frac{\Delta x}{\omega_0} + j\frac{k\omega_0}{2}\Delta\theta\right)E_{10} + \frac{1}{\sqrt{2}}\left(\frac{\Delta\omega_0}{\omega_0} + j\frac{\Delta b}{k\omega^2}\right)(E_{02} + E_{20}). \tag{5.25}$$

Here E_{ij} are the amplitudes of the fundamental, first and second eigenmodes, while $E_{\rm in}$ is the amplitude of the incident beam and ω_0 is the beam waist.

For a cavity consisting of two mirrors with radii of curvature R_{c1}, R_{c2}, intensity transmission T_1, T_2, and reflectivity R_1, R_2, separated by a distance L, the fractional transmission of the incident light amplitude through this cavity is [296]

$$T_{mn} = \frac{\sqrt{T_1T_2}}{1-\sqrt{R_1R_2}}\frac{1}{\sqrt{1+(\frac{2\sqrt{R_1R_2}}{1-R_1R_2}\sin((m+n)\Psi))^2}}, \tag{5.26}$$

where $\Psi = \cos^{-1}(\sqrt{(1-L/R_{c1}(1-L/R_{c2})})$.

For the fundamental mode, $T_{00} = \frac{\sqrt{T_1T_2}}{1-\sqrt{R_1R_2}}$. The amplitude attenuation of the higher-order modes compared with the fundamental mode is given by

$$\sqrt{1+\left(\frac{2\sqrt{R_1R_2}}{1-R_1R_2}\sin((m+n)\Psi)\right)^2} \approx \frac{2F}{\pi}\sin((m+n)\Psi), \tag{5.27}$$

where $F = \frac{\sqrt{R_1R_2}}{1-R_1R_2}$ is the finesse of the cavity. Thus a high-finesse cavity mode cleaner can strongly suppress the higher-order modes.

However, the power inside a high-finesse mode cleaner cavity will also be much higher than the incident light power. Thus, thermal damage to the mirror coating becomes a key issue in defining the cavity configuration. If P is the power we want to transmit, and ω is the beam radius on the mirrors, then the power density on mirrors is given by $I = \frac{2FP}{\pi^2\omega^2}$. To avoid optical damage to the coatings of the mirrors, the spot area should be kept above $\pi\omega_{\rm min}^2 = \frac{2FP}{\pi I_{\rm max}}$, where $I_{\rm max}$ is the power density limit of the coatings.

The power transmission of an optical cavity for incident light with frequency offset f from the resonant frequency is given by the well known Lorentzian response: $T_f = \frac{T_0}{1+(2f/\Delta\nu)^2}$, where $\Delta\nu = c/2LF$ is the cavity linewidth. The cavity acts as a second-order low-pass filter. With a large length L and high finesse F the cut-off frequency becomes low. For example, for $L =$ 100 m and $F = 1000$ the cut-off frequency is 1.5 kHz. Since all the laser fluctuations (amplitude and frequency) can be understood in terms of the generation of sidebands, a mode cleaner also acts to suppress such fluctuations at offset frequencies higher than the cut-off frequency.

5.8. Optics

As we have already seen, a fundamental limitation of the sensitivity of interferometric gravitational wave detectors is shot noise, or photon-counting errors. In order to reduce shot noise, high light power must circulate in the interferometer. Because of the limitation of laser power currently available from stabilized CW lasers, power recycling appears to be an indispensable technique for large-scale instruments.

The maximum power recycling factor is determined by the total losses of the interferometer when the transmission of the recycling mirror is properly chosen. The losses of the interferometer may result from energy loss due to absorption or scattering of the mirrors, or by imperfect recombination of the two beams on the beamsplitter due to misalignments and wavefront distortions. Power losses can arise from imperfect mirror surfaces, coating inhomogeneities, diffraction losses through limited apertures, beamsplitter and mirror substrate wavefront distortion and depolarization. The minimization of these losses presents a formidable challenge.

5.8.1. Surface quality. The relevant specifications of the surface figure for optical components has been considered extensively by all of the groups building large-scale laser interferometers [196, 297–299]: see, for example, the discussion by Winkler and coworkers [196], which is based on a requirement for a power build-up in a power-recycled DL interferometer. The surface deformations can be characterized by their amplitude s and spatial wavelength λ_s. Surface deformation with λ_s smaller than the beam diameter (micro-roughness) cause the scattering loss. The relative power loss by scattering due to the micro-roughness is given by

$$\frac{\Delta P}{P} = \left(4\pi \frac{s_{\rm rms}}{\lambda_2}\right)^2, \tag{5.28}$$

in which $s_{\rm rms}$ is the rms value of the micro-roughness amplitude. The tolerable micro-roughness in a DL interferometer with power recycling gain of 100 and 34 reflections is $s_{\rm rms} < \lambda/730$.

Surface deformations with λ_s in the order of the beam diameter contribute to the beam wavefront distortion and the deterioration of the dark fringe of a perfect interference. The tolerable deformation in this scale for the same interferometer is $s_{\rm rms} < \lambda/230$. For surface deformation with λ_s larger than the beam diameter (aberration) the demands are slightly less.

Using the computer-mode-based code of Vinet and Hello [297], LIGO group derived the requirements [299] of the optical components of the 4 km Fabry–Perot Michelson interferometer. The tolerable rms amplitude of the surface micro-roughness is 0.4 nm. The surface figure error (spatial wavelength larger than beam diameter) should be less than 0.8 nm.

Techniques of superpolishing are now well established and mirrors exceeding the tight specifications required have been developed [299–301]. LIGO optics is being polished by General Optics (GO) and Commonwealth Scientific and Industrial Research Organization (CSIRO). Metrology indicated that the polished surfaces with rms deviation (after removeing focus and astigmatism) <1 nm over 20 cm were produced. Surface roughness

measurements showed a micro-roughness of ∼3 Å for CSIRO substrates and ∼0.9 Å for LIGO substrates [299].

The mirror coating is also critical for scattering level and wavefront preservation in the interferometer. VIGO group has reached ∼1 ppm scattering level on 80 mm diameter coated mirror surface. The peak-to-valley coated surface deformation is ∼14 nm on 70 mm diameter [302].

5.8.2. Absorption. Optical absorption may take place at dielectric coatings, or inside the substrate material of transmitting optical components, such as the beamsplitter and the coupling mirror of Fabry–Perot cavities. Apart from losses introduced by the absorption itself, the absorbed light power will heat the local area, and consequently deform the optical components causing wavefront distortion. This arises due to the limited thermal conductivity of the substrate. The local heating forms a temperature gradient inside the substrate and consequently introduces radius of curvature changes on surfaces. Winkler *et al* [196] has analysed the problem and shown that the change δs of the sagitta by the absorption of the reflected beam is given by

$$\delta s = \frac{\alpha}{4\pi\kappa} P_a, \tag{5.29}$$

in which P_a is the absorbed light power, α is the thermal expansion coefficient, κ is the heat conductivity of the substrate material. The crucial quantity for the magnitude of the effect is the ratio α/κ of thermal expansion to heat conductivity. The α/κ of fused silica and sapphire are 33 and 28 respectively [196].

When the beam is transmitted through a material with a temperature gradient, because of a temperature dependence of the refraction index, the refraction indices of the beam axis and the outer parts of the beam are different and thermal lensing may result. The path difference δl between beam axis and outer parts of the beam, introduced by thermal lensing, is approximately [196]

$$\delta l \approx \frac{\beta}{4\pi\kappa} P_a, \tag{5.30}$$

in which $\beta = \delta n/\delta T$ is the temperature dependence of the refraction index and P_a is the power absorption there. It is clear that one wants to keep the ratio β/κ small. The β/κ of fused silica and sapphire are 1000 and 60 [196]. As regards thermal lensing, sapphire is much better than fused silica as a substrate material.

5.8.3. Depolarization. The temperature gradient inside the substrate will also produce a stress distribution. The stresses generate strains in the substrate, which in turn produce refractive index variations (or birefringence) via the photoelastic effect. Stresses may also be introduced during the manufacturing process. The magnitude of the birefringence may be defined by the phase difference δ introduced between orthogonal polarizations. In general, the polarization of the input beam will not be parallel to one of the principal axes of the birefringent component, especially since the birefringence may vary locally.

Power loss occurs due to the depolarization of the original input beam polarization. The measured birefringence of a very homogeneous 10 cm thick Corning 7940 grade 0A fused silica plate is $\delta = 1.2^\circ \pm 0.2^\circ$ in the central area [303] which corresponds to a maximum loss of 10^{-4} per pass. The reported birefringence in sapphire is comparable, about 0.1° cm^{-1} [304]. The lowest birefringences in coatings obtainable today are between 2 to 10 μrad per reflection—but so far only for mirrors and beams with a size of a few cm and mm, respectively [197].

Hello and Vinet [305, 306] have analysed the thermal effects in massive mirrors heated by high-power laser beams. The complete numerical simulation of thermal effects in a GW interferometer [307] indicate that the first-generation detectors using silica components may require substrate absorption coefficients of $\sim$2 ppm cm^{-1} $\pm$ 15%, and coating absorption coefficient of $\sim$2 ppm $\pm$ 10%.These values are within present capabilities for mirror and coating technologies. The reported lowest absorption is a level of less than 1 ppm cm^{-1} for light of 1 μm wavelength in a fused silica sample [308] and a level of 3.1 ppm cm^{-1} in a sapphire sample [309]. The present coating absorption coefficient is $\sim$1 ppm [302]. Recycling factors of 300 [173] and 450 [174] have been achieved with power of $\sim$100 W built up inside the recycling cavity. This corresponds to $>$1 kW cm^{-2} power on the beamsplitter and mirrors. Expected limits due to thermal effects have still not been reached.

Winkler *et al* [196,197] and Strain *et al* [308] with their co-workers at MPI have evaluated the effects of thermal deformation, thermal lensing and thermally induced birefringence on a recycling interferometer. Their model assumes that Gaussian-profile laser beams heat the optical substrates through either uniform bulk absorption or uniform absorption in the coatings, and that the optics has an aperture much larger than the beam diameter. They concluded that the power limit set by thermal lensing is a problem only for advanced interferometers operating at higher power than those presently under development. They find that inherent and thermally induced birefringence will not be the dominant loss mechanism [197] assuming the lowest values for absorption and inherent birefringence reported. They propose that resonant sideband extraction is the best way of reducing the effects of thermal lensing to reach sensitivity appropriate to a 'second-generation' detector [308].

5.9. High-power lasers

The choice of the laser wavelength is an important effect on the design of a long-baseline interferometer. At short wavelengths, the beam diffracts less and thus the diameter of the interferometer mirrors and the vacuum tube can be reduced; thereby reducing the cost of the interferometer. Short wavelengths would also allow a better shot-noise-limited strain sensitivity which is $\propto\lambda^{1/2}$ [189]. Other important factors in the choice of laser wavelength are the losses (absorption and scattering) in the mirrors and beamsplitter, and the availability of suitably quiet and powerful lasers.

Contrasting with prototype interferometers which have used argon-ion lasers, all the long-baseline interferometers will use diode-laser-pumped Nd:YAG lasers ($\lambda = 1064$ nm). The use of Nd:YAG lasers is driven by their much better efficiency and generally quieter characteristics with regard to practically all types of laser noise [293]. Diode-laser-pumped miniature ring lasers can fulfil the requirements of a interferometric gravitational wave detector concerning amplitude and frequency stability [310]. But direct use of these devices in an interferometer for gravitational wave detector is not possible, because the output power of these system is limited to values below 2 W CW in a single axial mode [311].

One possible technique to increase the output power is injection locking which coherently couples a low-power master and a high-power slave oscillator resulting in a high-power output with the frequency characteristics of the master [312]. As shown in figure 59, this is accomplished by injecting the output power from the master laser into the slave laser's resonator. The PDH reflection locking is used to lock the frequency of the slave laser to the master's by adjusting the position of the slave's mirrors according to the error signal [311].

Application of the injection locking technique to Nd:YAG lasers has been extensively investigated [311,313–317]. At Laser Zentrum Hannover (LZH), a maximum single-frequency output power of 20 W has been generated by injection locking to a monolithic ring laser. The

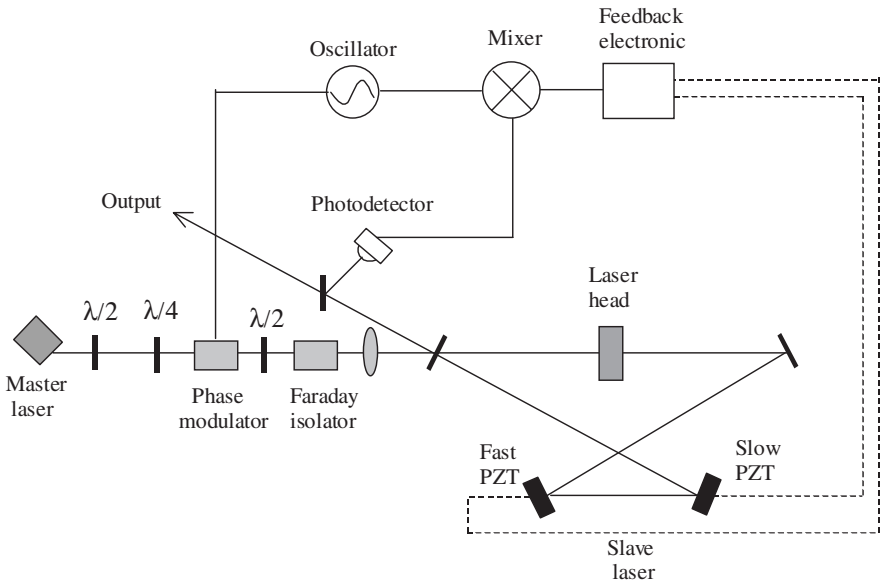

Figure 59. Schematic for injection locking of two lasers [311].

amplitude and frequency stability is investigated. The amplitude noise reaches the shot noise level beyond a few MHz. The relaxation oscillation of the miniature ring laser coupling at ∼700 kHz and the disturbance in the excitation of the slave laser caused by the diode laser power supplies at 80 kHz are two noise sources which could be further stabilized using active amplitude stabilization [318]. Using fibre-coupled diode lasers as pump sources, 62 W CW TEM_{00} mode output has been achieved [319].

At Stanford, an output of 5.5 W single-frequency, 'nearly diffraction-limited', TEM_{00} power was produced by using 50.4 W of pump power. The frequency noise of the unstabilized master laser of ∼20 Hz $Hz^{-\frac{1}{2}}$ at 1 kHz was reproduced at the output of the slave. The relative intensity noise at the output of the slave is $1.7 \times 10^{-6}/\sqrt{\text{Hz}}$ which is 10 times higher that that at the output of the master laser [314]. A 40 W CW, TEM_{00} diode-laser-pumped, Nd:YAG miniature-slab laser has been built and demonstrated with 212 W pumping power [320]. A 10 W laser-diode-pumped Nd:YAG master-oscillator power amplifier is spatially and temporally filtered by a fixed Fabry–Perot cavity, which produced a 7.6 W TEM_{00} beam with 1% higher-order transverse mode content and reduced the relative power fluctuations at 10 MHz to $2.8 \times 10^{-9}/\sqrt{\text{Hz}}$.

At VIRGO, a 10 W laser-diode-pumped Nd:YAG laser has been developed by using injection locking a high-power slave laser to a low power master laster [302]. The master laser is a 700 mW laser-diode-pumped miniature ring Nd:YAG laser operating at single-frequency. The slave laser is Nd:YAG laser transverse pumped on one side by 10 fibre-coupled diodes. TEM_{00} operation has been achieved with a slight contribution of TEM_{01} using a diaphragm inside the X-shaped ring cavity. Using a spatial filter, the TEM_{00} component can be extracted to give a 9 W output power for an effective pumped power of 60 W. The 10 W laser will be frequency pre-stabilized to a reference cavity, and be actively power stabilized.

At TAMA, with 22.3 W pump input from two fibre-coupled laser diodes, combined with 700 mW of power injected by a single-frequency master laser, the injection-locked slave laser emitted 10 W of linearly polarized TEM_{00} beam. The measured relative intensity

noise and the frequency noise are $2 \times 10^{-5}/\sqrt{\text{Hz}}$ and 50 Hz $\text{Hz}^{-\frac{1}{2}}$ respectively. When the frequency of the injection-locked laser is stabilized to an external high-finesse reference cavity, a minimum frequency noise of 40 mHz $\text{Hz}^{-\frac{1}{2}}$ was measured from the locking loop error signal at 1 kHz [313].

At Adelaide, an efficient, medium power, diode-pumped Nd:YAG slab, stable resonator, ring laser based on a new diode-pumping geometry [321] was developed. Using 18 W of absorbed laser diode power (20 W diode output power), 5.8 W TEM_{00} output beam has been produced [189].

6. Conclusion

Gravitational wave researchers have expected to detect gravitational waves 'within the next decade' for the last three decades. Detectors have been dramatically improved and a steadily increasing band of physicists has been able to devote more and more resources to the problem. In the process they have uncovered new physics and new technology. Gravitational wave detectors are the most sensitive devices ever invented.

Like the Great South Land which was rumoured for centuries before it was discovered, the spectrum of gravitational waves is a rumoured continent, first to be detected, and then to be explored. It seems not unreasonable that the exploration will begin within the next decade, but whatever happens the search will continue to motivate physicists and drive a continuing process of innovation.

Acknowledgments

The authors wish to acknowledge the Australian Research Council, which has supported gravitational wave research in Australia for many years, and our colleagues in Perth and around the world with whom we have had rich and rewarding interactions. The field is too large to be able to reference all important papers, and we apologize to those whose work we have failed to reference.

References

[1] Weisberg J M and Taylor J H 1984 Observations of post-Newtonian timing effects in the binary pulsar PSR 1913 + 16 *Phys. Rev. Lett.* **52** 1348
[2] Hulse R A and Taylor J H 1975 Discovery of a pulsar in a binary system *Astrophys. J.* **195** L51
[3] Einstein A 1916 *Preuss. Akad. Wiss. Berlin, Sitzungsberichte der Physikalisch-mathematischen Klasse* p 668
[4] Weber J 1960 Detection and generation of gravitational waves *Phys. Rev.* **117** 306
[5] Weber J 1969 Evidence for discovery of gravitational radiation *Phys. Rev. Lett.* **22** 1320
[6] Weber J 1970 Anisotropy and polarization in the gravitational-radiation experiments *Phys. Rev. Lett.* **25** 180
[7] Misner C W, Thorne K S and Wheeler J A 1973 *Gravitation* (San Francisco: Freeman)
[8] Thorne K S 1987 Gravitational radiation *300 Years of Gravitation* ed S Hawking and W Israel (Cambridge: Cambridge University Press)
[9] Saulson P R 1994 *Fundamentals of Interferometric Gravitational Wave Detectors* (Singapore: World Scientific)
[10] Weinberg S 1972 *Gravitation and Cosmology: Principles and Applications of the General Theory of Relativity* (New York: Wiley)
[11] Giazotto A 1989 Interferometer detection of gravitational waves *Phys. Rep.* **182** 365
[12] Damour T 1986 An introduction to the theory of gravitational radiation *Gravitation in Astrophysics* ed B Carter and J B Hartle (New York: Plenum)
[13] Damour T 1987 *Gravitation in Astrophysics* ed B Carter and J Hartle (New York: Plenum)
[14] Einstein A 1918 *Preuss. Akad. Wiss. Berlin, Sitzungsberichte der Physikalisch-mathematischen Klasse* p 154
[15] Suzuki T, Tsubono K, Kuroda K and Hirakawa H 1981 Calibration of gravitational radiation antenna by dynamic Newton field *Japan. J. Appl. Phys.* **20** L498

[16] Astone P *et al* 1991 Evaluation and preliminary measurement of the interaction of a dynamical gravitational near field with a cryogenic gravitational wave antenna *Z. Phys.* C **50** 21
[17] Dhurandhar S V, Blair D G and Costa M E 1996 Possibility of detection gravitational waves from millisecond pulsars by resonant bar antennas *Astron. Astrophys.* **311** 1043
[18] Thorne K S 1992 Sources of gravitational waves and prospects for their detection *Recent Advances in General Relativity* ed A Janis and J Porter (Boston: Birkhauser)
[19] Nakamura T 1995 *Proc. 7th Marcel Grossmann Meeting on General Relativity* ed R T Jantzen and G M Keiser (Singapore: World Scientific)
[20] Marck J-A 1995 *Proc. 7th Marcel Grossmann Meeting on General Relativity* ed R T Jantzen and G M Keiser (Singapore: World Scientific)
[21] Laguna P 1997 *Gravitational Waves: Sources and Detectors* ed I Ciufolini and F Fidecaro (Singapore: World Scientific) p 61
[22] Lai D and Shapiro S L 1995 Hydrodynamics of coalescing binary neutron stars: ellipsoidal treatment *Astrophys. J.* **443** 705
[23] Chandrasekhar S 1969 *Ellipsoidal Figures of Equilibrium* (New Haven, CT: Yale University Press)
[24] Houser J L, Centrella J M and Smith S C 1994 Gravitational radiation from nonaxisymmetric instability in a rotating star *Phys. Rev. Lett.* **72** 1314
[25] Hawking S W 1971 Gravitational radiation from colliding black holes *Phys. Rev. Lett.* **26** 1344
[26] Press W H and Thorne K S 1972 *Annu. Rev. Astron. Astrophys.* **10** 338
[27] Lai D and Shapiro S L 1995 Gravitational radiation from rapidly rotating nascent neutron stars *Astrophys. J.* **442** 259
[28] Phinney E S 1991 The rate of neutron star binary mergers in the universe: minimal predictions for gravity wave detectors *Astrophys. J.* **380** L17
[29] Narayan R, Piran T and Shemi A 1991 Neutron star and black hole binaries in the galaxy *Astrophys. J.* **379** L17
[30] Tutukov A V and Yungelson L R 1993 The merger rate of neutron star and black hole binaries *Mon. Not. R. Astron. Soc.* **260** 675
[31] Yamaoka H, Shigeyama T and Nomoto Z 1993 Formation of double neutron star systems and asymmetric supernova explosions *Astron. Astrophys.* **267** 433
[32] Abramovici A *et al* 1992 LIGO: The laser interferometer gravitational-wave observatory *Science* **256** 325
[33] Bradaschia C *et al* 1992 VIRGO: Very wide band interferometric gravitational wave antenna *Nucl. Phys.* B **28A** 54
[34] Johnson W W and Merkowitz S M 1993 Truncated icosahedral gravitational wave antenna *Phys. Rev. Lett.* **70** 2367
[35] Blair D G 1983 Resonant bar detectors for gravitational waves *Gravitational Radiation* ed N Deruelle and T Piran (Amsterdam: North-Holland)
[36] Rees M J 1993 *Proc. Natl Acad. Sci. USA* **90** 4840
[37] Rees M J 1997 Gravitational waves from galactic centres *Class. Quantum Grav.* **14** 1411
[38] Haehnelt M G 1994 Low-frequency gravitational waves from supermassive black holes *Mon. Not. R. Astron. Soc.* **269** 199
[39] Vecchio A 1997 Galaxy mergers and implications for massive black hole binary coalescence *Class. Quantum Grav.* **14** 1431
[40] Sigurdsson S 1997 Estimating the detectable rate of capture of stellar mass black holes by massive central black holes in normal galaxies *Class. Quantum Grav.* **14** 1425
[41] Rucinski S M 1994 M/sub V/=M/sub V/(log P, log T/sub e/) calibrations for W Ursae Majoris systems *Publ. Astron. Soc. Pac.* **106** 462
[42] Verbunt F 1997 Waiting for LISA: binaries with orbital periods less than $\sim 10^4$ s *Class. Quantum Grav.* **14** 1417
[43] Bildsten L 1998 Gravitational radiation and rotation of accreting neutron stars *Astrophys. J. Lett.* **501** L89
[44] Zwart S F P and McMillan S L W 1999 Black hole mergers in the universe *Astrophys. J. Lett. preprint* 9910061
[45] Ostriker J P and Cowie L L 1981 Galaxy formation in an intergalactic medium dominated by explosions *Astrophys. J. Lett.* **243** L127
[46] Cowie L L, Hu E M and Songaila A 1995 Detection of massive forming galaxies at redshifts $z > 1$ *Nature* **377** 603
[47] Hughes D H, Serjeant S, Dunlop J *et al* 1998 High-redshift star formation in the Hubble deep field revealed by a submillimetre-wavelength survey *Nature* **394** 241
[48] Blair D G and Ju L 1996 A cosmological background of gravitational waves produced by supernovae in the early universe *Mon. Not. R. Astron. Soc.* **283** 648

[49] Burman R R, Woodings S J and Blair D G 1998 The cosmic background of supernova-generated gravitational radiation *Publ. Astron. Soc. Australia*
[50] Ferrari V, Matarrese S and Schneider R 1999 Gravitational wave background from a cosmological population of core-collapse supernovae *Mon. Not. R. Astron. Soc.* **303** 247
[51] Ferrari V, Matarrese S and Schneider R 1999 Stochastic background of gravitational waves generated by a cosmological population of young, rapidly rotating neutron stars *Mon. Not. R. Astron. Soc.* **303** 258
[52] Flanagan E E 1993 Sensitivity of the laser interferometer gravitational wave observatory to a stochastic background, and its dependence on the detector orientations *Phys. Rev.* D **48** 2389
[53] Allen B 1996 *Proc. Les Houches Astronomical Sources of Gravitational Waves* ed J-A Marck and J-P Lasoto (Cambridge: Cambridge University Press)
[54] Blair D G 1999 Stochastic background detection with LLO and ALLEGRO *LIGO Report* U990003-00-0
[55] Sazhin M V 1988 *Experimental Gravitational Physics* ed P F Michelson (Singapore: World Scientific) p 179
[56] Taylor J H and Weisberg J M 1989 Further experimental tests of relativistic gravity using the binary pulsar PSR 1913+16 *Astrophys. J.* **345** 434
[57] Weber J 1967 Gravitational radiation *Phys. Rev. Lett.* **18** 498
[58] Forward R L 1971 Multidirectional, multipolarization antenna for scalar and tensor gravitational radiation *Gen. Rel. Grav.* **2** 149
[59] Wagoner R V and Paik H J 1977 *Gravitasione Sperimentale* (Rome: Academia Nazionale dei Lincei)
[60] Richard J-P 1982 A multimode antenna for the detection of short pulses of gravitational radiation *Proc. 2nd Marcel Grossmann Meeting* ed R Ruffini (Amsterdam: North-Holland)
[61] Richard J-P 1984 Wide-band bar detectors of gravitational radiation *Phys. Rev. Lett.* **52** 165
[62] Solomonson N, Johnson W W and Hamilton W O 1992 Comparative performance of two-, three- and four-mode gravitational radiation detectors *Phys. Rev.* D **46** 2299
[63] Tobar M E 1995 Characterizing multi-mode resonant-mass gravitational wave detectors *J. Phys. D: Appl. Phys.* **28** 1729
[64] Gertsenshtein M E and Pustovoit V I 1962 On the detection of low frequency gravitational waves *Sov. Phys.–JETP* **16** 433
[65] Weber J 1960s Weber proposed interferometer detector idea but never published it; see Thorne K S 1978
[66] Weiss R 1972 *MIT Res. Lab. Electron. Q. Report* vol 105, p 54
[67] Iess L and Armstrong J W 1997 *Gravitational Waves: Sources and Detectors* ed I Ciufolini and F Fidecaro (Singapore: World Scientific) p 323
[68] Bertotti B and Giampieri G 1998 Solar coronal plasma in Doppler measurements *Sol. Phys.* **178** 85
[69] Folkner W M, Hechler F, Vincent M A and Bender P L 1997 LISA orbit and stability *Class. Quantum Grav.* **14** 1405
[70] Astone P *et al* 1997 The gravitational wave detector Nautilus operation at $T = 0.1$ K *Astropart. Phys.* **7** 231
[71] Geng Z K, Hamilton W O, Johnson W W, Mauceli E, Merkowitz S, Morse A and Solomonson N 1995 Operation of the Allegro detector at LSU *Proc. 1st Eduardo Amaldi Conf. on Gravitational Wave Experiments* ed E Coccia, G Pizzella and G Ronga (Singapore: World Scientific)
[72] Locke C R, Tobar M E, Ivanov E N and Blair D G 1998 Parametric interaction of the electric and acoustic fields in a sapphire monocrystal transducer with a microwave readout *J. Appl. Phys.* **84** 6523
[73] Coccia E *et al* 1997 Experimental study of spherical resonators at very low temperatures *Proc. Omnidirectional Gravitational Radiation Observatory* ed W G Velloso Jr, O D Aguiar and N S Magalhaes (Singapore: World Scientific)
[74] Frossati G *et al* 1997 Very low temperature measurements of quality factors of copper alloys for resonant gravitational wave antennae *Proc. Omnidirectional Gravitational Radiation Observatory* ed W G Velloso Jr, O D Aguiar and N S Magalhaes (Singapore: World Scientific)
[75] Velloso W F Jr *et al* 1997 On the use of the finite elements method to design the structures of mechanical isolation to resonant mass antennas *Proc. Omnidirectional Gravitational Radiation Observatory* ed W G Velloso Jr, O D Aguiar and N S Magalhaes (Singapore: World Scientific)
[76] Astone P, Bonifazi P, Pallottino G V and Pizzella G 1994 Wiener filters for gravitational-wave antennas: characteristics and application *Nuovo Cimento* C **17** 713
[77] Liu J F, Blair D G and Ju L 1998 Near shore ocean wave measurement using a very low frequency folded pendulum *Meas. Sci. Technol.* **9** 1772
[78] Astone P, Buttigilione C, Frasca S, Palottin G V and Pizzella G 1997 The fast matched filter for gravitational-wave analysis *Nuovo Cimento* C **20** 9
[79] Heng I S 1999 Long term performance of the cryogenic resonant-mass gravitational wave antenna, NIOBE *PhD Thesis* University of Western Australia
[80] Mohanty S D, Heng I S, Blair D G, Dhurandhar S V, Tobar M and Ivanov E 1998 A data analysis approach for

detecting gravitational waves from PSR 0437-4715 *Mon. Not. R. Astron. Soc.* **301** 469
[81] Heng I S, Blair D G, Ivanov E N and Tobar M E 1996 Report on two years of the UWA gravitational radiation antenna *Phys. Lett.* A **218** 190
[82] Johnston S 1996 *Pulsars: Problems and Progress (ASP Conf. Ser. 105)* ed S Johnston, M A Walker and M Bailes p 501
[83] Suzuki T 1993 Low resonant frequency resonant detectors *Int. Workshop of New Technology for Gravitational Astronomy (Perth, 1993)*
[84] Astone P 1998 On the detection of monochromatic and stochastic gravitational waves with resonant gravitational wave detectors *Proc. 2nd Eduardo Amaldi Conf. on Gravitational Waves* ed E Coccia, G Pizzella and G Veneziano (Singapore: World Scientific)
[85] Schutz B F 1995 Sources of gravitational radiation for detectors of the 21st century *Proc. 1st Eduardo Amaldi Conf. on Gravitational Wave Experiments* ed E Coccia, G Pizzella and G Ronga (Singapore: World Scientific)
[86] Astone P *et al* 1997 Contributions from the AIE to the GWDAW2 workshop, Orsay *Albert Einstein Institut Preprint* AEI-057
[87] Giazotto A 1996 *Int. Conf. on Gravitational Waves: Source and Detectors (Pisa, Italy)*
[88] Opfer J E, Boughn S P, Fairbank W M, McAshan M S, Paik H J and Taber R C 1974 *Proc. Conf. Low Temperature Physics-LT13* vol 4, ed K D Timmerhaus, W J O Sullivan and E F Hammel (New York: Plenum) p 59
[89] Hamilton W O, Pipes P B and Nayar P S 1974 *Proc. Conf. Low Temperature Physics-LT13* vol 4, ed K D Timmerhaus, W J O Sullivan and E F Hammel (New York: Plenum) p 555
[90] Callen H B and Green R F 1952 On a theorem of irreversitable thermodynamics *Phys. Rev.* **86** 702
[91] Gibbons G W and Hawking S W 1971 Theory of the detection of short bursts of gravitational radiation *Phys. Rev.* D **4** 2191
[92] Papoulis A 1977 *Signal Analysis* (New York: McGraw-Hill)
[93] Pallotino G V and Pizzella G 1991 *The Detection of Gravitational Waves* ed D G Blair (Cambridge: Cambridge University Press)
[94] Braginsky V B 1970 *Physical experiments with test bodies NASA Tech. Trans. F672NTIS* (Springfield: NASA)
[95] Giffard R P 1976 Ultimate sensitivity limit of a resonant gravitational wave antenna using a linear motion detector *Phys. Rev.* D **14** 2478
[96] Heffner H 1962 *Proc. IRE* **50** 1604
[97] Braginsky V B, Vorontsov Y I and Kalili F Y 1978 *JETP Lett.* **27** 276
[98] Caves C M, Thorne K S, Drever R W P, Sandberg V D and Zimmerman M 1980 On the measurement of a weak classical force coupled to a quantum-mechanical oscillator I. Issues of principle *Rev. Mod. Phys.* **52** 341
[99] Unruh W G 1978 Analysis of quantum-nondemolition measurement *Phys. Rev.* D **18** 1764
[100] Tobar M E, Ivanov E N, Oi D K L, Cuthbertson D B and Blair D G 1997 Sapphire test-masses for measuring the standard quantum limit and achieving quantum non-demolition *J. Appl. Phys.* B **64** 153
[101] Paik H J and Wagoner R V 1976 Calculation of the absorption cross section for a cylindrical gravitational-wave antenna *Phys. Rev.* D **13** 2694
[102] Blair D G 1980 *Gravitational Radiation, Collapsed Objects and Exact Solutions* vol 314, ed D Edward (Berlin: Springer) p 299
[103] Veitch P J 1991 *The Detection of Gravitational Waves* ed D G Blair (Cambridge: Cambridge University Press)
[104] Cuthbertson B D, Tobar M E, Ivanov E N and Blair D G 1996 Parametric back action effects in a high-Q cryogenic sapphire transducer *Rev. Sci. Instrum.* **67** 2435
[105] Douglass X H and Braginsky V B 1979 *General Relativity, An Einstein Centenary Survey* ed S W Hawking and W Israel (Cambridge: Cambridge University Press)
[106] Johnson W W and Bocko M 1981 Approaching the quantum 'limit' for force detection *Phys. Rev. Lett.* **47** 1184
[107] Bocko M and Johnson W W 1982 Surpassing the amplifier limit for force detection *Phys. Rev. Lett.* **48** 1371
[108] Bocko M and Johnson W W 1984 Phase-sensitive parametric motion transducer *Phys. Rev.* A **30** 2135
[109] Pang Y and Richard J P 1997 Development of an optical transducer *Proc. 1st Int. Workshop for an Omnidirectional Gravitational Radiation Observatory* ed W F Velloso Jr, O D Aguiar and N S Magalhaes (Singapore: World Scientific)
[110] Conti L, Prodi G A, Vitale S, Marin F, De Rosa M, Cerdonio, Taffarello L and Zendri J P 1999 An optical transduction chain for the AURIGA detector *Proc. 3rd Eduardo Amaldi Conf. on Gravitational Waves* ed S Meshkov (New York: AIP) at press
[111] Braginsky V B 1983 *Gravitational Radiation* ed N Deruelle and T Piran (Amsterdam: North-Holland)
[112] Braginsky V B, Mitrofanov V P and Panov V I 1985 *System with Small Dissipation* (Chicago, IL: University of Chicago Press)

[113] Paik H J 1976 Superconducting tunable-diaphragm transducer for sensitive acceleration measurements *J. Appl. Phys.* **47** 1168
[114] Astone P *et al* 1993 Long-term operation of the Rome explorer cryogenic gravitational wave detector *Phys. Rev.* D **47** 362
[115] Linthorne N P, Veitch P J, Blair D G, Turner P J, Tobar M E and Mann A G 1990 Niobium gravitational radiation antenna with superconducting parametric transducer *Physica* B **165** 9–10
[116] Allen Z *et al* 1999 Development of a multi-mode transducer using a double SQUID preamplifier for the ALLEGRO detector *Proc. 3rd Eduardo Amaldi Conf. on Gravitational Waves* ed S Meshkov (New York: AIP) at press
[117] Giazotto A 1987 *Proc. 7th Conf. on General Relativity and Gravitational Physics* ed U Bruzzo, R Cianci and E Massa (Singapore: World Scientific)
[118] Ju L, Blair D G, Peng H and van Kann F 1992 High dynamic range measurements of an all metal isolator using a sapphire transducer *Meas. Sci. Technol.* **3** 463
[119] Tsubono K 1992 Private communication
[120] Richard J-P 1976 Sensor and suspensions for a low-temperature gravitational wave antenna *Rev. Sci. Instrum.* **47** 423
[121] Aldcroft T L, Michelson P and Taber R C 1992 *Proc. 6th Marcel Grossmann Meeting* ed H Sato and T Nakamura (Singapore: World Scientific)
[122] Blair D G, Tuner P J, Berinson D, Ju L, van Kann F J, Linthorne N P, Mann A G, Peng H and Tobar M E 1992 *Proc. 6th Marcel Grossmann Meeting* ed H Sato and T Nakamura (Singapore: World Scientific)
[123] Blair D G 1982 *Proc. 2nd Marcel Grossmann Meeting* ed R Ruffine (Amsterdam: North-Holland)
[124] Michelson P F and Taber R C 1984 Can a resonant-mass gravitational-wave detector have wideband sensitivity? *Phys. Rev.* D **29** 2149
[125] Veitch P J 1986 *PhD Thesis* University of Western Australia
[126] Coccia E 1984 Nodal point supported gravitational wave antennas *Rev. Sci. Instrum.* **55** 1980
[127] Allen Z A *et al* 2000 First search of gravitational wave bursts with a network of detectors *Phys. Rev. Lett.* submitted
[128] Vitale S, Cerdonio M, Coccia E and Ortolan A 1997 Gravitational-wave stochastic background detection with resonant-mass detectors *Phys. Rev.* D **55** 1741
[129] Astone P *et al* 1997 *Proc. 1st Int. Workshop for an Omnidirectional Gravitational Radiation Observatory* ed W F Velloso Jr, O D Aguiar and N S Magalhaes (Singapore: World Scientific)
[130] Modestino G *et al* 1999 Detection of cosmic rays by NAUTILUS *Proc. 3rd Eduardo Amaldi Conf. on Gravitational Waves* ed S Meshkov (New York: AIP) at press
[131] Hamilton W O 1987 *Int. Symp. on Experimental Gravitational Physics* ed P F Michelson (Singapore: World Scientific)
[132] Frasca S 1980 Analogical device for a rough localization of gravitational-wave sources *Nuovo Cimento* C **3** 237
[133] Nitti G 1980 Choice of optimal orientation of one or two cylindrical gravitational antennas *Nuovo Cimento* C **3** 420
[134] Blair D G, Frasca S and Pizzella G 1988 Antenna pattern for four gravitational wave antennas *Nuovo Cimento* **11** 185
[135] Schutz B F and Tinto M 1987 Antenna patterns of interferometric detectors of gravitational waves I. Linearly polarized waves *Mon. Not. R. Astron. Soc.* **224** 131
[136] Astone P, Pallottino G V and Pizzella G 1998 On the efficiency of the coincidence search in gravitational wave experiments *Gen. Rel. Grav.* **30** 105
[137] Heng I S, Bonifazi P, Blair D G, Tobar M E and Ivanov E N 1999 Background noise reduction in gravitational wave detectors through use of an amplitude ratio filter *Gen. Rel. Grav.* to be published
[138] Coccia E, Fafone V and Frossati G 1995 On the design of ultralow temperature spherical gravitational wave detectors *Proc. 1st Eduardo Amaldi Conf. on Gravitational Wave Experiments* ed E Coccia, G Pizzella and G Ronga (Singapore: World Scientific)
[139] Coccia E, Lobo J A and Ortega J A 1995 Proposed gravitational wave observatory based on solid elastic spheres *Phys. Rev.* D **52** 3735
[140] Coccia E and Fafone V 1996 Coalescing binaries and spherical gravitational wave detectors *Phys. Lett.* A **213** 16
[141] Coccia E, Fafone V, Frossati G, ter Haar E and Meisel M W 1996 Eigenfrequencies and quality factors of vibration of aluminium alloy spherical resonators *Phys. Lett.* A **219** 263
[142] Bianchi N, Coccia E, Colacino C N, Fafone V and Fucito F 1996 Testing theories of gravity with a spherical gravitational wave detector *Class. Quantum Grav.* **13** 2865

[143] Vitale S, Cerdonio M, Coccia E and Ortolan A 1997 Gravitational-wave stochastic background detection with resonant-mass detectors *Phys. Rev.* D **55** 1741
[144] Merkowitz S M and Johnson W W 1995 Spherical gravitational wave antennas and the truncated icosahedral arrangement *Phys. Rev.* D **51** 2546
[145] Zhou C Z and Michelson P F 1994 Spherical resonant-mass gravitational wave detectors *Phys. Rev.* D **51** 2517
[146] Stevenson T R 1995 Signal to noise analysis for a spherical gravitational wave antenna instrumented with multiple transducers *Proc. 1st Eduardo Amaldi Conf. on Gravitational Wave Experiments* ed E Coccia, G Pizzella and G Ronga (Singapore: World Scientific)
[147] Stevenson T R 1997 Limits on the sensitivity of spherical gravitational wave detectors and on the accuracy of reconstructed signals *Phys. Rev.* D **56** 564
[148] Harry G M, Stevenson T R and Paik H J 1996 Detecability of gravitational wave events by spherical resonant-mass antennas *Phys. Rev.* D 54 2409
[149] Lobo J A 1995 What can we learn about gravitational wave physics with an elastic spherical antenna? *Phys. Rev.* D **52** 591
[150] Blair D G, Peng H and Ivanov E N 1992 Sapphire dielectric resonator transducers *J. Phys. D: Appl. Phys.* **25** 1110
[151] Tobar M E, Ivanov E N, Blair D G and Cuthbertson B D 1997 *Proc. 1st Int. Workshop for an Omnidirectional Gravitational Radiation Observatory* ed W F Velloso Jr, O D Aguiar and N S Magalhaes (Singapore: World Scientific)
[152] Cuthbertson B D, Tobar M E, Ivanov E N and Blair D G 1998 Sensitivity and optimization of a high-Q sapphire dielectric motion sensing transducer *IEEE Trans. UFFC* **45** 1303
[153] Tobar M E, Ivanov E N and Blair D G 1999 Parametric transducers for the advanced cryogenic resonant-mass gravitational wave detectors *Gen. Rel. Grav.* to be published
[154] Frasca S and Papa M 1995 Local array of high frequency antennas *Proc. 1st Eduardo Amaldi Conf. on Gravitational Wave Experiments* ed E Coccia, G Pizzella and G Ronga (Singapore: World Scientific)
[155] Harry G M, Jin I, Paik H J, Stevenson T R and Wellstood F C 2000 Two stage superconducting quantum interference device amplifier in a high-Q gravitational wave transducer *Appl. Phys. Lett.* **76** 1446
[156] Tobar M, Ivanov E and Blair D G 1999 NIOBE: improved noise temperature performance and background noise suppression *Proc. 3rd Eduardo Amaldi Conf. on Gravitational Waves* ed S Meshkov (New York: AIP) at press
[157] Tobar M E, Ivanov E N and Blair D G 1996 Future prospects for the University of Western Australia's cryogenic resonant-mass gravitational wave detector *Czech. J. Phys.* **46** 2909
[158] Gertsenshtein M E and Pustovoit V I 1962 On the detection of low frequency gravitational waves *Sov. Phys.–JETP* **16** 433
[159] Moss G E, Miller L R and Forward R L 1971 Photon-noise-limited laser transducer for gravitational antenna *Appl. Opt.* **10** 2495
[160] Forward R L and Mosse G E 1972 Wideband interferometric gravitational radiation antenna *Bull. Am. Phys. Soc.* **17** 1183
[161] Forward R L 1978 Wide-band laser interferometer gravitational-radiation experiment *Phys. Rev.* D **17** 379
[162] Shoemaker D, Schilling R, Schnupp L, Maischberger K and Rüdiger A 1988 Noise behaviour of the Garching 30-meter prototype gravitational-wave detector *Phys. Rev.* D **38** 423
[163] Robertson D I, Morrison E, Hough J, Killbourn S, Meers B J, Newton G P, Robertson N A, Strain K A and Ward H 1995 The Glasgow 10 m prototype laser interferometric gravitational wave detector *Rev. Sci. Instrum.* **66** 4447
[164] Abramovici A *et al* 1996 Improved sensitivity in a gravitational wave interferometer and implications for LIGO *Phys. Lett.* A **218** 157
[165] Drever R W P 1983 *Gravitational Radiation* ed N Deruelle and T Piran (Amsterdam: North-Holland)
[166] B J Meers 1988 Recycling in laser-interferometric gravitational-wave detectors *Phys. Rev.* D **38** 2317
[167] Vinet J-Y, Meers B J, Man C N and Brillet A 1988 Optimization of long-baseline optical interferometers for gravitational-wave detection *Phys. Rev.* D **38** 433
[168] Mizuno J, Strain K A, Nelson P G, Chen J M, Schilling R, Rüdiger A, Winkler W and Danzmann K 1993 Resonant sideband extraction: a new configuration for interferometric gravitational wave detectors *Phys. Lett.* A **175** 273
[169] Heinzel G, Mizuno J, Schilling R, Winkler W, Rüdiger A and Danzmann K 1996 An experimental demonstration of resonant sideband extraction for laser-interferometric gravitational wave detectors *Phys. Lett.* A **217** 305
[170] Man C N, Shoemaker D, Manh Pham Tu and Davey D 1990 External modulation technique for sensitive interferometric detection of displacement *Phys. Lett.* A **148** 8
[171] Fritschel P, Shoemaker D and Weiss R 1992 Demonstration of light recycling in a Michelson interferometer

with Fabry–Perot cavities *Appl. Opt.* **31** 1412
[172] Regehr M W, Raab F J and Whitcomb S E 1995 Demonstration of a power-recycled Michelson interferometer with Fabry–Perot arms by frontal modulation *Opt. Lett.* **20** 1507
[173] Schnier D, Mizuno J, Heinzel G, Lück H, Rüdiger A, Schilling R, Schremple M, Winkler W and Danzmann K 1997 Power recycling in the Garching 30 m prototype interferometer for gravitational-wave detection *Phys. Lett.* A **225** 210
[174] Fritschel P, Gonzalez G, Lantz B and Zuker M 1998 High power phase measurements limited by quantum noise and application to detection of gravitational waves *Phys. Rev. Lett.* **80** 318
[175] Gray M B, Stevenson A J, Bachor H-A and McClelland D E 1998 Broadband and tuned signal recycling with a simple Michelson interferometer *Appl. Opt.* **37** 5886
[176] Strain K A and Meers B J 1991 Experimental demonstration of dual recycling for interferometric gravitational-wave detectors *Phys. Rev. Lett.* **66** 1391
[177] Heinzel G, Stain K A, Mizuno J, Skeldon K D, Willke B, Winkler W, Schilling R, Rüdiger A and Danzmann K 1998 Experimental demonstration of a suspended dual recycling interferometer for gravitational wave detection *Phys. Rev. Lett.* **81** 5493
[178] Bradaschia C *et al* 1990 The VIRGO project: a wide band antenna for gravitational wave detection *Nucl. Instrum. Methods* A **289** 518
[179] Danzmann K *et al* 1995 GEO 600: A 600 m laser interferometric gravitational wave antenna *Proc. 1st Eduardo Amaldi Conf. on Gravitational Wave Experiments* ed E Coccia, G Pizzella and G Tonga (Singapore: World Scientific)
[180] Tsubono K 1995 300-m laser interferometer gravitational wave detector (TAMA 300) *Proc. 1st Eduardo Amaldi Conf. on Gravitational Wave Experiments* ed E Coccia, G Pizzela and G Tonga (Singapore: World Scientific)
[181] Drever R W P, Ford G M, Hough J, Kerr I, Munley A J, Pugh J R, Robertson N A and Ward H 1983 *Proc. 9th Int. Conf. on General Relativity and Gravitation* ed E Shmutzer (Cambridge: Cambridge University Press)
[182] Shilling R, Schnupp L, Winkler W, Billing H, Maischerger K and Rüdiger A 1981 A method to bolt out scattered light effects and its application to a gravitational wave detector *J. Phys. E: Sci. Instrum.* **14** 65
[183] Winkler W 1991 A Michelson interferometer using delay line *The Detection of Gravitational Waves* ed D G Blair (Cambridge: Cambridge University Press)
[184] Sun K X, Fejer M M, Gustafson E and Byer R L 1996 Sagnac interferometer for gravitational-wave detection *Phys. Rev. Lett.* **76** 3053
[185] Sun K X, Gustafson E K, Fejer M M and Byer R L 1997 Polarization-based balanced heterodyne detection method in a Sagnac interferometer for precision phase measurement *Opt. Lett.* **22** 1359
[186] Shaddock D A, Gray M B and McClelland D E 1998 Experimental demonstration of resonant sideband extraction with a Sagnac interferometer *Appl. Opt.* **37** 7995
[187] Mizuno J, Rüdiger A, Schilling R, Winkler W and Danzmann K 1997 Frequency response of Michelson- and Sagnac-based interferometers *Opt. Commun.* **138** 383
[188] Drever R W P 1995 Concepts for extending the ultimate sensitivity of interferometric gravitational wave detectors using non-transmissive optics with diffractive or holographic coupling *Proc. 7th Marcel Grossman Meeting on General Relativity* ed M Keiser and R T Jantzen (Singapore: World Scientific)
[189] Veitch P J, Munch J, Hamilton M W, Ottaway D, Greentree A and Tikhomirov A 1995 High power laser and novel optics for laser interferometric gravitational wave detectors *Aust. J. Phys.* **48** 999
[190] Sun K X and Byer R L 1998 All-reflective Michelson, Sagnac, and Fabry–Perot interferometers based on grating beam splitters *Opt. Lett.* **23** 567
[191] Caves C M 1980 Quantum-mechanical radiation-pressure fluctuations in an interferometer *Phys. Rev. Lett.* **45** 75
[192] Caves C M 1981 Quantum-mechanical noise in an interferometer *Phys. Rev.* D **23** 1693
[193] Meers B J 1988 Recycling in laser interferometric gravitational-wave detectors *Phys. Rev.* D **38** 2317
[194] McClelland D E 1995 An overview of recycling in laser interferometric gravitational wave detectors *Aust. J. Phys.* **48** 953
[195] GEO 600 1994 Proposal for a 600 m laser-interferometric gravitational wave antenna *Max-Plank-Institut Für Quantenoptik Report* MPQ 190
[196] Winkler W, Danzmann K, Rüdiger A and Schilling R 1991 Optical problems in interferometric gravitational wave antennas *Proc. 6th Marcel Grossmann Meeting* ed H Sato and T Nakamura (Singapore: World Scientific)
[197] Winkler W, Rüdiger A, Schilling R, Strain K A and Danzmann K 1994 Birefringence-induced losses in interferometers *Opt. Commun.* **112** 245
[198] Plissi M V *et al* 1998 Aspect of the suspension system for GEO 600 *Rev. Sci. Instrum.* **69** 3055
[199] Stephens M, Saulson P and Kovalik J 1991 A double pendulum vibration isolation system for a laser

interferometric gravitational wave antenna *Rev. Sci. Instrum.* **62** 924
[200] Tsubono K, Arays A, Kawabe K, Moriwaki S and Mio N 1993 Triple-pendulum vibration isolation system for a laser interferometer *Rev. Sci. Instrum.* **64** 2237
[201] Veitch P J, Robertson N A, Cantley C A and Hough J 1992 Active control of a balanced two-stage pendulum vibration isolation system and its application to laser interferometric gravity wave detectors *Rev. Sci. Instrum.* **64** 1330
[202] Del Fabbro R, Di Virgilio A, Giazotto A, Kautzky H, Montelatici V and Passuello D 1988 Performance of a gas spring harmonic oscillator *Rev. Sci. Instrum.* **59** 293
[203] Del Fabbro R, Di Virgilio A, Giazotto A, Kautzky H, Montelatici V and Passuello D 1988 First results from the Pisa seismic noise super-attenuator for low frequency gravitational wave detection *Phys. Lett.* A **132** 237
[204] Braccini S *et al* 1996 Seismic vibration mechanical filters for the gravitational waves detector VIRGO *Rev. Sci. Instrum.* **67** 2899
[205] Robertson N A, Drever R W P, Kerr I and Hough J 1982 Passive and active seismic isolation for gravitational radiation detectors and other instruments *J. Phys. E: Sci. Instrum.* **15** 1101
[206] Saulson P 1984 Vibration isolation for broadband gravitational wave antennas *Rev. Sci. Instrum.* **55** 1315
[207] Campani E, Giazotto A and Passuello D 1986 Performance of an analogue phase follower *Rev. Sci. Instrum.* **57** 79
[208] Giazotto A, Passuello D and Stefani A 1986 One-mile equivalent length interferometric pendulum for seismic noise reduction *Rev. Sci. Instrum.* **57** 1145
[209] Nelson P G 1991 An active vibration isolation system for inertial reference and precision measurement *Rev. Sci. Instrum.* **62** 2069
[210] Stebbins R, Newell D, Richman S, Bender P, Faller J and Mason J 1994 Low-frequency active vibration isolation system *Proc. SPIE* **2264** 27
[211] McLoughlin F A 1990 Integrated structural damping and control system design for high-order flexible systems *PhD Thesis* Stanford University
[212] Beccaria M *et al* 1997 Extending the VIRGO gravitational wave detection band down to a few Hz: metal blade springs and magnetic antisprings *Nucl. Instrum. Methods* A **394** 397–408
[213] Pinoli M, Blair D G and Ju L 1993 Test on a low-frequency inverted pendulum system *Meas. Sci. Technol.* **4** 995
[214] Saulson P R, Stebbins R T, Dumont F D and Mock S E 1994 The inverted pendulum as a probe of anelasticity *Rev. Sci. Instrum.* **65** 182
[215] Losurdo G *et al* 1999 An inverted pendulum preisolator stage for the VIRGO suspension system *Rev. Sci. Instrum.* **70** 2507
[216] Winterflood J, Zhou Z B and Blair D G 1999 Reducing low-frequency residual motion in vibration isolation to the nanometre level *Proc. 3rd Eduardo Amaldi Conf. on Gravitational Waves* ed S Meshkov (New York: AIP) at press
[217] van Kann F 1993 Private communications
[218] Blair D G, Liu J, Moghaddam E F and Ju L 1994 Performance of an ultra low-frequency folded pendulum *Phys. Lett.* A **193** 223
[219] Liu L, Winterflood J and Blair D G 1995 Transfer function of an ultralow frequency vibration isolation system *Rev. Sci. Instrum.* **66** 3216
[220] Liu J, Ju L and Blair D G 1997 Vibration isolation performance of an ultra-low frequency folded pendulum *Phys. Lett.* A **228** 243
[221] Barton M A and Kuroda K 1994 Ultra-low frequency oscillator using a pendulum with crossed suspension wires *Rev. Sci. Instrum.* **65** 3775
[222] Kanda N, Barton M A and Kuroda K 1994 Transfer function of a crossed wire pendulum isolation system *Rev. Sci. Instrum.* **65** 3780
[223] Winterflood J and Blair D G 1996 A long-period conical pendulum for vibration isolation *Phys. Lett.* A **222** 141
[224] Winterflood J and Blair D G 1998 Ultra-low frequency pre-isolation in three dimensions *Proc. 2nd Eduardo Amaldi Conf. on Gravitational Waves* ed E Coccia, G Pizzella and G Veneziano (Singapore: World Scientific)
[225] Braccini S *et al* 1993 An improvement in the VIRGO super attenuator for interferometric detection of gravitational wave: the sue of a magnetic antispring *Rev. Sci. Instrum.* **64** 310
[226] LaCoste L J B 1934 *Phys.* **5** 178
[227] Bertolini A, Cella G, DeSalvo R and Sannibale V 1999 Seismic noise filters, vertical resonance frequency reduction with geometrical anti-springs: a feasibility study *Nucl. Instrum. Methods* A **435** 475
[228] Saulson P 1990 Thermal noise in mechanical experiments *Phys. Rev.* D **42** 2437
[229] Kimball A L and Lovell D E 1927 *Phys. Rev.* **30** 948

[230] Ju L, Blair D G and Notcutt M 1993 Ultrahigh *Q* pendulum suspensions for gravitational wave detectors *Rev. Sci. Instrum.* **64** 1899
[231] Quinn T J, Speake C C and Brown L M 1992 Materials problems in the construction of long-period pendulums *Phil. Mag.* A **65** 261
[232] Kovalik J and Saulson P R 1993 Mechanical loss in fibres for low noise pendulums *Rev. Sci. Instrum.* **64** 2942
[233] Gillespie A and Raab F 1993 Thermal noise in the test mass suspensions of a laser interferometer gravitational-wave detector prototype *Phys. Lett.* A **178** 357
[234] Gillespie A and Raab F 1994 Suspensions losses in the pendula of laser interferometer gravitational-wave detectors *Phys. Lett.* A **190** 213
[235] Zuker M 1992 The LIGO 40 m prototype laser interferometer gravitational wave detector *Proc. 6th Marcel Grossmann Meeting* ed H Sato and T Nakamura (Singapore: World Scientific)
[236] Logan J E, Hough J and Robertson N A 1993 Aspect of the thermal motion of a mass suspended as a pendulum by wires *Phys. Lett.* A **183** 145
[237] Bernardi A, Majorana E, Puppo P, Rapagnani P, Ricci F and Testi E 1999 Suspension last stages for the mirrors of the VIRGO interferometric gravitational wave antenna *Rev. Sci. Instrum.* **70** 3463
[238] Hough J 1989 Prospect for gravitational wave detection with laser interferometer detectors *Proc. 5th Marcel Grossmann Meeting* ed Blair D G and Buckingham M J (Singapore: World Scientific)
[239] Rowan S *et al* 1999 Mechanical loss factors of material and suspension systems for advanced gravitational wave detectors *Proc. 3rd Eduardo Amaldi Conf. on Gravitational Waves* ed S Meshkov (New York: AIP) at press
[240] Braginsky V B, Mitrofanov V P and Vyatchanin S P 1994 Isolation of test masses in the advanced laser interfeormetric gravitational wave antennae *Rev. Sci. Instrum.* **65** 3771
[241] Braginsky V B, Mitrofanov V P and Tokmakov K V 1994 On the thermal noise from the violin modes of the test mass suspension in the gravitational wave antennae *Phys. Lett.* A **186** 18
[242] Logan J E, Hough J and Robertson N A 1992 An investigation of limitations to quality factor measurements of suspended masses due to resonances in the suspension wires *Phys. Lett.* A **170** 352
[243] González G I and Saulson P R 1994 Brownian motion of a mass suspended by an anelastic wire *J. Acoust. Soc. Am.* **96** 207
[244] Martin W 1987 Experiments and techniques for the detection of gravitational and pulsed electromagnetic radiation from astrophysical sources *PhD Thesis* University of Glasgow
[245] Ju L, Blair D G, Taniwaki M and Andrew R 1999 The quality factor of niobium flexure pendulums *Phys. Lett.* A **254** 239
[246] Bondu F and Vinet J-Y 1995 Mirror thermal noise in interferometric gravitational-wave detectors *Phys. Lett.* A **198** 74
[247] Gillespie A and Raab F 1995 Thermally excited vibration isolations of the mirrors of laser interferometer gravitational-wave detectors *Phys. Rev.* D **52** 577
[248] Logan J E, Robertson N A, Hough J and Veitch P J 1992 An investigation of some mechanical properties of materials for test masses in laser gravitational wave detectors *Proc. 6th Marcel Grossmann Meeting* ed H Sato and T Nakamura (Singapore: World Scientific)
[249] Traeger S, Willke B and Danzmann K 1997 Monolithically suspended fused silica substrates with very high mechanical *Q Phys. Lett.* A **225** 39
[250] Taniwaki M, Ju L, Blair D G and Tobar M E 1998 Design and verification of low acoustic loss suspension system for measuring the *Q*-factor of a gravitational wave detector test mass *Phys. Lett.* A **246** 273
[251] Startin W J, Beilby M A and Saulson P R 1998 Mechanical quality factors of fused silica resonators *Rev. Sci. Instrum.* **69** 3681
[252] Braginsky V B, Mitorfanov V P and Okhrimenko O A 1992 Oscillators for free mass gravitational antennas *JETP Lett.* **55** 432
[253] Locke C 1999 University of Western Australia Private communication
[254] Ju L, Notcutt M, Blair D G, Bondu R and Zhao C N 1996 Sapphire beamsplitters and test masses for advanced laser interferometer gravitational wave detectors *Phys. Lett.* A **218** 197
[255] Rowan S, Twyford S M, Hough J, Gwo D-H and Route R 1998 Mechanical losses associated with the technique of hydroxide-catalysis bonding of fused silica *Phys. Lett.* A **246** 471
[256] Ju L, Taniwaki M, Blair D G, Benabid F and Notcutt M 1998 Using sapphire test masses and niobium flexure suspension in laser interferometer gravitational wave detectors *Proc. 2nd Eduardo Amaldi Conf. on Gravitational Waves* ed E Coccia, G Pizzella and G Veneziano (Singapore: World Scientific)
[257] Gwo D H 1998 Stanford University Private communication
[258] Bradaschia C, Del Fabbro R, Di Virgilio A, Giazotto A, Hautzky H, montelatici V and Passuello D 1989 First results on the electronic cooling of the Pisa seismic noise super-attenuator for gravitational wave detection

Phys. Lett. A **137** 329
[259] Blair D G, Ju L and Peng H 1993 Vibration isolation for gravitational wave detection *Class. Quantum Grav.* **10** 2407
[260] Winterflood J, Blair D G, Schilling R and Notcutt M 1995 Position control system for suspended masses in laser interferometer gravitational wave detectors *Rev. Sci. Instrum.* **66** 174
[261] Ke W, Blair D G, Notcutt M and Ju L 1995 Normal mode suppression in all metal cantilever vibration isolators *Phys. Lett.* A **197** 275
[262] Veitch P J, Robterson N A, Cantley C A and Hough J 1993 Active control of a balanced two-stage pendulum vibration isolation system and its application to laser interferometric gravity wave detectors *Rev. Sci. Instrum.* **64** 1330
[263] Veitch P J, Hough J, Morrison E and Robertson D I 1996 Can piezoelectric accelerometers be used to actively damp the mechanical suspensions in laser interferometric gravitational wave detectors? *Rev. Sci. Instrum.* **67** 633
[264] Braccini S *et al* 1995 Low noise wideband accelerometer using an inductive displacement sensor *Rev. Sci. Instrum.* **66** 2672
[265] Luiten A N, Beccaria M and Zhang Z 1997 Ground tilt spectrum measured with a new high sensitivity rotational accelerometer *Rev. Sci. Instrum.* **68** 1889
[266] Linsay P S and Shoemaker D H 1982 Low-noise RF capacitance bridge transducer *Rev. Sci. Instrum.* **53** 1014
[267] Drever R W P 1982 Interferometric detectors for gravitational radiation *Gravitational Radiation, Proc. Les Houches Summer Institute* ed T Piran and N Deruelle
[268] Man C N, Shoemaker D, Manh Pham Tu and Dewey D 1990 External modulation technique for sensitive interferometric detection of displacements *Phys. Lett.* A **148** 8
[269] Gray M B, Stevenson A J, Harb C C, Bachor H-A and McClelland D E 1996 External phase-modulation interferometry *Appl. Opt.* **35** 1623
[270] Schnupp L 1988 Contribution to the European collaboration meeting on interferometric detection of gravitational waves (Sorrento) Unpublished
[271] Takahashi R, Mizuno J, Miyoki S and Kawashima N 1994 Control of a 10 m delay line laser interferometer using the pre-modulation method *Phys. Lett.* A **187** 157
[272] Regehr M W, Raab F J and Whitcomb S E 1995 Demonstration of a power-recycled Michelson interferometer with Fabry–Perot arms by frontal modulation *Opt. Lett.* **20** 1507
[273] Flaminio R and Heitmann H 1996 Longitudinal control of an interferometer for the detection of gravitational waves *Phys. Lett.* A **214** 112
[274] Ando M, Kawabe K and Tsubono K 1997 Signal separation technique for a power-recycled interferometric gravitational wave detector *Phys. Lett.* A **237** 13
[275] Billing H, Maischberger K, Rüdiger A, Schilling R, Schnupp L and Winkler W 1979 An argon laser interferometer for the detection of gravitational radiation *J. Phys. E: Sci. Instrum.* **12** 1043
[276] Shoemaker D, Fritschel P, Giaime J, Christensen N and Weiss R 1991 Prototype Michelson interferometer with Fabry–Perot cavities *Appl. Opt.* **30** 3133
[277] Stevenson A J, Gray M B, Bachor H A and McClelland D E 1993 Quantum noise limited interferometer phase measurements *Appl. Opt.* **32** 3481
[278] Stevenson A J, Gray M B, Harb C C, Bachor H A and McClelland D E 1995 Interferometer with internal and external phase modulation *Aust. J. Phys.* **48** 971
[279] Lyons T T 1997 An optically recombined laser interferometer for gravitational wave detection *PhD Thesis* California Institute of Technology
[280] Barone F, Di Fiore L, Milano L and Russo G 1994 A digital approach to automatic control of a long-baseline interferometric antenna for gravitational wave detection *Meas. Sci. Technol.* **5** 1187
[281] Barone F, Di Fiore L, Milano L, Russo G and Solimeno S 1992 Automatic alignment of a Michelson interferometer *IEEE Trans. Nucl. Sci.* **39** 232
[282] Barone F, Calloni E, Di Fiore L, Grado A, Milano L and Russo G 1996 Digitally controlled interferometer prototype for gravitational wave detection *Rev. Sci. Instrum.* **67** 4353
[283] Heflin E G and Kawashima N 1995 *The Institute of Space and Astronautical Science, Japan ISAS Research Note* ISAS RN 567
[284] Heflin E G and Kawashima N 1995 *The Institute of Space and Astronautical Science, Japan ISAS Research Note* ISAS RN 563
[285] Drever R W P, Hall T L, Kowalski F V, Hough J, Ford G M, Munley A G and Ward H 1983 Laser phase and frequency stabilization using an optical resonator *J. Appl. Phys.* B **31** 97
[286] Pound R V 1946 *Rev. Sci. Instrum.* **17** 490
[287] Day T, Gustafson E K and Byer R L 1992 Sub-hertz relative frequency stabilization of two-diode laser-pumped

Nd:YAG lasers locked to a Fabry–Perot interferometer *IEEE Trans. Quantum Electron.* **28** 1106
[288] Shoemaker D, Brillet A, Man C N and Cregut O 1989 Frequency-stabilized laser-diode-pumped Nd:YAG laser *Opt. Lett.* **14** 609
[289] Kawamura S, Abramovici A and Zuker M E 1997 Improved multistage wideband laser frequency stabilization *Rev. Sci. Instrum.* **68** 223
[290] Bondu F, Fritschel P, Man C N and Brillet A 1996 Ultrahigh-spectral-purity laser for the VIRGO project *Opt. Lett.* **21** 582
[291] Nakagawa K, Katsuda T and Ohtsu M 1995 Short-term frequency stabilization of diode-laser pumped Nd:YAG lasers using double pendulum suspended cavities *J. Appl. Phys.* B **66** 489
[292] Araya A, Mio N, Tsubono K, Suehiro K, Telada S, Ohashi M and Fujimoto M 1997 Optical mode cleaner with suspended mirrors *Appl. Opt.* **36** 1446
[293] Skeldon K D, Strain K A, Grant A I and Hough J 1996 Test of an 18-m-long suspended mode cleaner cavity *Rev. Sci. Instrum.* **67** 2443
[294] Cotter D 1983 Stimulated Brillouin scattering in monomode optical fibre *J. Opt. Commun.* **4** 10
[295] Shiraki K, Ohashi M and Tateda M 1995 Suppression of stimulated Brillouin scattering in a fibre by changing the core radius *Electron. Lett.* **31** 668
[296] Rudiger A, Shilling R, Schnupp L, Winkler V, Billing H and Maischberger K 1998 A mode selector to suppress fluctuations in laser beam geometry *Opt. Acta* **28** 641
[297] Vinet J Y, Hello P H, Man C N and Brillet A 1992 A high accuracy method for the simulation of non-ideal optical cavity *J. Physique* I **2** 1287
[298] McClelland D E, Savage C M, Trigdell A J and Mavaddat R 1993 Tolerance of dual recycling laser interferometric gravitational wave detectors to mirror tilt and curvature errors *Phys. Rev.* D **48** 5474
[299] Fritschel P 1997 The LIGO project: progress and plans *Proc. 2nd Eduardo Amaldi Conf. on Gravitational Waves* ed E Coccia, G Pizzella and G Veneziano (Singapore: World Scientific)
[300] Walsh C, Davis G, Farrant D, Leistner A, Lesha F, Oreb B, Pavlovic E, Seckold J and Stuart W 1998 Fabrication and measurement of optics for gravitational wave detectors *13th National Congress of the Australian Institute of Physics (Fremantle, Western Australia, Sept. 1998)*
[301] Blair D G *et al* 1997 Development of low-loss sapphire mirrors *Appl. Opt.* **36** 337
[302] Mackowski J M, Pinard L, Dognin L, Ganau P, Lagrange B, Michel C and Morgue M 1998 VIRGO mirrors: wavefront control *Report* Univ. Lyon I, 5
[303] Logan J E, Robertson N A and Hough J 1994 Measurements of birefringence in a suspended sample of fused silica *Opt. Commun.* **107** 342
[304] Benabid F, Notcutt M, Ju L and Blair D G 1998 Birefringence measurements of sapphire test masses for laser interferometer gravitational wave detector *Phys. Lett.* A **237** 337
[305] Hello P and Vinet J Y 1990 Analytical models of thermal aberrations in massive mirrors heated by high power laser beams *J. Physique* **51** 1267
[306] Hello P and Vinet J Y 1990 Analytical models of transient thermoelastic deformations of mirrors heated by high power cw laser beams *J. Physique* **51** 2243
[307] Hello P and Vinet J Y 1993 Simulation of thermal effects in interferometric gravitational-wave detectors *Phys. Lett.* A **178** 351
[308] Strain K A, Danzmann K, Mizuno J, Nelson P G, Rüdiger A, Schilling R and Winkler W 1994 Thermal lensing in recycling interferometric gravitational wave detectors *Phys. Lett.* A **194** 124
[309] Blair D, Cleva F and Man C N 1997 Optical absorption measurements in monocrystalline sapphire at 1 μm *Opt. Mater.* **8** 233
[310] Kane T J and Byer R L 1985 Monolithic, unidirectional single-mode Nd:YAG ring laser *Opt. Lett.* **10** 65
[311] Freitag I, Golla D, Knoke S, Schöne W, Zellmer H, Tünnermann A and Welling H 1995 Amplitude and frequency stability of a diode pumped Nd:YAG laser operating at a single-frequency continuous-wave output power of 20 W *Opt. Lett.* **20** 462
[312] Siegman A E 1986 *Lasers* (Mill Valley, CA: University Science Books)
[313] Yang S T, Imai Y, Oka M, Eguchi N and Kubota S 1996 Frequency-stabilized, 10-W continuous-wave, laser-diode, end-pumped, injection-locked, Nd:YAG laser *Opt. Lett.* **21** 1676
[314] Farinas A D, Gustafson E K and Byer R L 1994 Design and characterization of a 5.5-W, CW, injection-locked fibre-coupled, laser-diode-pumped Nd:YAG miniature-slab laser *Opt. Lett.* **19** 114
[315] Harb C C, Ralph T C, Huntington E H, Freitag I, McClelland D E and Bachor H A 1996 Intensity noise properties of injection locked lasers *Phys. Rev.* A **54** 4370
[316] Harb C C, Ralph T C, Huntington E H, Bachor H A and McClelland D E 1997 Intensity noise dependence of Nd:YAG lasers on their diode-laser pump sources *J. Opt. Soc. Am.* B **14** 2936
[317] Huntington E H, Harb C C, Ralph T C, McClelland D E and Bachor H A 1998 Feedback control of the intensity

noise of injection locked lasers *Opt. Commun.* **145** 359
[318] Harb C C, Gray M B, Bachor H-A, Schilling R, Rottengatter P, Freitag I and Welling H 1994 Suppression of the intensity noise in a diode-pumped neodymium:YAG nonplanar ring laser *IEEE J. Quantum Electron.* **25** 767
[319] Golla D, Bode M, Knoke S, Schone W and Tunnermann A 1996 62-W CW TEM/sub 00/ Nd:YAG laser side-pumped by fibre-coupled diode lasers *Opt. Lett.* **21** 210
[320] Shine R J Jr, Alfrey A J and Byer R L 1995 40-W CW, TEM00-mode, diode-laser-pumped, Nd:YAG miniature-slab laser *Opt. Lett.* **20** 459
[321] Richards J and McInnes A 1995 Versatile, efficient, diode-pumped miniature slab laser *Opt. Lett.* **20** 371
[322] Hough J 1997 LISA—new development in design *Proc. 2nd Edoardo Amaldi Conf. on Gravitational Waves* ed E Coccia, G Pizzella and G Veneziano (Singapore: World Scientific)
[323] LISA web page: http://lisa.jpl/nasa/gov
[324] Drever R W P 1991 Fabry–Perot cavity gravity-wave detectors *The Detection of Gravitational Waves* ed D G Blair (Cambridge: Cambridge University Press)
[325] Meers B J 1989 The frequency response of interferometric gravitational wave detectors *Phys. Lett.* A **142** 465
[326] Ju L and Blair D G 1994 Low resonant frequency cantilever spring vibration isolator for gravitational wave detectors *Rev. Sci. Instrum.* **65** 3482